Structural and catalytic characterization of *B. viridis* and *P. aeruginosa* homospermidine synthases reveals the essential role of cation-π interaction

Dissertation

zur Erlangung des Doktorgrades
der Mathematisch-Naturwissenschaftlichen Fakultät
der Christian-Albrechts-Universität zu Kiel

vorgelegt von
Felix Helfrich

Kiel, 2020

Erster Gutachter:	Prof. Dr. Axel J. Scheidig
Zweiter Gutachter:	Prof. Dr. Dietrich Ober
Tag der Verteidigung:	10.12.2020
Zum Druck genehmigt:	10.12.2020

Erklärung

Hiermit erkläre ich, dass ich bis zum heutigen Tage weder an der Christian-Albrechts-Universität zu Kiel noch an einer anderen Hochschule ein Promotionsverfahren endgültig nicht bestanden habe oder mich in einem entsprechenden Verfahren befinde. Außerdem wurde mir kein akademischer Grad entzogen. Ich erkläre, dass die Abhandlung nach Inhalt und Form die eigene Arbeit ist, dass ich die Inanspruchnahme fremder Hilfen aufgeführt habe und dass ich die wörtlich oder inhaltlich aus anderen Quellen entnommenen Stellen als solche gekennzeichnet habe. Ich erkläre, dass diese Arbeit weder ganz noch zum Teil schon einer anderen Stelle im Rahmen eines Prüfungsverfahrens vorgelegen hat. Zum Zeitpunkt der Begutachtung unterliegen Teile dieser Arbeit dem Peer-Review-Prozess des Journals *Biochemistry* zur Erwägung einer zukünftigen Publikation. Ich erkläre, dass die Arbeit unter Einhaltung der Regeln guter wissenschaftlicher Praxis der Deutschen Forschungsgemeinschaft entstanden ist.

Kiel, 01.10.2020

Felix Helfrich

Danksagung

Ich möchte mich an dieser Stelle für die fachliche und private Unterstützung während meiner Promotionszeit bedanken:

Bei Prof. Axel Scheidig bedanke ich mich herzlich für die Aufnahme in die Arbeitsgruppe und für die Beratung und Unterstützung bei der Bearbeitung meiner verschiedenen Forschungsprojekte.

Prof. Frank Sönnichsen und Dr. Hugo van Ingen (Solution NMR Group, Universität Utrecht, Utrecht, Niederlande) danke ich für das herausragende Engagement innerhalb des „Luciferase-Projektes“, für die Durchführung der NMR-Messungen und für die Einführung in die Daten-Auswertung. Im Kontext des „Luciferase-Projektes“ danke ich auch Dr. Christoph Plieth für seine Ratschläge zur praktischen Umsetzbarkeit von Experimenten und für die Zurverfügungstellung verschiedener Substrate.

Großer Dank gilt auch meinen Kollegen Sebastian, Brigitte, Kubi, Chrissy und vielen mehr für konstruktive Diskussionen und die angenehme Arbeitsatmosphäre. Zusätzlicher Dank gilt dabei Sebastian für die Ratschläge zur Weiterführung seines ehemaligen „HSS-Projektes“ und Brigitte für die Unterstützung im Labor und beim Versand von Proben.

Am meisten und auf besonderer Ebene bedanke ich mich bei meinen Eltern für die kontinuierliche Unterstützung auf meinem Lebensweg und bei meiner Ehefrau, die mir unsere gemeinsame Tochter geschenkt hat.

Zusammenfassung

Polyamine beeinflussen medizinisch relevante Prozesse in dem opportunistischen Erreger *P. aeruginosa*, darunter Virulenz, Biofilm-Formation und Empfindlichkeit gegenüber Antibiotika. Obwohl die Homospermidin-Synthase (HSS) von *P. aeruginosa* ein Teil des Polyamin-Metabolismus in zahlreichen Stämmen einschließlich PA7 und PA14 ist, wurde bisher weder ihre Rolle noch ihre Struktur untersucht. Der Reaktionsmechanismus der NAD^+-abhängigen bakteriellen HSS wurde bereits anhand von Kristallstrukturen der *B. viridis* HSS (*Bv*HSS) charakterisiert. Diese Arbeit präsentiert die Kristallstruktur der HSS von *P. aeruginosa* (*Pa*HSS) im Komplex mit ihrem Substrat Putrescin. Eine hohe strukturelle Ähnlichkeit zwischen *Pa*HSS und *Bv*HSS mit Konservierung katalytisch relevanter Aminosäure-Reste wird demonstriert, was die *Bv*HSS als geeignetes Modell für den Reaktionsmechanismus der *Pa*HSS qualifiziert. Dementsprechend werden Kristallstrukturen von Varianten der *Bv*HSS mit einzeln ausgetauschten Resten präsentiert und zusätzlich HPLC-basierte Aktivitäts-Assays der *Pa*HSS, *Bv*HSS und *Bv*HSS-Varianten dargelegt. Saure Reste im Eingangsbereich der Bindetasche („Ionische Rutsche“) und in der Nähe des aktiven Zentrums („Innere Amino-Stelle“) ermöglichen eine effiziente Homospermidin-Produktion durch Anziehung bzw. Koordinierung von Putrescin. Der Tryptophan-Rest im aktiven Zentrum stabilisiert kationische Moleküle durch Kation-π-Interaktion, was sich aus der Interaktions-Geometrie zwischen Putrescin und dem Indol-Ring ableiten lässt. Austausch des Tryptophan-Restes gegen verschiedene andere Aminosäuren zeigte eine Abhängigkeit der Katalyse von einem aromatischen Interaktionspartner mit hoch negativem elektrostatischen Potential. Die Elektronendichte-Verteilung in einem aktiven Zentrum legt die Bildung eines NAD^+-Adduktes nahe. Diese Erkenntnisse erweitern das Wissen über die Struktur und den Reaktionsmechanismus der bakteriellen HSS und liefern Ansatzpunkte für ein rationales Inhibitor-Design.

Abstract

Polyamines influence medically relevant processes in the opportunistic pathogen *P. aeruginosa* including virulence, biofilm formation and susceptibility to antibiotics. Although the pseudomonal homospermidine synthase (HSS) is part of the polyamine metabolism in various strains including PA7 and PA14, neither its role nor structure were examined so far. The reaction mechanism of the NAD^+-dependent bacterial HSS was previously characterized based on crystal structures of the *B. viridis* HSS (*Bv*HSS). This thesis presents the crystal structure of the *P. aeruginosa* HSS (*Pa*HSS) in complex with its substrate putrescine. A high structural similarity between *Pa*HSS and *Bv*HSS with conservation of catalytically relevant residues is demonstrated, qualifying *Bv*HSS as model for the reaction mechanism of *Pa*HSS. Following this strategy, crystal structures of single residue variants of *Bv*HSS are presented together with HPLC-based activity assays of *Pa*HSS, *Bv*HSS and *Bv*HSS variants. For efficient homospermidine production, acidic residues at the entrance of the binding pocket (“ionic slide”) and near the active site (“inner amino site”) attract and coordinate putrescine, respectively. The tryptophan residue at the active site stabilizes cationic reaction components via cation-π interaction, as inferred from the interaction geometry between putrescine and the indole ring plane. Exchange of the tryptophan residue for other amino acids revealed a distinct catalytic requirement for an aromatic interaction partner with highly negative electrostatic potential. The electron density distribution in one active site suggests formation of an NAD^+ adduct. These findings deepen the structural and mechanistic knowledge about the bacterial HSS and provide approaches for rational inhibitor design.

Table of Contents

List of Figures

List of Tables

Abbreviations

ADC	arginine decarboxylase
AEX	anion exchange chromatography
AGM	agmatine
AIH	agmatine iminohydrolase/deiminase
APH	acetylpolyamine amidohydrolase
APT	aminopropyltransferase
Ara4N	4-amino-4-deoxy-L-arabinose
ATP	adenosine triphosphate
AUH	agmatine ureohydrolase
BES	N,N-bis(2-hydroxyethyl)-2-aminoethanesulfonic acid
*Bv*HSS	*B. viridis* homospermidine synthase
CAD	cadaverine
CANSDC	carboxynorspermidine decarboxylase
CF	cystic fibrosis
CHES	2-(cyclohexylamino)ethanesulfonic acid
DAP	diaminopropane
dcSAM	decarboxylated S-adenosylmethionine
DOHH	deoxyhypusine hydroxylase
DTT	dithiothreitol
GST	glutathione S-transferase
HEPES	4-(2-hydroxyethyl)-1-piperazineethanesulfonic acid
HEPES	2-[4-(2-hydroxyethyl)piperazin-1-yl]ethanesulfonic acid
HPLC	high-performance liquid chromatography
HRV3C	human rhinovirus 3C
HSP	*sym*-homospermidine
HSS	homospermidine synthase
IMAC	immobilized metal ion chromatography
IPTG	isopropyl-β-D-1-thiogalactopyranoside
LDC	lysine decarboxylase
LIOAS	laser-induced optoacoustic spectroscopy
LMW	low-molecular-weight
LPS	lipopolysaccharide
MALS	multi-angle light scattering
MES	2-(N-morpholino)ethanesulfonic acid
MIC	minimal inhibitory concentration
MOPS	3-morpholinopropane-1-sulfonic acid
MR	molecular replacement
M_W	molecular weight
NAD^+	nicotinamide adenine dinucleotide
NCPAH	N-carbamoylputrescine amidohydrolase
NSPD	*sym*-norspermidine
ODC	ornithine decarboxylase
*Pa*HSS	*P. aeruginosa* homospermidine synthase
PAs	polyamines
PBS	phosphate-buffered saline

PEG	polyethylene glycol
PIPES	1,4-piperazinediethanesulfonic acid
PMSF	phenylmethylsulfonyl fluoride
PTC	putrescine transcarbamylase
PUT	putrescine
RMSD	root-mean-square distances
r_W	van der Waals radii
SDS-PAGE	sodium dodecyl sulfate polyacrylamide gel electrophoresis
SEC	size-exclusion chromatography
SPD	spermidine
SPDDH	spermidine dehydrogenase
SPM	spermine
T2SS, T3SS	type II/III secretion system
TAPS	N-tris(hydroxymethyl)methyl-3-aminopropanesulfonic acid
TCS	two-component regulatory systems
TES	2-[[1,3-dihydroxy-2-(hydroxymethyl)propan-2-yl]amino]ethanesulfonic acid
TM	melting temperature
TRIS	tris(hydroxymethyl)aminomethane
TSA	thermal shift assay
wt	wildtype

1 Introduction

1.1 Polyamines

Polyamines (PAs) were found in almost all living organisms within the three domains of life (Michael 2016). PAs are small molecules with amino groups, which are positively charged at physiological pH (Bencini et al. 1999) and separated by aliphatic carbon chains. These properties allow both hydrophobic and ionic interactions between PAs and cellular compounds in addition to covalent bonding. In fact, measurement of the cellular PA concentration and of the binding constants for DNA, RNA and phospholipids suggested, that PAs predominantly bind to RNA (including ATP) and to a lesser extent to DNA (Watanabe et al. 1991; Miyamoto et al. 1993). Binding to protein seemed to be neglectable in general.

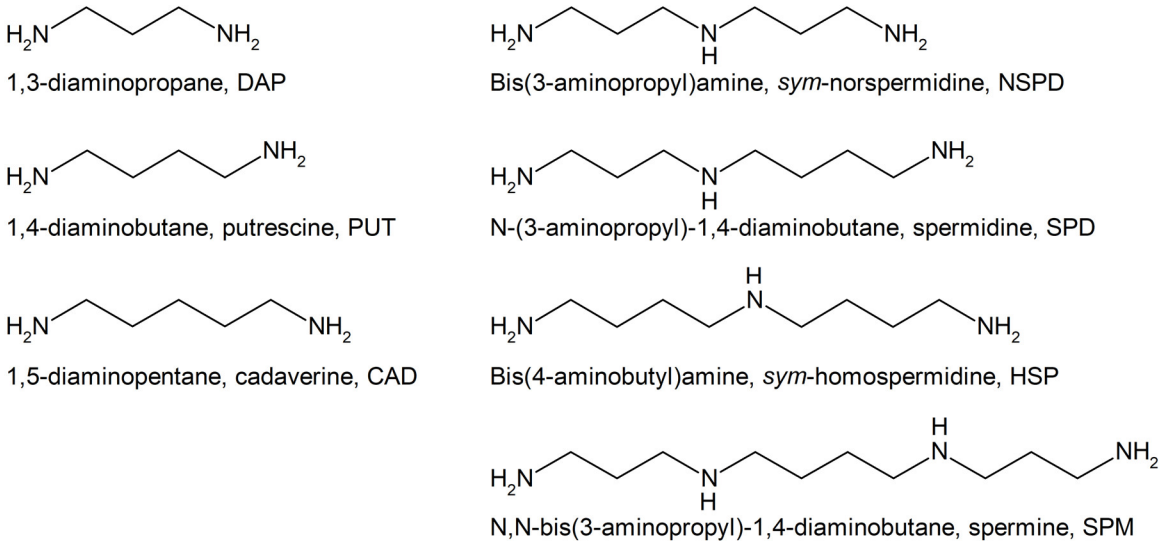

Figure 1: Two-dimensional structures of selected biogenic polyamines.

The most dominant PAs (Figure 1) in plants and mammalian cells are putrescine (1,4-diaminobutane, PUT), spermidine (N-(3-Aminopropyl)-1,4-diaminobutane, SPD) and spermine (N,N′-bis(3-aminopropyl)-1,4-diaminobutane, SPM). In addition to PUT and SPD, prokaryotes species-specifically contain various other PAs including cadaverine (1,5-diaminopentane, CAD), *sym*-norspermidine (bis(3-aminopropyl)amine, NSPD) and *sym*-homospermidine (bis(4-aminobutyl)amine, HSP) (Hamana and Matsuzaki 1992; Hamana et al. 2007).

1.2 Polyamine biosynthesis

1.2.1 Synthesis of diamines

For synthesis of 1,3-diaminopropane (DAP), aspartate semialdehyde is converted into L-2,4-diaminobutanoate by 2-ketoglutarate 4-aminotransferase, followed by production of DAP by L-2,4-diaminobutanoate decarboxylase (Ikai and Yamamoto 1994; Ikai and Yamamoto 1997). It can also be released by catabolic cleavage of SPD into 4-aminobutanal and DAP by SPD dehydrogenase (Dasu et al. 2006).

PUT is synthesized via five different pathways depending on the organism. Ornithine can be decarboxylated by ornithine decarboxylase (ODC) to directly form PUT. Three other pathways start with the production of agmatine (AGM) by decarboxylation of arginine via arginine decarboxylase (ADC). AGM is then directly converted into PUT by agmatine ureohydrolase (AUH) or intermediately deaminated to N-carbamoylputrescine by agmatine iminohydrolase/deiminase (AIH). PUT synthesis from N-carbamoylputrescine is subsequently accomplished either by hydrolysis using N-carbamoylputrescine amidohydrolase (NCPAH) or by conversion to PUT and carbamoylphosphate by putrescine transcarbamylase (PTC) involving inorganic phosphate. Another pathway generates PUT via citrulline as intermediate. All pathways containing ODC and ADC can be found in bacteria depending on the species (Wargnies et al. 1979; Michael 2016). Eukaryotes predominantly and mammals most likely exclusively exhibit the ODC pathway (Kanerva et al. 2008; Pegg 2009). Plants may alternatively utilize the citrulline and NCPAH pathways (Chen et al. 2018), the latter being evolutionary obtained from a cyanobacterial endosymbiont (Borrell et al. 1995; Illingworth et al. 2003; Janowitz et al. 2003; Piotrowski et al. 2003; Michael 2016).
CAD is synthesized from lysine by lysine decarboxylase (LDC) (Gale and Epps 1944).

1.2.2 Synthesis of norspermidine, spermidine and spermine

PUT can be aminopropylated by SPD synthase to yield SPD, which is in turn aminopropylated to SPM by SPM synthase (Pegg 2009; Shao et al. 2012). The aminopropyl group is provided by decarboxylated S-adenosylmethionine (dcSAM), which was generated from SAM by S-adenosylmethionine decarboxylase. For SPD synthesis, some bacteria alternatively use aspartate β-semialdehyde to convert PUT into carboxyspermidine by carboxyspermidine dehydrogenase and subsequent decarboxylation to SPD by carboxyspermidine decarboxylase (Tait 1976; Hanfrey et al. 2011). Similarly, the triamine NSPD is formed by carboxynorspermidine dehydrogenase (CANSDH) and carboxynorspermidine decarboxylase (CANSDC) using DAP instead of PUT as aminopropyl-acceptor (Nakao et al. 1991; Yamamoto et al. 1994; Lee et al. 2009). Another rare synthetic pathway for SPD was found in *T. thermophilus*, which aminopropylates AGM using dcSAM via an SPD synthase homologue. An agmatine ureohydrolase homologue subsequently produces SPD (Ohnuma et al. 2005).
In addition, species-dependent catabolic pathways allow to break down longer PAs into shorter ones to e.g. convert SPM into SPD or SPD into PUT. This is either directly achieved by amine oxidases or by N1-acetylation via SPM/SPD-N1-acetyltransferase, which is followed by action of acetylpolyamine oxidase (Sánchez-Jiménez et al. 2019; Wang et al. 2019).

1.2.3 Synthesis of homospermidine

HSP is synthesized by evolutionary unrelated homospermidine synthases (HSS) in bacteria (Tait 1979; Krossa et al. 2016) and in pyrrolizidine alkaloid-synthesizing plants (Srivenugopal and Adiga 1980; Ober and Hartmann 1999b). HSP is also formed as side-product of eukaryotic DHS (Ober and Hartmann 1999a), which actual function is the essential transfer of an aminobutyl moiety onto the eIF5a (chapter 1.4, p. 5) (Park et al. 1981).
While the bacterial HSS favors the conversion of two PUT molecules into one HSP molecule, it also

tolerates SPD in combination with PUT or SPD as sole substrate to form HSP (Ober et al. 1996; Shaw et al. 2010). In contrast, the plant HSS and the DHS can only produce HSP by transfer of the aminobutyl moiety from SPD (or HSP) to PUT (Ober et al. 2003). Neither PUT nor SPD as sole substrates can be converted into HSP by these enzymes.

1.3 Bacterial homospermidine synthase

The phylogenetic distribution of the bacterial HSS and the implicated evolution was previously examined (Shaw et al. 2010): The enzyme is mostly found in α-proteobacteria and in some β- and γ-proteobacteria, including pathogenic strains like *L. pneumophila* and *P. aeruginosa*. Proposed to be a result of horizontal gene transfer, it is also present in single-celled eukaryotes, archaea, bacteriophages and viruses. Based on similarities regarding the sequence and the catalyzed reaction, the bacterial HSS was suggested to be evolved from CA(N)SDH (chapter 1.2.2, p. 2)). However, this relationship could not be structurally verified without the structure of CA(N)SDH. Structure-based comparison of the bacterial HSS with other known structures revealed common domain assembly and cofactor usage of lysine 6-dehydrogenase, saccharopine dehydrogenase and aspartate dehydrogenase.

While the bacterial HSS most efficiently converts two PUT molecules into one HSP molecule, it was shown to catalyze various side reactions (Ober et al. 1996) as depicted in Figure 2.

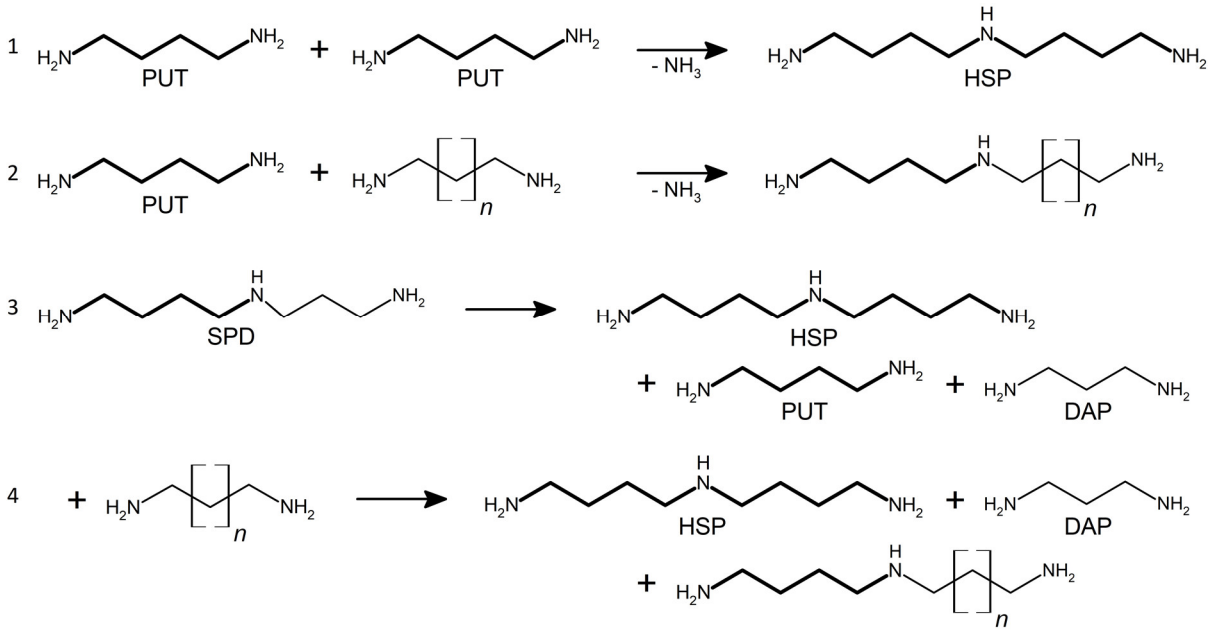

Figure 2: Reactions catalyzed by bacterial HSS.

Simplified depiction of the reactions catalyzed by the bacterial HSS (Ober et al. 1996). Bonds of PUT-derived aminobutyl moieties are depicted thicker for visual convenience. 1: Two PUT molecules are converted into HSP; 2: PUT and a second diamine (n = 1 to 5) are converted into a corresponding triamine; 3: SPD as sole substrate is converted into HSP, PUT and DAP; 4: SPD and a diamine (n = 3 to 4) are converted into HSP, a corresponding aminobutyl-containing triamine and DAP.

HSP can also be produced from a mixture of SPD and PUT, releasing DAP as by-product, or from SPD alone, releasing PUT and DAP as by-products. In other side reactions, the aminobutyl moiety of

PUT is connected to primary diamines with three (DAP) to seven (1,7-diaminoheptane) carbons, forming the corresponding triamines. Similarly, the aminobutyl moiety of SPD can be transferred onto CAD or 1,6-diaminohexane to form the corresponding triamine and DAP as by-product. Other diamines than PUT are not accepted as sole substrate.

The bacterial HSS requires the presence of NAD^+ for catalysis, which cannot be substituted by NADH, $NADP^+$ or NADPH (Tait 1979). It is active from neutral to basic pH with an optimum at pH ~8.8, while the activity is further increased by 50 mM potassium ions (Yamamoto et al. 1993; Ober et al. 1996). DAP acts as strong competitive inhibitor (Tait 1979; Yamamoto et al. 1993), although it is converted into SPD together with PUT.

The first bacterial HSS structure to be solved was derived from *L. pneumophila*, albeit with moderate resolution (2.5 Å, PDB ID 2PH5) and questionable refinement. A detailed structural characterization of the bacterial HSS of *B. viridis* (*Bv*HSS) with better resolution (PDB ID: 4PLP, 1.5 Å) and refinement statistics was recently performed (Krossa et al. 2016). The work additionally included structures of relevant single residue variants and qualitative activity assays to evaluate the reaction mechanism:

The *Bv*HSS structure shows a dimer with each subunit forming a boot-shaped substrate binding pocket between an “NAD(P)-binding Rossmann-like domain” and an “HSS-like domain”. The cofactor NAD^+ is thereby bound as prosthetic group and reaches into the binding pocket with its nicotinamide ring being part of the active site. Based on electrostatic surface calculations at pH >7, especially the residues D94 and E117 were proposed to attract and lead positively charged amine substrates from the entrance of the binding pocket into the active site. The electron density within the active site of one structure (PDB ID 4TVB) was interpreted as PUT in one subunit and as HSP in the other one. The residues coordinating to the amino groups of the two compounds were described and the locations of these amino groups were termed “amino sites”. The innermost nitrogen atoms N1 of PUT and N01 of HSP, placed at the “inner amino site”, are coordinated to the residues E210 and N162. The outermost nitrogen N11 of HSP is coordinated to residue E237 and oxygen O2D of NAD^+ (“outer amino site”). Both nitrogen atoms N2 of PUT and N06 of HSP are located at the “center amino site” between the residues N162 and H296 as well as between the ring planes of the W229 indole ring and the nicotinamide ring. These residues also surround the carbon atoms C4 of PUT and C05 of HSP, which play central roles in the reaction mechanism together with the adjacent nitrogen atoms. The “center amino site” therefore simultaneously represents/overlaps with the active site. Within the proposed reaction mechanism, the aromatic side chain of W229 stabilizes positively charged amino groups and partially charged carbons of reaction components through cation-π interaction. The nicotinamide ring of NAD^+ serves as hydride acceptor and donor, while residue H296 acts as proton acceptor and donor. The proposed reaction mechanism starts with residue H296, which forms a catalytic triad with the neighboring residues E237 and E298. It thereby becomes a strong base and deprotonates a water molecule. The resulting hydroxide ion subsequently deprotonates PUT N2 at the active site, followed by hydride transfer from carbon C4 of PUT to carbon C4N of NAD^+. PUT subsequently becomes an imine with a partially positive charge at C4, which is stabilized by cation-π interaction with the indole ring of W229. This facilitates the nucleophilic attack of a water or a hydroxide ion at PUT C4, causing deamination and generation of 4-aminobutanal. A partially positive charge at C4 of the (protonated) 4-aminobutanal could again be stabilized by cation-π interaction with residue W229. The nucleophilic

attack of the nitrogen atom of a second PUT at C4 results in release of a water molecule and Schiff base formation. Re-transfer of a hydride from NADH C4N to the carbon C05 of the Schiff base finally produces HSP and regenerates NAD^+.

Taken together, these structural observations convincingly distinguish the bacterial HSS from the eukaryotic HSS and DHS. The eukaryotic DHS catalyzes the transfer of an aminobutyl moiety from SPD (or HSP) either to the lysine of the eIF5a as main reaction (Park et al. 1981) or to a PUT molecule as side reaction to form HSP (Ober and Hartmann 1999a). After gene duplication of the DHS gene, the eukaryotic HSS evolved (Ober and Hartmann 1999b; Reimann et al. 2004) by losing the eIF5a-modifying activity. It retained the HSP-producing activity (Ober et al. 2003) and provides certain plants with HSP as precursor compound for the biosynthesis of pyrrolizidine alkaloids.

All three enzymes (bacterial HSS, eukaryotic HSS and eukaryotic DHS) require NAD^+ as cofactor and synthesize HSP. The crystal structure of human DHS exhibits an active site comparable to the bacterial HSS, formed by H288 as potential proton acceptor, W327 as cation-π interaction partner and the nicotinamide ring as hydride acceptor/donor (Umland et al. 2004). However, the aminobutyl moiety, originating from the substrate SPD (or HSP) is covalently bound as Schiff base to K329 as intermediate step of the DHS reaction mechanism (Wolff et al. 1997). This is in complete contrast to the reaction mechanism of the bacterial *Bv*HSS, which lacks a lysine residue in the binding pocket for such a covalent enzyme-substrate intermediate. In addition, the DHS forms tetramers with two active sites at the interface of two subunits (Umland et al. 2004). In contrast to this, each subunit of the bacterial HSS independently contains an active site. Consistent with these structural differences, the bacterial HSS is neither related to the eukaryotic DHS nor to the paralogous eukaryotic HSS.

1.4 Functions of polyamines

Research on PAs is complicated by their structural diversity, their unique distribution between and within (multicellular) species and their species-specific effects, which can be direct and indirect. In addition, an experimentally induced loss of one PA in an organism might be compensated by another PA, alternative biosynthesis pathways or transport systems. In context of these obstacles and considering the extensive ongoing research, the following chapter is intended to give a basic overview over the most important and profoundly described roles of PAs.

In eukaryotes, SPD plays an essential role in the hypusination of the eIF5a (Park and Wolff 2018). The enzymes deoxyhypusine synthase (DHS) and deoxyhypusine hydroxylase (DOHH) mediate the transfer of an aminobutyl moiety of SPD onto a lysine residue of the eIF5a to form hypusine. The modification of eIF5a enables the expression of certain genes on the level of translation elongation. A lack of this modification was shown to be lethal in eukaryotes (Park et al. 1998; Spradling et al. 1999; Sugimoto 2004; Chattopadhyay et al. 2008; Nishimura K et al. 2012).

The presence of SPM has more species-specific effects in eukaryotes. While it is not required for growth in yeast (Hamasaki-Katagiri N et al. 1998), mutations in the SPM synthase gene of mice (Gy mice) (Meyer RA. et al. 1998) and human (Snyder-Robinson syndrome) (Lauren Cason et al. 2003) cause severe physical and neurological defects.

Various other processes were shown to be influenced by PAs in eukaryotes, including their requirement in the progression of the cell cycle (Yamashita et al. 2013; Bae et al. 2018; Igarashi and

Kashiwagi 2019), their involvement in apoptosis (Stefanelli et al. 2000; Maccarrone et al. 2001; Salvi and Toninello 2004), their antioxidative properties (Ha et al. 1998; Mackintosh and Pegg 2000; Rider et al. 2007; Casero et al. 2018; Seifi and Shelp 2019) and role in aging (Minois 2014), their ability to modulate the immune system (Ferioli 2000; Handa et al. 2018; Madeo et al. 2018), glutamate receptors (Bowie 2018) and inwardly rectifying K^+-channels (Nichols and Lee 2018), their condensing effect on chromatin (Pasini et al. 2014) and their association with cancer (Casero et al. 2018; Sánchez-Jiménez et al. 2019).

While a certain PA typically has a similar function in most eukaryotes, the requirement and function for PAs in bacteria may be completely contrary in different species (Michael 2018). The growth of most bacteria is promoted by PAs (Patel et al. 2006; Lee et al. 2009; Green et al. 2011; Sakanaka et al. 2016; Becerra-Rivera et al. 2018; Sakanaka et al. 2018) and some bacteria even strictly depend on PAs for growth (Hanfrey et al. 2011; Kim SHo et al. 2016; Bontemps-Gallo et al. 2018; Burnat et al. 2018; Lowe-Power et al. 2018). For example, the aerobic growth rate of *E. coli* is reduced in the absence of PAs (Linderoth and Morris 1983; Chattopadhyay MK. et al. 2009) and long chain as well as branched PAs are essential for growth at high temperatures in the extreme thermophile *T. thermophilus* (Ohnuma et al. 2005; Nakashima et al. 2017). In complete contrast, *S. aureus* lacks polyamine biosynthesis genes and suffers growth inhibition or even death when confronted with exogenous PAs (Joshi et al. 2011). Other functions in bacteria comprise the covalent incorporation of PAs into the cell wall for cell integrity (Kamio et al. 1981; Kamio et al. 1986; Hirao et al. 2000; Hamana et al. 2002), assembly of siderophores (Ong et al. 1979; Griffiths et al. 1984; Oves-Costales et al. 2007; Baars et al. 2018), positive (Karatan et al. 2005; Patel et al. 2006; Lee et al. 2009; McGinnis et al. 2009; Burrell et al. 2010; Wortham et al. 2010; Hobley et al. 2014; Hobley L et al. 2017; Sobe et al. 2017) and negative (Ding et al. 2014; Wang et al. 2016; Kera et al. 2018) effects on biofilm formation and protection against reactive oxygen species (Khan and Di Mascio et al. 1992; Khan and Mei et al. 1992; Chattopadhyay MK. et al. 2003; Kim et al. 2006) and acidic environments (Park YK. et al. 1996; Jung and Kim 2003; Lee YHeon et al. 2007; Moreau 2007).

In conclusion, the role of PAs in bacteria may not be generalized, ranging from essential to dispensable or even bactericidal. Profound assumptions regarding a certain species require close inspection of PA-biosynthetic enzymes, catabolic enzymes, transport systems and compensatory mechanisms to reveal potential functions of individual PAs.

1.5 *P. aeruginosa* as pathogen

P. aeruginosa is a gram-negative bacterium naturally found in the soil and on surfaces in aqueous environments (Ramos 2004). It can live on various hydrocarbon compounds (Frimmersdorf et al. 2010) and is able to grow anaerobically by denitrification (Borrero-de Acuña JManuel et al. 2017). While *P. aeruginosa* is commonly no threat to healthy individuals, it causes severe infections as opportunistic pathogen in immunocompromised patients with high risk of lethality (Lynch et al. 2017). Due to its additional ability to form biofilms on medical equipment, e.g. ventilator tubing (Adair et al. 1999) and catheters (Peters et al. 1981), it consistently plays a dominant role in nosocomial infections (Zarb P et al. 2012; Magill et al. 2014). Pseudomonal infections often affect surgical or burn wounds (Zhang and Liu 2015), the urinary tract (Morata et al. 2012), the blood system (Scheetz et al.

2009) and especially the respiratory system (Kollef et al. 2014). The combination of a weakened immune system and the emergence of multi- or even pan-resistant strains (Horcajada et al. 2019) severely complicates treatment and results in chronic infections with poor prognosis. Best-known chronic lung infections by *P. aeruginosa* occur in cystic fibrosis (CF) patients (Malhotra et al. 2019), which persist for decades causing inflammatory damage to the lung tissue and ultimately fatal outcome.

P. aeruginosa is equipped with numerous properties to provide high adaptivity to the environment, evasion of the immune system and resistance to antibiotics. A single polar flagellum and several type 4 pili enable motility and adhesion on surfaces and tissue (Köhler et al. 2000; Craig et al. 2004). The outer membrane of the pathogen exhibits low permeability for hydrophilic molecules like antibiotics (Nicas and Hancock 1983), which can exclusively pass through the porins. Antibiotics reaching the cytosol are effectively removed by membrane efflux pumps (Masuda et al. 2000). The pathogen also contains a chromosomal β-lactamase (AmpC) (Normark 1995), which is secreted into the periplasm. The outer leaflet of the outer membrane is further composed of lipopolysaccharide (LPS), comprising the membrane-anchored lipid A, a polysaccharide core region and optionally a variable O-specific polysaccharide (O-antigen) (Lam et al. 2011). LPS molecules are electrostatically connected via divalent cations (e.g. Mg^{2+}) and provide a polar shield against hydrophobic antibiotics (Vaara 1992). The bacterium senses and adapts to environmental conditions via three quorum-sensing systems (Lee and Zhang 2015) and a multitude of two-component regulatory systems (TCS) (Gooderham and Hancock 2009). TCS are pairs of stimulus-detecting, membrane bound histidine kinases and cytoplasmic, DNA-binding response regulators. Several TCS were shown to mediate virulence, biofilm formation and antibiotic resistance among others (Gooderham and Hancock 2009). For example, the PhoPQ and PmrAB TCS sense low Mg^{2+} concentrations (McPhee et al. 2006), presence of polycationic peptides (e.g. cationic peptide antibiotics (Moskowitz et al. 2004)) or low pH (Mulcahy et al. 2008) and subsequently activate the *arnBCADTEF-ugd* operon (also termed *pmrHFIJKLM*). As adaptive result, 4-amino-4-deoxy-L-arabinose (Ara4N) is added to the phosphates of the lipid A moiety of LPS (Gooderham and Hancock 2009; Lo Sciuto and Imperi 2018; Tierney and Rather 2019), which reduces the negative charge of the LPS and consequently decreases binding of cationic antimicrobial peptides.

P. aeruginosa further harbors a large arsenal of virulence factors, which are secreted from the bacterium especially in the initial phase of infection via type II (Lindgren and Wretlind 1987; Martínez et al. 1999; Sandkvist 2001) and type III (Hauser 2009; Galle et al. 2012) secretion systems (T2SS, T3SS). The T3SS thereby forms a needle-like structure and a pore within the host membrane to directly transfer effector proteins from the bacterium into the host cell, leading to disruption of the host cytoskeleton. This mechanism is used to attack epithelial cells (Berube et al. 2016) and as defense against immune cells (Diaz et al. 2008).

The main response of the host immune system in respiratory infections is thought to comprise the recognition of the pathogen via e.g. toll-like receptors, triggering of an inflammation reaction and eradication of the pathogen by attracted neutrophils (Maurice et al. 2018). If both the immune system and antibiotic treatment fail to defeat the bacteria, as especially seen in CF patients, *P. aeruginosa* infection becomes chronic (Faure et al. 2018). Accumulating bacteria form microcolonies and a biofilm

by embedding themselves in extracellular polymeric substances, composed of polysaccharides, nucleic acids, lipids, and proteins (Ciofu and Tolker-Nielsen 2019). This transition from planktonic to sessile biofilm lifestyle drastically increases the resistance of the pathogen against antibiotics and the immune system. The biofilm hinders diffusion of certain antibiotics (Walters et al. 2003; Tseng et al. 2013), movement of immune cells (Jesaitis et al. 2003) and the activation of the complement system (Pier et al. 2001). Even more, *P. aeruginosa* constantly adapts within the biofilm by phenotypic and genetic changes to outlast the immune response and antibiotic treatment. It decreases its recognition by immune cells by removal of its pili (Kresse et al. 2003), the flagellum (Patankar et al. 2013), the O-antigen (Hancock et al. 1983) and by modification of lipid A (Ernst et al. 2006) to alleviate inflammation reactions. Nutrient and oxygen limitations slow the bacterial metabolism down, which contributes to antibiotic resistance (Ciofu and Tolker-Nielsen 2019). A sub-population of cells may completely arrest metabolism to become so-called persister cells (Jesaitis et al. 2003; Lewis 2010), making them almost invulnerable to antibiotics. Prolonged exposition to antibiotics promotes selection of resistant strains, which acquire resistance via horizontal gene transfer (Klockgether et al. 2011) or chromosomal mutations due to oxidative stress (Boles and Singh 2008; Dettman et al. 2013). Various resistances were shown to result from mutations, causing overproduction of the endogenous β-lactamase or efflux pumps, loss of outer membrane porins or alteration of antibiotic targets like the DNA gyrases or type IV topoisomerases (Horcajada et al. 2019). These processes promote the evolution of different strains within the same host and ultimately the emergence of pan-resistant strains.

1.6 Polyamine metabolism in *P. aeruginosa*

The interplay of polyamine biosynthesis pathways, membrane transport systems and inhibitory compounds in *P. aeruginosa* is shown in Figure 3. The genomic locus tags given in this chapter refer to the nomenclature of the pseudomonas genome database (www.pseudomonas.com).

In *P. aeruginosa*, PUT can be produced from decarboxylation of both ornithine and arginine via the ODC (PA4519) pathway and the ADC (PA4839)/AIH (PA0292)/NCPAH (PA0293) pathway (chapter 1.2.1, p. 1) (Nakada and Itoh 2003). Ornithine is thereby endogenously synthesized from glutamate (Lu 2006; Xu et al. 2007). In addition, two acetylpolyamine amidohydrolases (APHs, PA0321 and PA1409) were demonstrated to deacetylate acetyl-PAs and were suspected to compensate for NCPAH by hydrolysis of N-carbamoylputrescine (Krämer et al. 2016).

CAD is generated by the LDC (PA1818) (Chou et al. 2010) and a gene encoded within the same operon as the decarboxylase was proposed to be a lysine:CAD antiporter (PA1819), albeit not experimentally shown (Chou et al. 2010).

PUT serves as substrate for the dcSAM-dependent (provided by SAM decarboxylase, SAMDC, PA0654) generation of SPD via SPD synthase (PA1687) and of HSP via HSS (CIA_02171 in PA14, PSPA7_3061 in PA7, not present in PAO1). A SPD dehydrogenase (SPDDH, PA3713) was shown to cleave both SPD and SPM, releasing 4-aminobutanal and DAP in case of SPD and 3-aminopropanal and SPD in case of SPM (Dasu et al. 2006).

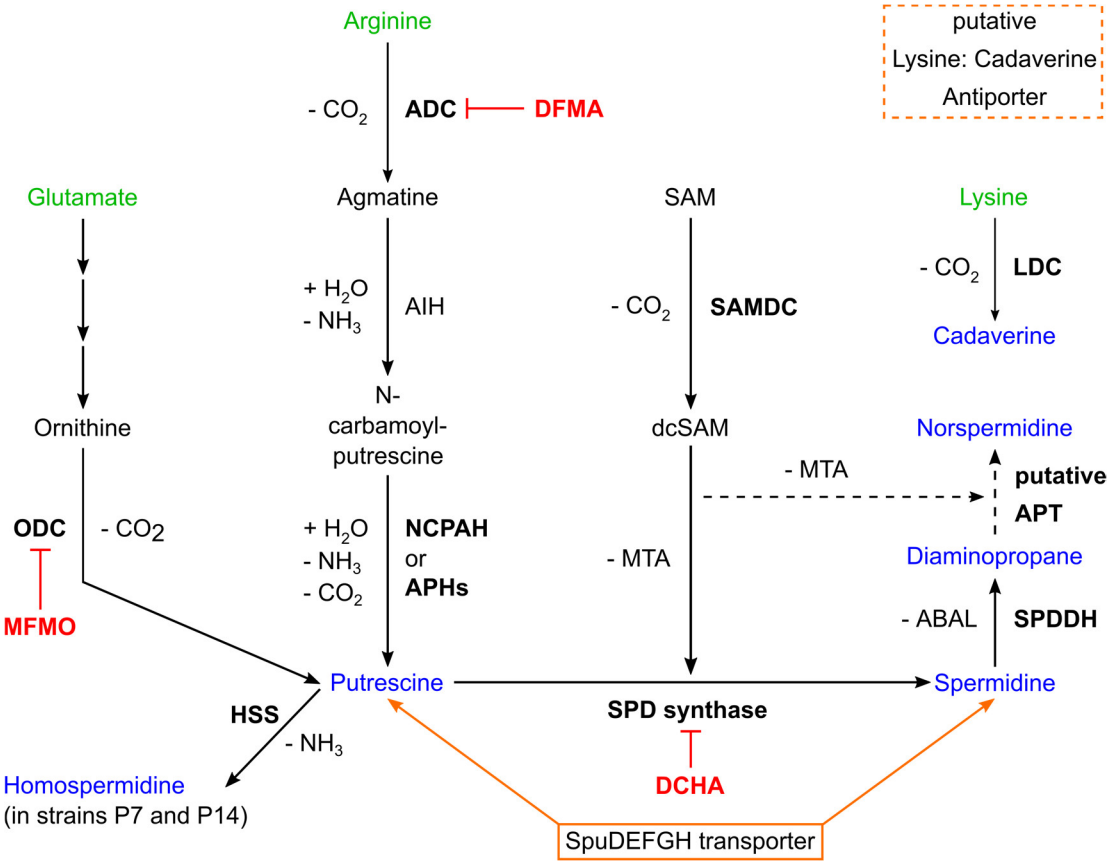

Figure 3: PA biosynthesis, membrane transport and synthetic inhibitors in *P. aeruginosa*.
Membrane transporters and transport routes are depicted in orange, amino acids are colored green, PAs are blue and synthetic inhibitors are red. The HSS gene is present in the strains PA7 and PA14, among others. The presence of the putative lysine:CAD antiporter remains to be experimentally proven and is therefore framed with a dotted line. The PA4774 gene product (putative APT) was suggested to synthesize external SPD as inducible, additional SPD synthase in one work (Johnson et al. 2012) and attributed for synthesis of external NSPD as aminopropyltransferase (APT) in another work (Bolard et al. 2019). The biosynthesis pathway of NSPD using DAP and dcSAM accordingly remains to be confirmed and is shown as dotted arrow. ABAL: 4-aminobutanal, ADC: arginine decarboxylase, AIH: agmatine deiminase, APH: acetylpolyamine amidohydrolases, APT: aminopropyltransferase, DCHA: dicyclohexylammonium sulphate, DFMA: DL-α-(Difluoromethyl)arginine, dcSAM: decarboxylated SAM, HSS: homospermidine synthase, LDC: lysine decarboxylase, MFMO: DL-α-monofluoromethylornithine, MTA: methylthioadenosine, NCPAH: N-carbamoylputrescine amidohydrolase, SAM: S-adenosylmethionine, SAMDC: SAM decarboxylase, SPD: spermidine, SPDDH: SPD dehydrogenase. The corresponding genomic locus tags are given in the text below.

Never found in *P. aeruginosa* before, very recent research detected NSPD in cell surface extracts of a mutant *P. aeruginosa* strain (Bolard et al. 2019). The PA4774 gene product, which was annotated as additional SPD synthase so far, was thereby proposed to function as aminopropyltransferase (APT) to form NSPD from DAP and dcSAM.

The two irreversible inhibitors DL-α-(Difluoromethyl)arginine (DFMA) (Kallio et al. 1981) and DL-α-monofluoromethylornithine (MFMO) (Kollonitsch et al. 1978) inhibit ADC and ODC, respectively, and dicyclohexylammonium sulphate (DCHA) (Hibasami et al. 1980) competitively inhibits the SPD synthase.

Apart from endogenous synthesis, PAs from the environment are taken up by an ABC-type transport

system (SpuDEFGH, PA0300-PA0304) (Lu et al. 2002), which was shown to preferentially bind SPD but also PUT. Besides other potential PA cargo, SPM was additionally suggested to be transported based on experimental evidence.
Catabolism of PAs is accomplished via the γ-glutamylation pathway, which provides various enzymes for the deamination of different PAs on their way into the tricarboxylic acid cycle (Yao et al. 2011). *P. aeruginosa* is consistently able to use PAs as sole carbon and nitrogen source.

1.7 Effects of polyamines on *P. aeruginosa*

The following results of previous research are mainly based on experiments with the *P. aeruginosa* lab strain PAO1. Findings are not necessarily reproducible in all strains and especially clinical isolates were occasionally shown to behave differently.
To evaluate the need for PAs for growth of *P. aeruginosa*, various enzymes of the polyamine biosynthesis network were inhibited with the above-mentioned inhibitors. Interference with a single PUT synthesis pathway (ADC or ODC) did not change the cellular PUT level as it was compensated by the other (Kallio and McCann 1981). Only simultaneous inhibition of ADC, ODC and SPD synthase using DFMA, MFMO and DCHA in minimal medium significantly reduced the cellular concentration of PUT and SPD by 80 % and 95 %, respectively, and caused the generation time to increase by 70 % (Bitonti et al. 1982). Although potential synthesis of other PAs like CAD was not excluded by this approach, limitation of PA concentrations was at least shown to decrease the growth rate.
Apart from the role in growth, the involvement of PAs in biofilm formation was inspected in some strains. In the strain PAO1, AGM is converted via AIH and NCPAH into PUT using the gene products of PA0292 and PA0292, respectively (Nakada and Itoh 2003). In the strain P14 and 25 % of clinical isolates, an additional operon was detected for this pathway (PA14_48490: AIH, PA14_48450: AIH with twin-arginine translocation signal sequence, PA14_48470: NCPAH, PA14_48460: polyamine binding/transport protein) along with the regular one (Williams et al. 2010). The activity of the two cloned AIH proteins (PA14_48490 and PA14_48450) was proven and the secretion of the latter one experimentally shown. This operon was demonstrated not to compensate for the regular operon in terms of growth but to be induced by exogenous AGM in the stationary phase and to promote biofilm formation. Since macrophages secrete AGM upon contact with endotoxins, this additional operon was proposed to be an adaption mechanism to sense inflammatory environments and promote biofilm formation for survival.
Another interesting finding was the connection between the PA transporter and virulence. Knockout of any of the PA transporter genes (*spuDEFGH*) disrupted the utilization of SPD (but not PUT) as sole exogenous carbon and nitrogen source (Lu et al. 2002). Even more, these mutants were characterized by reduced expression of the T3SS (Zhou et al. 2007), which allows *P. aeruginosa* to translocate effector proteins into host cells during infections. Apart from providing *P. aeruginosa* with exogenous PAs, the sensing of exogenous host PAs and subsequent induction of T3SS was consequently proposed to be another role of the SpuDEFGH transporter. Aiming to reduce the expression of T3SS and therefore decrease the pathogenicity of *P. aeruginosa*, various compounds were developed to inhibit the transporter or the subsequent induction mechanisms of the T3SS genes (Anantharajah et al. 2016; Wang J et al. 2018).

Other studies revealed the importance of PA homeostasis to prevent excess PA burden. PA catabolism is mediated by the γ-glutamylation pathway in *P. aeruginosa* (Yao et al. 2011). Interestingly, knockout of the glutamylpolyamine synthetase PauA2 belonging to this pathway abolished catabolism of both SPD and SPM (Yao et al. 2012). Both PAs subsequently became bactericidal when exogenously applied. This would make PauA2 a promising therapeutic target, since physiological SPM concentrations present in human plasma were demonstrated to exert bactericidal effects on *pauA2* mutants.

Intensive research was dedicated to the link between PAs and the susceptibility to antibiotic compounds in *P. aeruginosa*. In general, exogenous PAs (especially SPD but partly also SPM, PUT, CAD, AGM) were discovered to increase the minimal inhibitory concentration (MIC) of cationic antimicrobial peptides, aminoglycosides, quinolones (Kwon and Lu 2006b) (except for nalidixic acid (Kwon and Lu 2006a)) and imipenem (Kwon and Lu 2007). Based on gene chip analysis and knockout experiments, the effect of SPD was associated with the PhoPQ TCS (but not with the PmrAB TCS) and the *arnBCADTEF-ugd* operon (Kwon and Lu 2006b), responsible for 4-aminoribosylation of lipid A. The increased SPD-induced resistance was thereby independent of the SpuDEFGH transporter in case of cationic antimicrobial peptides but dependent on the transporter in case of the aminoglycosides and quinolones (Kwon and Lu 2006b). The protective function of SPD accordingly seemed to be exerted intra- and extracellularly, depending on the antibiotic compound and its mode of action.

In complete contrast, exogenous PAs (SPD, SPM, PUT, CAD) decreased the MIC of numerous β-lactam antibiotics (except for imipenem (Kwon and Lu 2007)), chloramphenicol, nalidixic acid and trimethoprim i.e. increased the susceptibility of *P. aeruginosa* to these antibiotics (Kwon and Lu 2006a). The effect was neither caused by destabilization of the membranes nor by inhibition of the pseudomonal AmpC β-lactamase (Kwon and Lu 2006a).

Very complex and possibly strain- and concentration-dependent effects of NSPD on *P. aeruginosa* were discussed and remain to be fully elucidated. NSPD negatively interferes with biofilm formation in several bacteria, including *P. aeruginosa* (Qu et al. 2016; Cardile et al. 2017). Depending on the application of exogenous NSPD, pseudomonal biofilm formation was reduced, the biofilm was disassembled, or NSPD even exerted bactericidal effects. However, the required concentrations of NSPD for these effects varied in different publications and were considerably high (5-20 mM). In comparison, physiological triamine concentrations in bacteria are lower (1-3 mM) (Cohen 1998). Furthermore, NSPD concentrations of >5 mM were demonstrated to be cytotoxic for human cells (Cardile et al. 2017), not qualifying NSPD as potential antibiotic compound. In addition, NSPD contrarily promoted biofilm formation in some clinical isolates (Cardile et al. 2017).

The question of actual biosynthesis of NSPD in *P. aeruginosa* is further complicated by two publications, which inspected the PA4773-5 gene cluster in response to induction by the PmrAB TCS (which also promotes lipid A modification via the *arn* operon). In the earlier study, the PmrAB TCS was shown to upregulate the PA4773-5 gene cluster after exogenous activation (Johnson et al. 2012). Mutants lacking the PA4774 gene revealed absence of extracellular SPD along with higher susceptibility to antibiotics (polymyxin and aminoglycoside) and oxidative stress. PA4774 was consequently suggested to code for an additional SPD synthase and protective effects were attributed

to extracellular SPD, among others. A more recent publication inspected a *pmrAB* mutant strain which constitutively induced the expression of the PA4773-5 gene cluster (Bolard et al. 2019). Increased resistance against antibiotics (polymyxin and aminoglycosides) was confirmed but elevated extracellular concentrations of both NSPD and SPD were detected in the *pmrAB* mutant. Deletion of the mutant *pmrAB* genes significantly reduced extracellular NSPD levels but had little effect on the elevated extracellular SPD levels. While polymyxin resistance was demonstrated to require the *arn* operon, the increased aminoglycoside resistance was dependent on both the MexXY efflux pump and the PA4773-5 gene cluster. Concluding, the PA4774 gene product was proposed to be an aminopropyltransferase and to synthesize NSPD instead of SPD using SAM and DAP. Elevated aminoglycoside resistance was therefore attributed to extracellular NSPD together with the functional MexXY pump.

Taken together, both the presence and role of NSPD along with the function of the PA4774 gene product remain to be unambiguously elucidated in *P. aeruginosa*.

1.8 Cation-π interaction

The non-covalent binding of a cation to a π-electron system is termed cation-π interaction (Dougherty 1996). This interaction was first reported between K^+ and benzene in gas phase based on both mass spectrometry measurements and quantum mechanical calculations (Sunner et al. 1981). The electron density distribution of benzene with its delocalized π-electrons is described as quadrupole moment (Hill and Smith 1951; Vrbancich and Ritchie 1980) with positive partial charge within the carbon ring plane and negative partial charge below and above the plane due to the π-electron cloud. Cation-π interactions can sufficiently be explained by electrostatic models considering the attraction between the negative partial charge of the π-system and the positive charge of the cation (Mecozzi et al. 1996a; Mecozzi et al. 1996b). The bonding energy depends on the cation (Reddy and Sastry 2005), the characteristics of the π-system (Mecozzi et al. 1996a; Vijay and Sastry 2008), the interaction geometry and the solvent polarity (Marshall et al. 2009; Du et al. 2012). The binding energy is thereby in the range of hydrogen bonds and salt bridges in aqueous solution (Pletneva et al. 2001).

In the biological context, cation-π interactions occur between a multitude of interaction partners. Participating cations include metal ions (Xue et al. 2008; Pan et al. 2010), basic amino acids (Burley and Petsko 1986), and e.g. reaction intermediates (Faraldos et al. 2011), while biological π-system include aromatic amino acids (Burley and Petsko 1986), nucleobases (Horvath et al. 1998) and cofactors (Collard et al. 2011). Three different online tools were developed to find cation-π interactions in PDB protein structures based on different search criteria (Gallivan and Dougherty 1999; Martz 2002; Reddy AS et al. 2007). Cation-π interactions were shown to stabilize protein structures, protein-protein, protein-ligand and protein-DNA complexes and to be involved in enzymatic reactions (Zacharias 2002; Crowley and Golovin 2005; Mahadevi and Sastry 2013).

1.9 Structure determination by X-ray crystallography

The following chapters give a brief introduction into textbook knowledge about the principles, the experimental approaches and quality criteria of structure determination by X-ray crystallography (Rhodes 2009; Rupp 2010). An own chapter was dedicated to the phasing method “molecular replacement” (chapter 1.9.3, p. 15), which allowed to obtain initial phase values for the structures presented in this thesis.

1.9.1 Principle of X-ray diffraction

Structure determination of biomolecules by X-ray crystallography is principally based on the scattering of X-rays by electrons. X-rays are electromagnetic waves composed of both an electric and a magnetic field. The electric field causes oscillation of the electrons in the biomolecule, which in turn generates the scattered X-rays due to dipole radiation. X-ray crystallography thereby makes use of elastic scattering, in which the wavelength of incoming and scattered waves remains the same.
As prerequisite for structure determination, the biomolecule needs to be crystallized. Such a crystal is composed of non-covalently interacting biomolecules, which form a uniform, periodic array of electron density in all three dimensions of space. The periodicity of the electron density distribution can be described as crystal lattice with the so-called “unit cell” as building block, which is translationally repeated along the three crystal axes. The lattice causes a unique interference of scattering X-rays, resulting in a discrete diffraction pattern. The position and intensity of these diffracted X-rays, also called reflections, are recorded as spots on a detector.
It can mathematically be shown that each reflection originates from a set of (imaginary) planes, which cut through the unit cell. Each unique set is composed of parallel, equidistant planes with each plane containing the same average electron density. Each set of planes and the corresponding reflection are named by the same “Miller indices” h, k and l. The three Miller indices are integers, which equal the number of times the unit cell edges a, b and c are cut by the set of planes. The Bragg’s law describes the diffraction conditions, under which an X-ray of wavelength λ multiplied by an integer n is reflected by a certain set of planes (hkl) with corresponding interplanar distance d_{hkl} at an angle θ:

$$2d_{hkl}\, sin\theta = n\lambda \tag{1}$$

The angle θ is spanned by the reflecting plane and both the incoming and the scattered X-ray. The left part of the equation basically expresses the path difference and therefore the phase difference between X-rays diffracted from different planes of the same set at an angle of θ. If this difference equals an integer n of the X-ray’s wavelength, diffracting X-rays interfere constructively and produce a detectable reflection. In other words, all X-rays reflected by a set of planes at an angle of θ are in phase. If the equation is not met, destructive interference of diffracted X-rays prevents emergence of a reflection.
A reflection can be described by a complex number, the so-called structure factor F_{hkl}:

$$F_{hkl} = |F_{hkl}|e^{i\alpha_{hkl}} \tag{2}$$

Each reflection is thereby characterized by an amplitude $|F_{hkl}|$ and a phase α_{hkl}. $|F_{hkl}|$ is proportional to

the square root of the reflection intensity, which is recorded on the detector. The phase α, however, cannot be measured and needs to be determined later (chapter 1.9.2).

The goal of structure determination is the construction of a model of the biomolecule by defining the positions of (preferably) all atoms. This is achieved by interpretation of the three-dimensional distribution of the electron density, which is calculated by a Fourier sum:

$$\rho(x,y,z) = \frac{1}{V}\sum_{h}\sum_{k}\sum_{l} |F_{hkl}|\, e^{i\alpha_{hkl}} e^{-2\pi i(hx+ky+lz)} \qquad (3)$$

The coordinates x, y and z define the location of the electron density ρ within the unit cell of volume V. All structure factors defined by the Miller indices (h, k, l) of the corresponding reflections are included in the Fourier sum.

Concluding, calculation of the electron density distribution is based on the combination of all structure factors, which carry the information of the electron density distribution on sets of parallel, equidistant planes. The electron density along the planes is thereby distributed in wave form with density maxima and minima. Combination of differently orientated and distanced sets of planes with respective electron densities sums up to the three-dimensional electron density distribution within the unit cell. However, only the average electron density along sets of planes can experimentally be determined by measuring the intensity of the reflections. The precise position of the wave-like density distribution requires knowledge of the phase value of each reflection/structure factor. Since this phase value α cannot be measured, Equ. 3 cannot be solved, causing the well-known phase problem in X-ray crystallography.

1.9.2 Solving the phase problem

Calculation of the electron density distribution ρ(x, y, z) according to Equ. 3 requires knowledge of the phase angle α of each scattered X-ray. These phase values depend on the locations of the scatterers within the unit cell, which are not known and are the actual goal of the whole structure determination effort. Different phasing methods were developed to circumvent this complication.

For small molecules, the locations of atoms can be determined by direct methods. These include trial-and-error placing of the atoms at varying locations and evaluation of each trial-solution by comparing its calculated diffraction pattern (Equ. 7, p. 17) with the experimental diffraction pattern. Obviously, the number of possible arrangements increases with the number of atoms and demands too much computational effort for larger molecules. Another direct method makes use of mathematical approximations, which relate the phase angles of structure factors with their indices.

Phasing methods for larger molecules mostly provide mere estimates of phase values for only a subset of reflections. These methods include isomorphous replacement, anomalous dispersion and molecular replacement.

Isomorphous replacement describes the introduction of a strong scatterer into identical sites of each unit cell without distortion of the “native” crystal lattice (isomorphism). This is accomplished by soaking of heavy atoms into the “native” crystal or by incorporation of selenomethionine into the protein during translation. Strong scatterers influence the intensity of the reflections and their contribution is reflected by the difference between the diffraction pattern of the “native” crystal and the “derivative” crystal. This

intensity difference of reflections is used to locate the position of the strong scatterers in the unit cell by the Patterson function (insert $[|F_{hkl}^{heavy}|-|F_{hkl}^{native}|]^2$ for $|F_{hkl}|^2$ in Equ. 4, p.16) or by direct methods. Knowledge about the position of the strong scatterers allows calculation of the phase value of its contribution to the derivative scattering factors and consequently to estimate the phase values of the "native" reflections by e.g. Harker diagrams.

Anomalous scattering describes the wavelength-dependent difference of Friedel pair intensities (I_{hkl} and $I_{\overline{hkl}}$) due to gain of real and imaginary anomalous scattering contributions to the structure factors. This phenomenon occurs near the element-specific X-ray absorption edge. The experimental setup therefore requires tuning of the exciting X-ray wavelength to address corresponding elements. Since the absorption edges of carbon, nitrogen and oxygen are not in the experimentally used range of X-ray wavelengths, heavier elements need to be present in the biomolecule. Again, the location of these anomalous scatterers and therefore the phase angle of their contribution to the structure factors can be determined by Patterson function (Equ. 4, p. 16) or direct methods. Measurement of anomalous scattering at varying wavelengths at and around the absorption edge changes the wavelength-dependent anomalous contributions to the structure factors, further facilitating determination of initial phase values by e.g. Harker diagrams.

Since both isomorphous replacement and anomalous dispersion require the presence of heavy atoms, these methods can be combined to increase the quality of the estimated phase angles. However, these methods entail preparation of different derivative crystals and/or collection of multiple diffraction patterns. A far less labor-intensive method, normally not requiring any additional experimental efforts, is termed molecular replacement.

1.9.3 Phasing by molecular replacement

Molecular replacement is based on the phase angles of a known structure, the so-called phasing model. These phase angles serve as initial phase estimates for the unknown target structure. For molecular replacement to be successful, the phasing model needs to exhibit low root-mean-square distances (RMSD) from the target structure. High identity on the level of amino acid sequence between model and target is thereby assumed as indicator for structural similarity. As rule of thumb, albeit not guaranteeing success, a sequence identity of at least 40 % should be provided. Parts of the model, which are suspected to highly differ from the target structure, should rather be omitted. Having chosen an appropriate phasing model, this is used to computationally replace the target structure within its unit cell. Therefore, the number of target molecules in the unit cell, their orientation and the location of each molecule need to be matched by the phasing model. Knowing the volume of the target's unit cell, the size of the target molecule in terms of amino acid sequence and typical values for the solvent content in protein crystals, the number of target molecules in the unit cell can be estimated by the Matthew's coefficient (Matthews 1968). Correct orientation and placing of model molecules require definition of six parameters, three spatial coordinates (x, y, z) and three rotation angles (φ, ϕ, χ). To minimize the computational effort by decreasing the combinational possibilities of this search, the rotation search and translation search can simply be separated.

This is possible by first defining the rotation angles with the Patterson function (Patterson 1934):

$$P(u, \mathrm{v}, \mathrm{w}) = \frac{1}{V} \sum_{h} \sum_{k} \sum_{l} |F|^2_{hkl}\, e^{-2\pi i(hu+kv+lw)} \tag{4}$$

In contrast to Equ. 3, the Patterson function does not require the individual phase values α_{hkl}. Thus, computation of the Patterson map P(u, v, w) is possible only knowing the measured intensities of the target structure (which are proportional to the squares of the amplitudes |F|). The Patterson map is an autocorrelation of the electron density distribution, basically showing peaks corresponding to tips of interatomic vectors. The orientation of intramolecular vectors depends on the orientation of the corresponding molecule, but not on its location in the unit cell. To align a model molecule with a target molecule, the Patterson functions of both the model and target are calculated. One Patterson map is then incrementally rotated around the three rotation axes (φ, ϕ, χ) and the product of model and target map is integrated. Maximal values hint at correct rotational alignment of model and target structure:

$$R(\phi, \varphi, \chi) = \int_{u,v,w} P^{target}(u, v, w)\; P^{model}\{(u, v, w) \times [\phi, \varphi, \chi]\}\, du\, dv\, dw \tag{5}$$

Subsequently, the location of the correctly rotated phasing model in the unit cell of the target needs to be determined. This translation search entails trial-and-error placing of the phasing model and calculation of the corresponding diffraction pattern (Equ. 7, p.17). Minimal difference between this model diffraction pattern and the target diffraction pattern, as evaluated by the R-factor (Equ. 8, p. 18), indicates a correct solution.

1.9.4 Structure refinement

Having measured the intensity of the diffracted X-rays and obtained initial phase estimations, the first electron density distribution can be computed according to Equ. 3. However, initial phase values are often too bad to yield an interpretable electron density distribution. Thus, refinement methods are required to improve the phase angles, while the measured reflection intensities remain the same.

Initially, density modification methods including solvent flattening (Wang 1985), histogram matching (Zhang and Main 1990) and non-crystallographic symmetry averaging are applied to improve the initially calculated electron density distribution. Solvent flattening makes use of the considerably large solvent regions within a protein crystal, which should have a uniformly low density. The solvent density of the initial map is therefore set to a uniform, low value to remove noisy variations or even artificial, negative densities. In histogram matching, the resolution-dependent electron density distribution of the initial map is matched with the characteristic distribution of refined, high-quality maps. Non-crystallographic symmetry averaging entails the averaging of the electron density distribution of multiple identical molecules within the asymmetric unit to increase the signal-to-noise ratio.

Improvement of the electron density distribution, representing the real-space, simultaneously improves the phase estimates and thereby the structure factors, representing the reciprocal-space. This relation is mathematically based on the Fourier transform operation. The electron density distribution (Equ. 3) is the Fourier transform of the structure factors and vice versa.

The electron density distribution can accordingly be back-transformed into structure factors:

$$F_{hkl} = \int_x \int_y \int_z \rho(x,y,z) e^{2\pi i(hx+ky+lz)} dx\, dy\, dz \tag{6}$$

These calculated structure factors are composed of (hopefully) improved phase estimates and calculated amplitudes, which are compared to the experimental amplitudes (measured as reflections). Calculated amplitudes should thereby converge to the measured ones during structure refinement (R-factor, Equ. 8, p. 18), which serves as quality control for phase improvement. To prevent major bias caused by a refinement step, old and new phase values are combined before calculation of the (hopefully) improved electron density distribution. A qualitatively adequate electron density distribution can subsequently be interpreted by fitting of the atoms of the unknown structure into the density. Structure factors of this current model can equivalently be calculated by a Fourier sum of the contributions of all scattering atoms f_j at positions x_j, y_j, z_j:

$$F_{hkl} = \sum_{j=1}^{n} f_j e^{2\pi i(hx_j+ky_j+lz_j)} \tag{7}$$

The atomic scattering factor f_j represents an element-specific function to describe the respective atom as sphere of electron density.

Structure refinement is proceeded by improving both the fit of the atomic model to the electron density distribution in real-space and by reciprocal-space methods. Reciprocal-space methods include weighting of phases according to their reliability (figure of merit) and refinement of atomic positions guided by minimization of the difference between measured and calculated amplitudes. In real-space, *a priori* knowledge is used to minimize computational efforts by reducing the possibilities for atom placement. The amino acid sequence of the unknown structure and their ideal geometric values are known. Constraints and restraints are defined for e.g. bond lengths, bond angles, torsion angles peptide bond planarity and occupancies. At later stages of refinement and especially for high-resolution structures, these constraints and restraints can be relaxed to reveal physiological deviations from ideal geometry values. At some point, the model is maximally refined to fit the experimental data.

1.9.5 Quality criteria in X-ray crystallography

The collection of the diffraction pattern(s) can be considered as last experiment in structure determination. The measured intensities carry structural information and serve as benchmark for quality control. However, random and systematic errors compromise the measurement of reflection intensities, which will ultimately limit the quality of the electron density distribution. Initial phases cannot be accurately measured but are error-prone estimates. Phases from molecular replacement thereby impose a particular complication, the well-known “model bias”. While initial phase estimates from other methods simply deteriorate the electron density distribution, phases from molecular replacement transfer features of the phasing model into the electron density distribution of the target model, which need to be removed during structure refinement. Concluding, both the quality of the diffraction data and the reliability of the model need to be evaluated, which can be done by a multitude

of indicators.

The probably best-known indicators for model quality are R_{work} (Jensen 1985) and R_{free} (Brünger 1992):

$$R = \frac{\sum_{hkl} \left| \left|F_{hkl}^{obs}\right| - \left|F_{hkl}^{calc}\right| \right|}{\sum_{hkl} \left|F_{hkl}^{obs}\right|} \tag{8}$$

These R-factors represent the agreement of the model's amplitudes $|F^{calc}|$ with the experimental amplitudes $|F^{obs}|$. R_{work} takes all amplitudes into account which were used for refinement, the "working set". However, $|F^{obs}|$ is thereby both part of the structure refinement process and benchmark for quality control. To prevent overfitting of the model to the data, R_{free} is additionally calculated for cross-validation to reflect the accuracy of the model. R_{free} only considers a "test set" of amplitudes, usually comprising 5-10 % of the data set, which is not used for refinement.

On the side of diffraction data quality, the strength of reflection intensities can be quantified by the averaged signal-to-noise ratio $\langle I/\sigma I \rangle$. However, $\langle I/\sigma I \rangle$ can vary between different data processing software, because σ is calculated according to an error model. Also depending on the respective error model, another indicator $\langle I/\sigma I \rangle_{asymptotic}$ or ISa can be calculated (Diederichs 2010). ISa represents the theoretical maximum value of $\langle I/\sigma I \rangle$ achievable by the experimental setup. The reciprocal of ISa may be considered as the systematic instrument error contribution.

Another R-factor for the evaluation of data quality is the redundancy-independent R-factor R_{meas} (Diederichs and Karplus 1997), which can be used to judge the precision of individual symmetry-related reflection intensities:

$$R_{meas} = \frac{\sum_{hkl} \sqrt{\frac{N}{N-1}} \sum_i \left| I_i(hkl) - \overline{I(hkl)} \right|}{\sum_{hkl} \sum_i I_i(hkl)} \tag{9}$$

R_{meas} can be used to determine the space group symmetry of a crystal or to evaluate isomorphism of two diffraction data sets. Other R-factors exist, which were regularly used to judge diffraction data, including R_{sym}, $R_{p.i.m.}$, $R_{mrgd\text{-}I}$. However, they were recently discussed to be misleading or inferior to other indicators and proposed to be subsided by more meaningful indicators based on the Pearson correlation coefficient (Karplus and Diederichs 2012, 2015):

$$CC_{1/2} = \frac{\sum_{i=1}^{n}((x_i - \bar{x})(y_i - \bar{y}))}{\sqrt{\sum_{i=1}^{n}(x_i - \bar{x})^2 \sum_{i=1}^{n}(y_i - \bar{y})^2}} \qquad CC^* = \sqrt{\frac{2CC_{1/2}}{1 + CC_{1/2}}} \tag{10) / (11}$$

For calculation of $CC_{1/2}$, the symmetry-related (redundant) reflections are randomly divided into two half data sets, separately averaged and correlated with each other. Knowing the number of observations, the significance of the data can be calculated by the student's t-test. Concluding, calculation of the $CC_{1/2}$ within individual resolution bins allows to estimate the residual information content of the reflections and to define a high-resolution limit. The CC^* assesses the accuracy of the merged reflection data, meaning the agreement of merged data with the hypothetical and unknown "true" data. Both $CC_{1/2}$ and CC^*, in contrast to other indicators, were shown to predict beneficial and adverse effects on the final model by merging of different data sets (Diederichs and Karplus 2013).

Furthermore, CC^* allows to link the diffraction data quality with the model quality by comparison with CC_{work} and CC_{free} (Karplus and Diederichs 2012). Equivalent to calculation of R_{work} and R_{free}, CC_{work} and CC_{free} are thereby calculated using the “working” and “test set” of the diffraction data. CC^* represents an upper limit for the model quality, which is limited by data quality. $CC_{work}<CC^*$ indicates a model, which insufficiently explains the reflection data. $CC_{free}>CC^*$ reveals overfitting of the data, because this would suggest the model to better explain the data than the “true” structure.

The above indicators are limited to “global” assessments of data sets or models. The real-space correlation coefficient (Jones et al. 1991), following Equ. 10, allows local comparison of the model electron density with the “observed” electron density to e.g. detect placement of single residues of the model not matching the observed electron density distribution.

Apart from the convergence of the model’s calculated diffraction data to the experimental diffraction data, model quality can be judged based on its structural properties. Root-mean-square deviations from ideal bond lengths and angles should be low (less than 0.02 Å and 4°, respectively). Peptide bonds should approximately be planar and mostly *trans* (*cis* more probable for proline). Backbone dihedral angles (ϕ and φ) should mainly fall into allowed regions of the Ramachandran plot (except for glycine) and side chain dihedral angles (χ) should match with typical rotamer conformations. The clash score, quantifying too close contacts of van der Waals radii, should be low. The (total) occupancy of each atom should ideally be 1 and uncertainty in atomic positions is given by high B-factors to interpret low electron density as disorder. Reasonable deviations from these parameters might represent “true” features of the structure and should preferably be supported by high-resolution data.

2 Materials and Methods

2.1 Materials

Reagents were mostly obtained from Carl Roth (Karlsruhe, Germany) or Sigma-Aldrich (Darmstadt, Germany). DNA oligonucleotides (primers) for cloning and plasmid DNA sequencing were ordered from Eurofins Genomics (Ebersberg, Germany). DNA-purification kits were acquired from Macherey-Nagel (Düren, Germany). Pre-packed chromatography columns for preparative protein purification were obtained from GE Healthcare (Chicago, IL, USA). Other suppliers for particular materials are given in the following chapters.

2.2 Cloning of *Bv*HSS variant expression plasmids

An expression plasmid coding for the wildtype (wt) *Bv*HSS (*Bv*HSS pETM-14) was kindly provided by Dr. Krossa (Krossa et al. 2016). The plasmid is based on the pETM-14 backbone (EMBL, Heidelberg, Germany). The wt *Bv*HSS-coding cDNA was previously introduced into the plasmid via NcoI/XhoI-restriction sites (Figure 32, p. 85). Expression of the resulting plasmid yields the wt *Bv*HSS with an *N*-terminal 6x histidine-tag followed by a human rhinovirus 3C (HRV 3C) cleavage site. For the generation of the *Bv*HSS single residue variants, site-directed mutagenesis was performed to target the respective codons in the *Bv*HSS DNA sequence. Complementary oligonucleotides were designed, which carried the corresponding mutations (Table 1).

Table 1: Primers used for the cloning of *Bv*HSS variants.
Mutated nucleotides in reference to the wt BvHSS sequence are colored red. The corresponding codon is underlined.

Name of primer	Sequence (5' → 3')	Name of primer	Sequence (5' → 3')
*Bv*HSS D94K fw	TCTCGGTCAAAACCTCATCGCT	*Bv*HSS E210A fw	CATCGCCGCGCGCGACA
*Bv*HSS D94K rv	GATGAGGTTTTGACCGAGAGGT	*Bv*HSS E210A rv	TGTCGCGCGCGGCGATGT
*Bv*HSS D94N fw	CCTCTCGGTCAATACCTCATCGCTC	*Bv*HSS E210K fw	ACATCGCCAAGCGCGACA
*Bv*HSS D94N rv	GAGCGATGAGGTATTGACCGAGAGG	BvHSS E210K rv	TCGCGCTTGGCGATGTG
*Bv*HSS V116F fw	ACACCGTGTTCGAGCCGTG	*Bv*HSS E210Q fw	ACATCGCCCAACGCGACA
*Bv*HSS V116F rv	ACGGCTCGAACACGGTGTC	*Bv*HSS E210Q rv	TCGCGTTGGGCGATGTG
*Bv*HSS E117K fw	CGTGGTCAAACCGTGGCTTG	*Bv*HSS W229A fw	AACACCGCGTCGGTCGAG
*Bv*HSS E117K rv	CCACGGTTTGACCACGGTGT	*Bv*HSS W229A rv	ACCGACGCGGTGTTGACG
*Bv*HSS E117Q fw	ACACCGTGGTCCAGCCGTGGCTT	*Bv*HSS W229E fw	TTCGTCAACACCGAATCGGTCGAG
*Bv*HSS E117Q rv	AAGCCACGGCTGGACCACGGTGT	*Bv*HSS W229E rv	CTCGACCGATTCGGTGTTGACGAA
*Bv*HSS Y123E fw	GCTTGGCTTCGAATTCGACCCCG	*Bv*HSS W229F fw	CGTCAACACCTTTTCGGTCGAGGG
*Bv*HSS Y123E rv	CGGGGTCGAATTCGAAGCCAAGC	*Bv*HSS W229F rv	CCCTCGACCGAAAAGGTGTTGACG
*Bv*HSS Y123F fw	GCTTGGCTTCTTTTTCGACCCCG	*Bv*HSS W229H fw	TCAACACCCATTCGGTCGAGGG
*Bv*HSS Y123F rv	CGGGGTCGAAAAAGAAGCCAAGC	*Bv*HSS W229H rv	TCGACCGAATGGGTGTTGACGA
*Bv*HSS Y123K fw	CTTGGCTTCAAATTCGACCCCGAC	*Bv*HSS W229K fw	GTTCGTCAACACCAAGTCGGTCGA
*Bv*HSS Y123K rv	GTCGGGGTCGAATTTGAAGCCAAG	*Bv*HSS W229K rv	TCGACCGACTTGGTGTTGACGAAC
*Bv*HSS Y123S fw	CTTGGCTTCTCATTCGACCCCGAC	*Bv*HSS W229Y fw	TCAACACCTATTCGGTCGAGGG
*Bv*HSS Y123S rv	GTCGGGGTCGAATGAGAAGCCAAG	*Bv*HSS W229Y rv	TCGACCGAATAGGTGTTGACGA
*Bv*HSS N135F fw	CGCGCTCGTTCTACGCG	T7 promoter	TAATACGACTCACTATAGGG
*Bv*HSS N135F rv	AGCGCGTAGAACGAGCGC	T7 terminator	GCTAGTTATTGCTCAGCGG

The Phusion polymerase (Thermo Fisher Scientific, Waltham, MA, USA) was used for PCR in GC-Buffer with 0.5 mM dNTPs (Thermo Fisher Scientific), 0.5 µM of each primer, 50 ng *Bv*HSS pETM-14 template and 3 % DMSO. The elongation time was 30s/kbp.
Two cloning strategies were used, restriction/ligation-free cloning and cloning using overlap-extension-PCR. For restriction/ligation-free cloning, the primer pairs carrying the desired mutations (Table 1) and the *Bv*HSS pETM-14 template DNA were used to synthesize complete, nicked plasmids containing the site-directed mutations in a single PCR. Template DNA strands were subsequently digested with DpnI (Thermo Fisher Scientific).
For cloning using overlap-extension-PCR, two initial PCRs were performed with the *Bv*HSS pETM-14 template DNA and two different primer combinations. In one PCR, the T7 promoter primer was combined with the reverse variant primer. In the other PCR, the T7 terminator primer was combined with the forward variant primer. The two resulting PCR products were purified by agarose gel electrophoresis and subsequent gel-extraction. The PCR products were subsequently utilized in combination with both T7 primers in a third overlap-extension-PCR. The third PCR product was digested with the restriction enzymes NcoI and XhoI (New England Biolabs) and ligated (T4 DNA Ligase, Thermo Fisher Scientific) with equally digested and dephosphorylated (Thermosensitive Alkaline Phosphatase (FastAP), Thermo Fisher Scientific) pETM-14-plasmid.
Following both cloning strategies, generated plasmids were transformed into *E. coli* XL1-Blue cells by heat shock for plasmid production. The correct *Bv*HSS DNA sequence was confirmed by sequencing. For protein expression, plasmids were heat shock-transformed into *E. coli* BL21(DE3) gold cells.

2.3 Cloning of *Pa*HSS expression plasmids

The amino acid sequence of *Pa*HSS (UniProtKB Q6X2Y9) was back-translated into an *E. coli* K12 codon-optimized DNA sequence by EMBOSS Backtranseq (https://www.ebi.ac.uk/Tools/st/emboss_backtranseq/). Addition of 5'-CC and TAATAACTCGAG-3' to the termini of the DNA sequence provided NcoI and XhoI restriction sites and two stop codons (Figure 33, p. 85). The synthesis of this DNA was ordered from General Biosystems, Inc. (Durham, NC, USA) and delivered as insert in a pUC57 plasmid (*Pa*HSS pUC57). For plasmid production, *Pa*HSS pUC57 was heat shock-transformed into *E. coli* XL1-Blue cells. The *Pa*HSS-coding DNA sequence was removed from the pUC57 plasmid via NcoI/XhoI-restriction and ligated with equally restricted and dephosphorylated pETM-14 plasmid, yielding *Pa*HSS pETM-14 plasmid. *Pa*HSS pETM-14 plasmid was heat shock-transformed into *E. coli* XL1-Blue cells for plasmid amplification. The correct sequence of the *Pa*HSS insert was confirmed by DNA sequencing and *Pa*HSS pETM-14 was heat shock-transformed into *E. coli* BL21(DE3) gold cells for protein expression.

2.4 Expression and purification of wt *Bv*HSS and variants

A starter culture of *E. coli* BL21(DE3) gold cells transformed with wt *Bv*HSS pETM-14 plasmid or a variant plasmid was incubated in LB medium (including 30 µg/mL kanamycin) at 37 °C in a shaking incubator overnight. On the following day, 1 L LB media (incl. 30 µg/mL kanamycin) in 5 L baffled Erlenmeyer flasks were inoculated to an absorbance at 600 nm (OD_{600}) of 0.1 and further cultivated at

37 °C and 90 rpm (orbital diameter = 25 mm) to an OD_{600} of 0.6-0.8. After induction with 1 mM isopropyl-β-D-1-thiogalactopyranoside (IPTG), cells were further incubated for 4 h at 25 °C. The cells were harvested by centrifugation (10 min, 10,000 g, 4 °C) prior to freezing in liquid nitrogen and storage at -80 °C.

Table 2: Buffers used for purification and storage of wt *Bv*HSS and variants.
DTT: dithiothreitol, PMSF: phenylmethylsulfonyl fluoride, DNase I (Thermo Fisher Scientific).

Buffer	Composition
Standard buffer	50 mM BIS-TRIS propane-HCl pH 9, 25 mM KCl, 2 mM DTT
Lysis buffer	Standard buffer incl. 25 mM imidazole, 1 mM PMSF, 1 U/mL DNase I
Wash buffer	Standard buffer incl. 25 mM imidazole
Elution buffer	Standard buffer incl. 0.5 M imidazole
Storage buffer	Standard buffer incl. 2 mM NAD^+

Before cell disruption, the pellet was thawed and resuspended 1:10 (w/v) in lysis buffer (buffer compositions listed in Table 2). Cells were disrupted by one passage through an Emulsiflex C3 homogenizer (Avestin, Mannheim, Germany) at pulses of approximately 1,200 bar. Cell debris was subsequently separated by centrifugation (45 min, 75,600 g, 10 °C). Following chromatographic purification steps were performed at an ÄKTA FPLC system (GE Healthcare), equipped with a multi-wavelength UV-Vis monitor (UV-900) for protein detection and a conductivity detector. The wt *Bv*HSS and variants were purified from the clarified cell extract via their *N*-terminal 6x histidine-tag by immobilized metal ion chromatography (IMAC). The extract was therefore loaded onto a 5 mL HisTrap HP column (agarose beads with chelated Ni^{2+} ions), which was equilibrated with 15 column volumes (CV) standard buffer beforehand. The loaded column was then washed with 10 CV standard buffer, followed by 10 CV standard buffer incl. 25 mM imidazole (wash buffer). Bound protein was eluted by increasing the concentration of imidazole in standard buffer to 0.5 M (elution buffer) in a linear gradient over 5 CV. For the *Bv*HSS variants Y123S and W229K, a single elution peak at 280 nm was detected during imidazole-gradient formation. For the wt *Bv*HSS and the other variants, an additional elution peak occurred before gradient formation in the preceding washing step with 25 mM imidazole in standard buffer. In case of two such elution fractions, the fractions were separately pooled and treated as described in the following purification steps. Protein pools were concentrated in 10 kDa Amicon Ultra-15 Centrifugal Filter Units (Merck Millipore, Darmstadt, Germany) by centrifugation (3,000 g, 4 °C). The buffer of the protein sample was exchanged for fresh standard buffer using 5 mL HiTrap Desalting columns according to the manufacturer's protocol. To remove the *N*-terminal histidine-tag, the purified protein was incubated over night at 4 °C with glutathione S-transferase (GST)-tagged HRV 3C protease in a 1:100 protein ratio (HRV3C:purified protein). The following day, the GST-tagged HRV 3C protease and the histidine-tag were removed by passage of the protein sample through connected 5 mL HisTrap HP and GSTrap HP columns in standard buffer. The final protein sample was concentrated to approx. 5 mg/mL, supplied with 2 mM NAD^+, aliquoted, frozen in liquid nitrogen and stored at -80 °C.

2.5 Expression and purification of *Pa*HSS

E. coli BL21(DE3) gold cells carrying *Pa*HSS pETM-14 plasmid were used to inoculate an LB medium starter culture (incl. 30 µg/mL kanamycin), which was then incubated at 37 °C in a shaking incubator overnight. The next day, 1 L media (incl. 30 µg/mL kanamycin) in 5 L baffled Erlenmeyer flasks were inoculated to an OD_{600} of 0.1 and further grown at 37 °C and 90 rpm (orbital diameter = 25 mm) to an OD_{600} of 0.6-0.8. After induction with 0.1 mM IPTG, cells were incubated for 20 h at 25 °C. Cells were harvested by centrifugation (10 min, 10,000 g, 4 °C), frozen in liquid nitrogen and stored at -80 °C.

Table 3: Buffers used for purification and storage of *Pa*HSS.
DTT: dithiothreitol, PMSF: phenylmethylsulfonyl fluoride, DNase I (Thermo Fisher Scientific).

Buffer	Composition
Basis buffer	50 mM TRIS-HCl pH 7.4, 25 mM KCl, 2 mM DTT
Lysis buffer	Basis buffer incl. 0.3 M NaCl, 25 mM imidazole, 2 mM NAD^+, 1 mM PMSF, 1 U/mL DNase I
IMAC wash buffer I	Basis buffer incl. 0.15 M NaCl
IMAC wash buffer II	Basis buffer incl. 25 mM imidazole
IMAC elution buffer	Basis buffer incl. 0.5 M imidazole
AEX elution buffer	Basis buffer incl. 1 M NaCl
Storage buffer	Basis buffer incl. 2 mM NAD^+

Prior cell disruption, the cell pellet was thawed and resuspended 1:10 (w/v) in lysis buffer (buffer compositions listed in Table 3). Cells were opened by one passage through an Emulsiflex C3 homogenizer at pulses of approximately 1,200 bar. After centrifugation (45 min, 75,600 g, 10 °C), the *Pa*HSS was purified from the cell extract via chromatographic purification steps at the ÄKTA FPLC system described in chapter 2.4. In a first step, the extract was loaded onto an equilibrated (15 CV basis buffer) 5 mL HisTrap HP column for binding of the protein via its *N*-terminal 6x histidine-tag. The column was then washed with 5 CV basis buffer incl. 0.15 M NaCl (IMAC wash buffer I), followed by 5 CV basis buffer incl. 25 mM imidazole (IMAC wash buffer II). Elution of bound *Pa*HSS was performed by increasing the concentration of imidazole in basis buffer to 0.5 M in a linear gradient over 20 CV (IMAC elution buffer). Eluted protein was pooled and concentrated in 10 kDa Amicon Ultra-15 Centrifugal Filter Units by centrifugation (3,000 g, 4 °C). Using 5 mL HiTrap Desalting columns, the protein was transferred into basis buffer according to the manufacturer's protocol. The sample was supplied with 2 mM NAD^+ and the *N*-terminal histidine-tag was removed by incubation of the *Pa*HSS with GST-tagged HRV 3C protease in a 1:100 protein ratio (HRV 3C:purified protein) over night at 4 °C. On the next day, both the GST-tagged HRV 3C protease and the histidine-tag were removed by passage of the protein sample through connected 5 mL HisTrap HP and GSTrap HP columns in basis buffer. The flow-through containing the *Pa*HSS was directly loaded onto two 1 mL HiTrap Q HP columns (anion-exchange chromatography (AEX)), equilibrated with basis buffer. Applying a linear gradient to 0.3 M NaCl (AEX elution buffer) over 15 CV, the *Pa*HSS eluted between ~18-23 mS/cm and was collected. The pooled protein sample was desalted and provided with fresh basis buffer using HiTrap Desalting columns. The protein was concentrated to approx. 5 mg/mL, supplied with 2 mM NAD^+, aliquoted, frozen in liquid nitrogen and stored at -80 °C.

2.6 Biophysical characterization of proteins

2.6.1 Determination of protein concentration

Protein concentrations were spectroscopically determined at 280 nm (P300 Nanophotometer, Implen, München, Germany) according to the Lambert-Beer law:

$$A_{280} = \log\frac{I_0}{I} = \varepsilon_{280} * c * d$$

Equation 12: Lambert-Beer law.

A_{280}: absorption at 280 nm, I_0: intensity of incident light (W m^2), I: intensity of transmitted light (W m^2), ε_{280}: molar extinction coefficient at 280 nm (dm^2 mol^{-1}), c: protein concentration (mol/L), d: path length (dm).

Extinction coefficients were calculated based on the amino acid sequence of the respective protein using the ProtParam online tool from Expasy (Gasteiger et al. 2005).

2.6.2 Gel electrophoresis

The molecular weight (M_W) and purity of proteins was estimated by sodium dodecyl sulfate polyacrylamide gel electrophoresis (SDS-PAGE) (Laemmli 1970). Protein samples were pretreated by mixing with reducing loading buffer (final concentration: 50 mM TRIS-HCl pH 6.8, 10 % (w/v) glycerol, 2 % (w/v) SDS, 0.05 % (w/v) bromophenol blue, 5 % (v/v) β-mercaptoethanol) and incubation at 98 °C for 5 min. Casting of gels and electrophoresis was performed using the Mini-PROTEAN system (Bio-Rad, Feldkirchen, Germany). The gels were prepared with 30 % acrylamide:bis-acrylamide (37.5:1) solution (Carl Roth) and were composed of a 5 % stacking gel (0.13 M TRIS-HCl pH 6.8, 0.1 % (w/v) SDS) and a 12 % separating gel (0.38 M TRIS-HCl pH 8.8, 0.1 % (w/v) SDS). The pretreated protein samples and a M_W marker (Pierce™ unstained protein molecular weight marker, Thermo Fisher Scientific) were loaded onto the gel and separated at constant 250 V for 35 min. The gel was subsequently fixed and stained in 20 % (v/v) ethanol, 10 % (v/v) acetic acid and 0.1 % (w/v) Coomassie brilliant blue R-250. Excess dye was removed by washing with 20 % (v/v) ethanol and 10 % (v/v) acetic acid.

2.6.3 SEC-MALS

The oligomerization state of proteins was examined by size-exclusion chromatography coupled to multi-angle light scattering (SEC-MALS). Analysis was performed on a high-performance liquid chromatography system (HPLC, Agilent 1100 series, Waldbronn, Germany). It was composed of a vacuum degasser (S 8515, Schambeck SFD GmbH, Bad Honnef, Germany), a quaternary pump (G1311A), both an autosampler (G2258) and a sample injection valve (7725i, Rheodyne LLC, Bensheim, Germany), a multi-wavelength detector (G1365B), a refractive index detector (G1362A) and a three-angle light scattering detector (miniDAWN TREOS, 658 nm laser, Wyatt Technology, Dernbach, Germany). Two different SEC columns were used for sample separation in an isocratic mobile phase. *Pa*HSS samples were separated with a Superdex 200 10/30 column (10x300 mm, 13 µm particle size, GE Healthcare) in PBS (137 mM NaCl, 2.7 mM KCl, 10 mM Na_2HPO_4, 1.8 mM KH_2PO_4, pH 7.4) at 0.5 mL/min. Samples of wt *Bv*HSS and *Bv*HSS variants were separated with a

WTC-050N5 column (4.6x300 mm, 500 Å pore size, 5 µm particle size, Wyatt Technology) protected by a corresponding WTC-050N5G guard column in PBS (pH 7.0) at 0.4 mL/min. The M_W of the analyzed samples was determined by the software Astra 5.3.4.10 (refractive index n_{water} = 1.331, $dn/dc_{protein}$ = 0.185 mL/g, second virial coefficient A_2 = 0, Model = Zimm, fit degree = 1). Conventional calibration of the columns was done with a mixture of differently sized proteins (Protein Standard Mix 15-600 kDa, Sigma-Aldrich).

2.6.4 Thermal shift assay

Thermal shift assays (TSA) were performed to evaluate the effect of various buffer conditions on the folding state and thereby stability of *Bv*HSS and *Pa*HSS. Therefore, protein was mixed with different buffer components, salts and additives in 96-well format in the presence of a fluorescent dye and subjected to a temperature gradient. Depending on the stability of the protein in the respective assay solution, the protein begins to unfold from a certain temperature on. Hydrophobic core regions are subsequently revealed and bind to the dye, thereby increasing its fluorescence. As result, unfolding of the protein can be correlated to increasing fluorescence emission, which is measured as „melting curve“. A Boltzmann function was fitted to the fluorescence data using a Microsoft Excel-based analysis tool (ftp://ftp.sgc.ox.ac.uk/pub/biophysics) to allow calculation of its inflection point. This inflection point, in the following termed “melting temperature” (T_M), was used to compare the stability of the proteins in different buffer compositions.
For the assay, *Pa*HSS still carrying the *N*-terminal histidine-tag and the “*Bv*HSS elution 1” (chapter 3.1, p. 31) without histidine-tag were used. *Pa*HSS was thereby obtained by IMAC and desalting into 50 mM TRIS-HCl (pH 7.5), 25 mM KCl, 2 mM DTT without the following anion-exchange chromatography step. The *Bv*HSS sample contained 50 mM BIS-TRIS propane-HCl (pH 9), 25 mM KCl, 2 mM DTT and 2 mM NAD^+. For *Pa*HSS, each assay solution was prepared in 20 µL aliquots containing 0.2 mg/mL protein, 5x SYPRO Orange protein gel stain (Sigma-Aldrich) and buffer components as indicated in chapter 3.3 (p. 40). *Bv*HSS assay solutions were similarly prepared but contained 10 x dye. Measurement was performed in an Applied Biosystems 7300 Real Time PCR System (Thermo Fisher Scientific) in 96-well PCR plates (half skirt flat, SARSTEDT AG &Co. KG, Nümbrecht, Germany) sealed with film (AxyGen PCR-TS CyclerSeal, Jena Bioscience GmbH, Jena, Germany). Over 75 cycles, the temperature was step-wisely increased from 21 °C to 95 °C and held for 1 min at each step. The fluorescence was measured using the TAMRA filter set at three different locations per well. The average of the three fluorescence values was plotted against the temperature to calculate the T_M.

2.6.5 HSS activity assay

To analyze the conversion of PUT to HSP by *Pa*HSS, *Bv*HSS and corresponding variants, a protocol published by Weiss *et al.* (Weiss et al. 1997) was applied. In short, PUT was added to the respective protein and the reaction was stopped after defined time intervals by precipitation of the protein. The polyamines were fluorescently labeled and quantified after separation via reversed-phase chromatography by measurement of the fluorescent signal. If not stated otherwise, the following protocol was used for the assays.

The enzymatic reaction was started by addition of 10 mM PUT (Sigma-Aldrich) in three pre-warmed reaction pools (independent triplicate measurement) containing 0.2 g/L protein in 50 mM potassium phosphate (pH 7.4) and 0.2 mM NAD^+ at 37 °C or 25 °C. After varying time spans, the reactions were stopped by transfer of 100 µL from the reaction pools into 50 µL 100 % (w/v) trichloroacetic acid. Precipitated protein was separated from the soluble polyamines by centrifugation at 18,000 g for 10 min. 1 µL supernatant was subsequently mixed with 589 µL 0.2 M sodium borate-NaOH buffer (pH 8.5). 25 µL of the neutralized samples were labeled with 10 µL 10 mM 6-aminoquinolyl-N-hydroxysuccinimidyl carbamate (Synchem UG & Co. KG, Felsberg, Germany) in dry acetonitrile. After incubation for 5 min at RT in the dark, the samples were diluted with 35 µL 0.2 M sodium borate-NaOH buffer (pH 8.5). 50 µL of the labeled samples were loaded onto a ProntoSIL HyperSorb ODS (C18) column (4.6x250 mm, 120 Å pore size, 5 µm particle size, Bischoff Chromatography, Leonberg, Germany), corresponding to injection of 202 pmol of initially added PUT. The mobile phase was a mixture of 25 mM triethylamine (pH 4.8, adjusted with acetic acid), 80 % (v/v) acetonitrile and methanol in a gradient composition described by the protocol of Weiss *et al.*. The flow rate was 1.3 mL/min at 33 °C and fluorescence was measured at λ_{ex} = 248 nm, λ_{em} = 398 nm at a photomultiplier gain of 11. Signal peaks were integrated for quantification using the ChemStation software version B.01.03 (Agilent) (Figure 15). To confirm the retention times of the respective labeled compounds and to convert peak areas to compound quantity, different amounts of PUT and HSP (Toronto Research Chemicals Inc., Ontario, Canada) were directly labeled and separated on the column to determine a standard curve (Figure 17). The mean number of HSP molecules produced per (monomeric) HSS molecule was plotted against the reaction time using GraphPad Prism version 5.00 (Figure 18). The maximal slope at steady state, yielding the k_{cat} value including its standard deviation, was derived from linear regression considering all data points (not only the mean) of at least three time points.

2.6.6 Crystallization

Crystallization of *Bv*HSS variants and *Pa*HSS was performed by the hanging drop vapor diffusion technique at 18 °C.

*Bv*HSS variants were crystallized as similarly described (Krossa et al. 2016). The hanging drop was a mixture of 1 µL protein solution (~3.3 mg/mL HSS, 33 mM BIS-TRIS propane-HCl pH 9, 17 mM KCl, 1.3 mM DTT, 1.3 mM NAD^+, 0.2 mM agmatine sulfate) and 1 µL reservoir solution (0.1 M sodium acetate pH 4.6–4.8, 150 mM ammonium acetate, 22–26% (w/v) polyethylene glycol (PEG) 10,000, 150–300 mM 3-(1-pyridino)-1-propane sulfonate), equilibrated against 0.5 mL reservoir solution. Crystals became visible after ~3 days in needle clusters. Single needles were manually isolated from the cluster, harvested and either directly frozen in liquid nitrogen (variants E117Q, PDB ID 6S6G; E210A, PDB ID 6S49; E210Q, PDB ID 6S3X) or soaked with PUT prior freezing (variants N135F, PDB ID 6S65; W229A, PDB ID 6S72; W229E, PDB ID 6SEP; W229F, PDB ID 6S4D). Soaking was done by short transfer of single crystals into a drop containing 0.2 M PUT and 2/3 reservoir solution.

To crystallize *Pa*HSS (PDB ID 6Y87), 1 µL protein solution (~3.3 mg/mL *Pa*HSS, 33 mM TRIS-HCl pH 7.4, 17 mM KCl, 1.3 mM DTT, 1.3 mM NAD^+, 0.2 mM agmatine sulfate) and 1 µL reservoir solution (0.1 M HEPES-NaOH pH 7.5, 18-23 % (w/v) poly(acrylic acid sodium salt) (average M_W ~5,100),

10 mM adenosine triphosphate (ATP)) were mixed as hanging drop and equilibrated against 0.5 mL reservoir solution. Crystals became detectable after ~1-3 days and were disintegrated by vortexing with glass beads in reservoir solution. By streak seeding, crystal debris was transferred into hanging drops of a freshly prepared crystallization setup. This second setup was similarly prepared as described above, but the poly(acrylic acid sodium salt) concentration was only increased from 18-22 % (w/v) in 24 incremental steps. Crystals became visible after one day and turned into homogeneous, trigonal prism-shaped crystals within several days in a narrow concentration range of poly(acrylic acid sodium salt). Crystals were briefly soaked with 20 % glycerol / 80 % reservoir solution before freezing in liquid nitrogen. Initial crystallization conditions were found in-house (chapter 3.5, p. 50). Further optimization was achieved by additive screenings, funded by iNEXT (funded by the Horizon 2020 program of the European Commission) and performed by the HTX crystallization facility at the EMBL Hamburg, Germany.

2.6.7 X-ray diffraction data collection

Diffraction data for structure solution were collected at 100 K at beam lines P13 and P14 (EMBL, DESY PETRA III, Hamburg, Germany). P13 was equipped with a PILATUS 6M detector, P14 with an EIGER 16M detector. Data of structures with PDB IDs 6S72, 6S6G, 6S49, 6SEP were collected at P13, data of structures with PDB IDs 6S65, 6S4D, 6S3X, 6Y87 at P14.

2.6.8 Structure determination and visualization

Indexing and integration of diffraction data was performed with the software XDS (Kabsch 2010). The following data reduction was done with the programs Pointless and SCALA of the CCP4 program suite (Potterton et al. 2003; Evans 2011). The space group was determined with Pointless. SCALA was used for scaling and merging of reflections and to assign FreeR-flags to 5 % of the data sets. Initial structure models were calculated by molecular replacement (MR) using PHENIX (Afonine et al. 2012). For *Bv*HSS variants, the wt *Bv*HSS model (PDB ID 4PLP), lacking the NAD^+ molecules and any other ligands, served as starting model. After MR, the mutated residue of each variant was accordingly exchanged in the program Coot (Emsley et al. 2010) and a refinement including cartesian simulated annealing was performed using the software PHENIX. The model was further optimized by iterative manual and automated refinement using Coot and PHENIX, respectively.

For the *Pa*HSS structure, the wt *Bv*HSS model (PDB ID 4PLP) together with the amino acid sequence of *Pa*HSS were used to calculate an initial *Pa*HSS phasing model without NAD^+ molecules or any other ligand using the standard settings of PRIMO (Hatherley et al. 2016). With the Matthew's coefficient calculator software within the CCP4 suite, six molecules of *Pa*HSS were estimated to fit in the asymmetric unit. MR was performed with PHENIX, specifying six initial *Pa*HSS phasing models per asymmetric unit as input. An iterative process of MR and manual inspection of MR solutions using Coot was performed. Correctly placed molecules, which were supported by electron density, served as improved starting model for another round of MR, while misplaced molecules were deleted from the asymmetric unit. The final MR model contained six correctly placed molecules within the asymmetric unit. After fitting of NAD^+ molecules into the active site of each molecule, a refinement including cartesian simulated annealing was performed with the software PHENIX. The model was further

improved by iterative manual and automated refinement using Coot and PHENIX, respectively.
Structural images were prepared with PyMOL (Schrödinger 2015). Omit maps were calculated with the composite omit map-tool implemented in Phenix by omitting only one specific part of the model, including cartesian simulated annealing in the refinement and allowing bulk solvent to occupy omit regions. For PUT omit maps, only the PUT molecule was omitted. For omit maps targeting the respective residue mutated in each corresponding *Bv*HSS variant, the mutated residue was omitted together with ten N- and C-terminally adjacent residues (21 residues in total).
Superimposition of structures was mostly done with PyMOL using the "super" algorithm over 5 cycles. Therefore, hydrogen atoms were neglected and only protein atoms, NAD^+ atoms and alternate locations A were considered. RMSD values were subsequently calculated with the command "rms_cur". For the generation of the structure-based sequence alignment of *Bv*HSS and *Pa*HSS, the structures of *Bv*HSS (PDB ID 4TVB, chain B) and *Pa*HSS (PDB ID 6Y87, chain A) were superimposed onto each other using UCSF Chimera 1.14 (Pettersen et al. 2004) via the "MatchMaker" tool. This tool comprised an initial sequence alignment based on the Needleman-Wunsch algorithm, the BLOSUM-62 substitution matrix and secondary structure scoring. The sequence alignment was followed by the superimposition of structures including iterative pruning of C_α atom pairs exceeding a distance of 2 Å. RMSD values were calculated for both the pruned C_α atom pairs and all superimposed C_α atom pairs. The resulting structure-based sequence alignment is depicted in Figure 28 (p. 71) with a C_α-based residue-residue distance cutoff of 5 Å. The sequence conservation is scored according to the PAM250 matrix using Clustal symbols (* = identical, : = high similarity, . = low similarity). RMSD between "complete" residues, including all identically named atoms of the aligned residues, are illustrated as bars with a cutoff of 5 Å.
For the depiction of solvent-accessible surfaces in the interior of proteins, binding pockets were filled with dummy atoms using the program Hollow 1.1 (Ho and Gruswitz 2008). Dummy atoms with a radius of 1.4 Å were placed at a grid spacing of 0.2 Å and restricted to the "interior" of the protein by applying a surface probe sphere with a radius of 4 Å. After addition of water molecules from the respective structure to the dummy atoms, the surface of this cast of dummy atoms was depicted with PyMOL.

3 Results

3.1 Protein expression and purification of wt *Bv*HSS and variants

Both wt *Bv*HSS and *Bv*HSS variants were produced and purified according to the same protocol. In brief, expression was performed in *E. coli* BL21(DE3) gold cells for 4 h at 25 °C after induction with 1 mM IPTG at an OD_{600} = 0.6-0.8. The cells were disrupted by shear force to release the protein. After removal of cell debris by centrifugation, the protein of interest was purified from the clarified cell extract by IMAC via its *N*-terminal 6x histidine-tag. Thereby, two washing buffers were passed through the column after loading, the second buffer containing 25 mM imidazole. In a linear elution gradient, the imidazole concentration was further increased to 0.5 M. The buffer of the eluted protein samples was exchanged to remove the imidazole and the *N*-terminal 6x histidine-tag was cleaved off by incubation with HRV 3C protease overnight. By passage through an IMAC column and a glutathione-functionalized column, both the histidine-tag and the GST-tagged protease were removed from the protein sample.

In the following, the results of the protein production and purification of the wt *Bv*HSS and the *Bv*HSS variant W229K are discussed. The results of the other variants (D94K, D94N, V116F, E117K, E117Q, N135F, Y123E, Y123F, Y123K, Y123S, E210A, E210Q, E210K, W229A, W229E, W229F, W229H, W229Y) were very similar regarding protein yield, purity and oligomerization state. Figure 4 depicts the UV absorbance at 280 nm during IMAC purification of the wt *Bv*HSS.

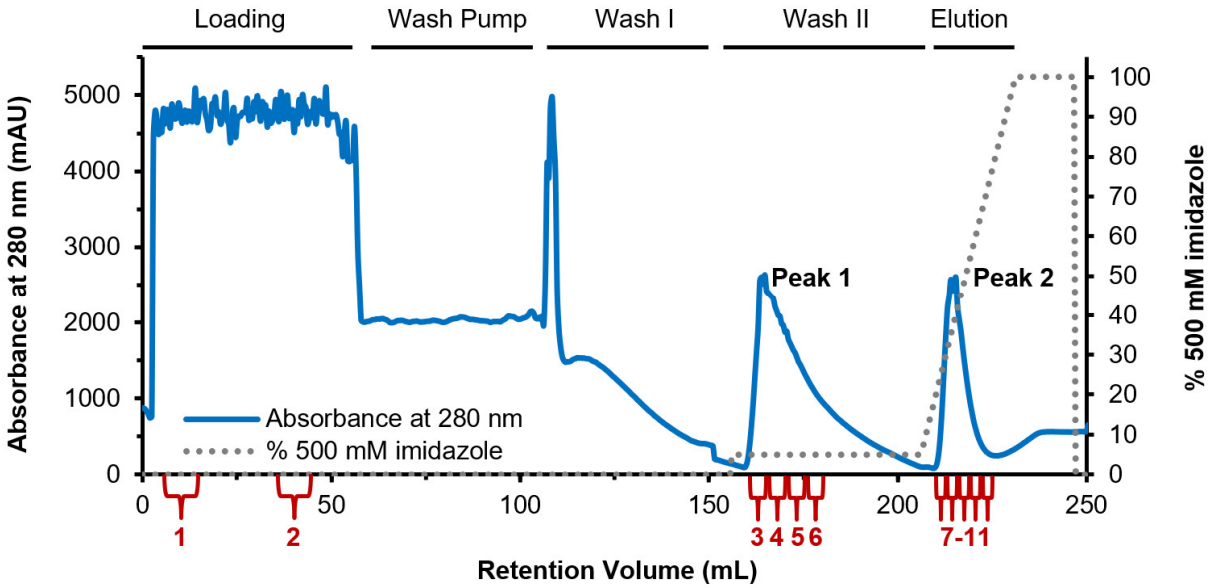

Figure 4: Chromatogram of the IMAC purification of wt *Bv*HSS.

Cell extract originating from 4 L expression medium was loaded onto a 5 mL HisTrap HP column. The loading, washing and elution steps are indicated above the chromatogram. The "Wash Pump" step flushed the loading pump and was not passed through the column. The buffer of the "Wash II" step contained 25 mM imidazole and the imidazole concentration was linearly increased during "Elution" to 0.5 M. Collected fractions, which were analyzed by SDS-PAGE (Figure 5), are indicated under the x-axis in red. The two wt Bv*HSS elution peaks (termed "Peak 1" and "Peak 2") were separately pooled, further processed and analyzed by SDS-PAGE (Figure 7) and SEC-MALS (Figure 8).*

Figure 5 shows the corresponding reductive SDS-PAGE analysis of individual samples, which were collected throughout the purification process. The first SDS-PAGE sample contained integer cells, which were harvested after protein production (P, pellet). A distinct band at ~50 kDa is visible, matching the M_W of a *Bv*HSS monomer, among lots of other protein bands.

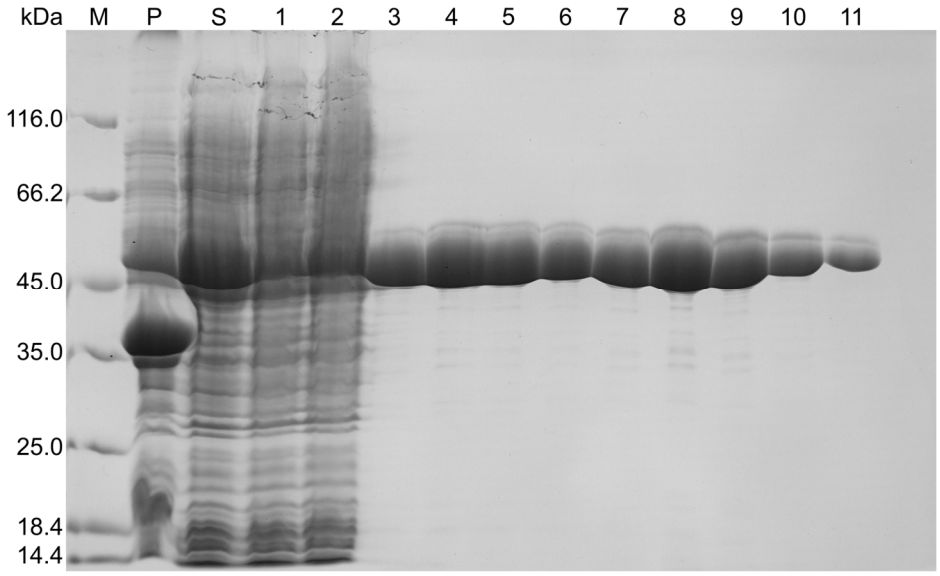

Figure 5: SDS-PAGE analysis of the wt *Bv*HSS purification.

Protein samples (indicated in Figure 4) were incubated in reductive loading buffer at 98 °C and separated in a 12 % separating gel. M = M_W marker, P = whole cell sample (pellet), S = cell extract without debris (supernatant), 1-11: collected fractions from the wt Bv*HSS IMAC purification as indicated in Figure 4.*

The second sample was the clarified cell extract without cell debris (S, supernatant). In this sample, the protein band at ~50 kDa is the most prominent one and stronger than in the cell sample. The soluble wt *Bv*HSS accordingly represented the most abundant protein in the cell extract, suggesting an effective protein expression. Regarding the chromatogram of the IMAC purification, a high absorbance was detected during loading of the *E. coli* cell extract, which nearly declined to zero after the first washing step. In the SDS-PAGE samples of the column flow-through (1 and 2) from the beginning and ending of this loading step, the ~50 kDa band was distinctly weaker compared to the extract sample. The majority of wt *Bv*HSS was therefore bound to the IMAC column without considerable oversaturation of the column at the end of the loading phase. The second washing step with buffer containing 25 mM imidazole was originally applied to wash weakly binding contaminants from the column. Interestingly, a large elution peak (Peak 1) occurred during this second washing step, followed by another peak (Peak 2) within the elution gradient. Both peaks are distinctly baseline-separated from each other in the chromatogram, suggesting two protein species with different binding affinities to the IMAC column. Fractions belonging to Peak 1 (3-6) and Peak 2 (7-11) showed the same strong 50 kDa-protein band in the SDS-PAGE with faint low-molecular-weight (LMW) impurities (~35-45 kDa), which were only detectable in highly concentrated samples. These two elution species were similarly found for all *Bv*HSS variants but not for variants Y123S and W229K. For the latter variants, no increase of absorbance was measured during the second washing step, containing 25 mM imidazole. Instead, only one “strongly binding” protein species was eluted within the imidazole gradient, consistently termed “Peak 2”.

The IMAC purification chromatogram of the *Bv*HSS variant W229K with its single elution peak is representatively shown in Figure 6.

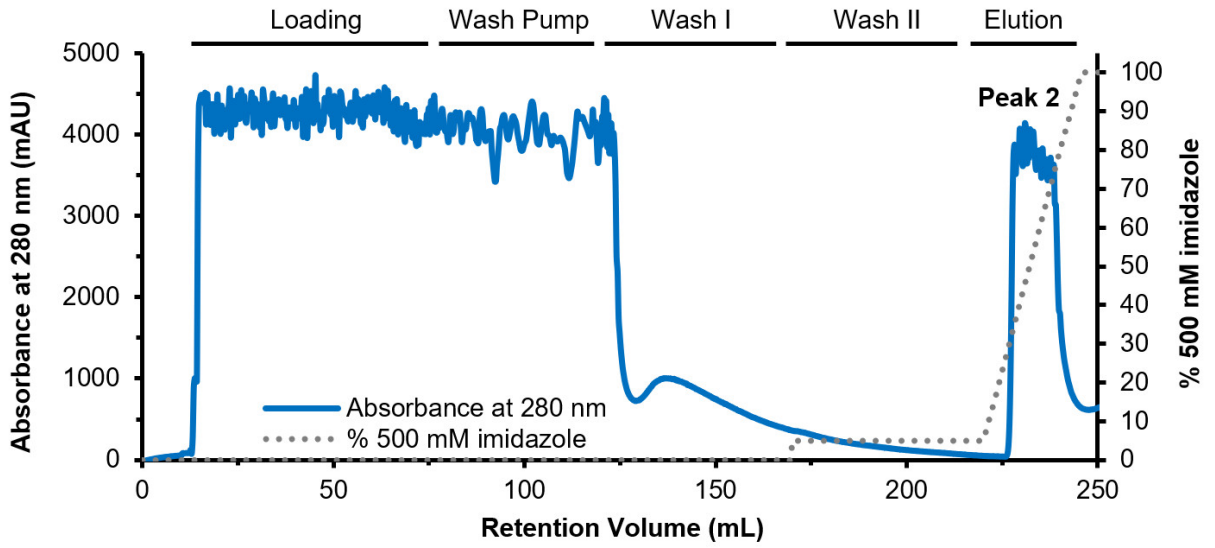

Figure 6: Chromatogram of the IMAC purification of the *Bv*HSS variant W229K.

Cell extract originating from 4 L expression medium was loaded onto a 5 mL HisTrap HP column. The loading, washing and elution steps are indicated above the chromatogram. The "Wash Pump" step flushed the loading pump and was not passed through the column. The buffer of the "Wash II"-step contained 25 mM imidazole and the imidazole concentration was linearly increased during "Elution" to 0.5 M. The Bv*HSS W229K elution peak (termed "Peak 2") was pooled, further processed and analyzed by SEC-MALS (Figure 8).*

The reason for this variant-dependent elution behavior from the IMAC column remains elusive. One explanation could be the different accessibility of the *N*-terminal 6x histidine-tag, influencing the affinity to the IMAC column. In this context, different oligomerization states cannot be the cause for this effect. All variants were purified as dimers as confirmed by SEC-MALS (Figure 8) and the *N*-terminus is located at the opposite site of the dimer interface as confirmed by the determined X-ray structures.

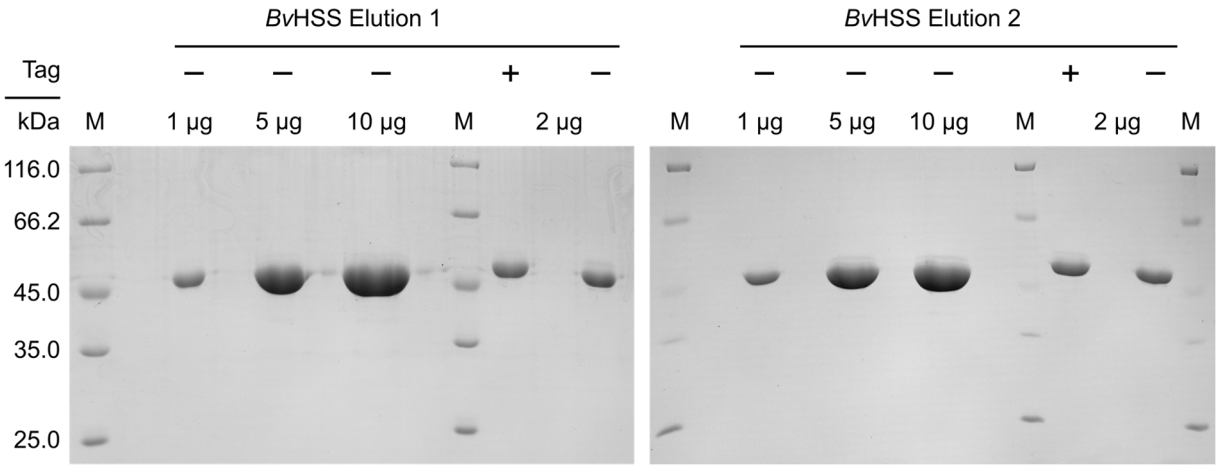

Figure 7: SDS-PAGE analysis of purified wt *Bv*HSS.

*Protein samples were incubated in reductive loading buffer at 98 °C and separated in a 12 % separating gel. "*Bv*HSS Elution 1" and "*Bv*HSS Elution 2" samples correspond to the IMAC elution peaks as labeled in Figure 4. The amount of loaded sample in µg and the presence (+) or absence (-) of the* N*-terminal histidine-tag are indicated. M = M_W marker.*

The final protein pools of the wt *Bv*HSS after chromatographic removal of both the cleaved tag and the protease were additionally analyzed by reductive SDS-PAGE (Figure 7). Loading up to 10 µg of protein, a sharp protein band at ~50 kDa without impurities is visible for both wt *Bv*HSS elution pools. Furthermore, protein samples separated before and after incubation with HRV 3C protease show a shift in the SDS-PAGE, confirming the successful removal of the histidine-tag.

Regarding yield and purity of wt *Bv*HSS production, 4 L expression medium provided a 7 g wet cell pellet after harvesting. The elution "Peak 1" amounted to ~13 mg and the elution "Peak 2" to ~7 mg. The total yield of the wt *Bv*HSS expression was therefore 20 mg or 5 mg/L_{medium}. Although the purification mainly consisted of a single IMAC step, a high purity of the protein could be confirmed by SDS-PAGE.

The wt *Bv*HSS and the variants were further analyzed by SEC-MALS to determine the oligomerization state (Figure 8). The oligomerization state can roughly be estimated by SEC in reference to a protein standard mix and was more accurately confirmed by coupled MALS analysis. M_W values according to SEC-MALS are given in Table 4.

Table 4: Molecular weights of proteins according to SEC-MALS analysis.

The first column indicates the sample, which was analyzed by SEC-MALS. The second column states the individual proteins or oligomerization states. The third column lists the actual M_W of the proteins, the fourth lists the SEC-MALS results. A partially monomeric state of Bv*HSS W229K could be presumed based on the SEC analysis but was not further confirmed. SEC-MALS data of the Protein Standard Mix is comparably poor due to the small amount of loaded protein (175 µg in total).*

Sample	Protein / Oligomer	M_W (kDa)	M_W (kDa, SEC-MALS)
Protein Standard Mix	thyroglobulin	~670	758
	γ-globulins	~150	142
	albumin	~44.3	52
	ribonuclease A type I-A	~13.7	22
wt *Bv*HSS	dimer	106	98
***Bv*HSS W229K**	dimer	106	90
	monomer	53	62 (potential)

Both wt *Bv*HSS elution samples were equally eluted after ~3.5 mL from the SEC column as single, sharp absorbance peak. The peak at ~4.6 mL was caused by NAD^+, which was supplied in the storage buffer of the protein. Referencing the retention volume to the protein mix, the wt *Bv*HSS eluted between peak II (γ-globulins, ~150 kDa) and peak III (albumin, ~44.3 kDa), roughly matching the M_W of a *Bv*HSS dimer (~106 kDa).

In line with the correlation to the protein standard mix, SEC-MALS analysis resulted in a M_W value of 98 kDa for both wt *Bv*HSS elution pools. The wt *Bv*HSS has previously been shown to form a dimer in solution (Krossa et al. 2016) as consistently shown in this work. SEC-MALS analysis of variant W229K is also depicted in Figure 8. The elution behavior from the column and the calculated M_W (90 kDa) are similar to the wt *Bv*HSS, confirming a dimeric state. Still, a small peak shoulder could be detected at higher retention volume (~3.9 mL) with a calculated M_W of 62 kDa. This could be caused by a small proportion of monomeric protein or by protein impurities.

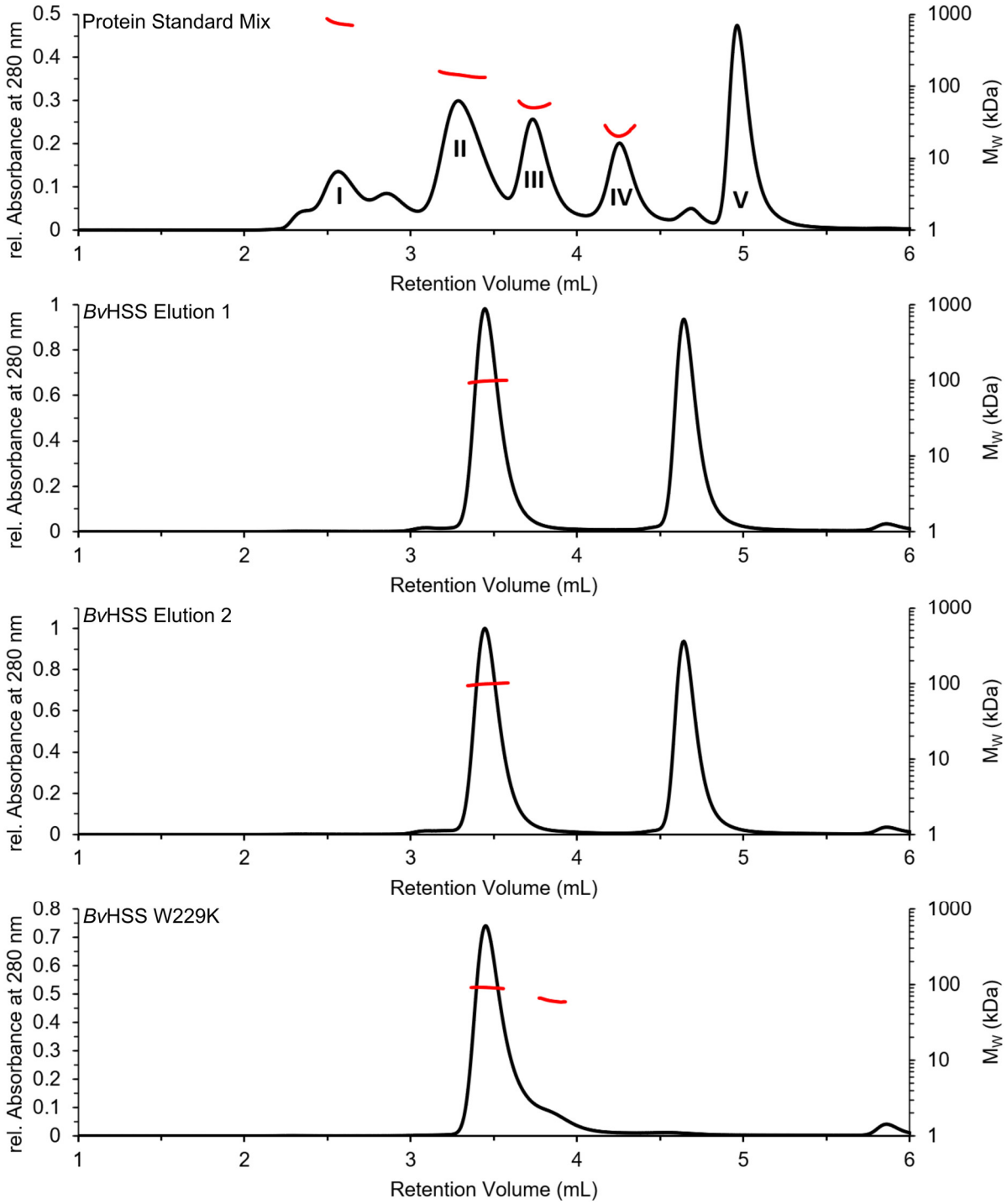

Figure 8: SEC-MALS analysis of wt *Bv*HSS and the *Bv*HSS variant W229K.

Proteins were separated on a WTC-050N5 column (4.6x300 mm, 500 Å pore size, 5 µm particle size, Wyatt Technology) in PBS (pH 7) at 0.4 mL/min. Chromatography was followed by measurement of the absorbance at 280 nm (black graphs), the light scattering at three angles and the change of refractive index. M_W values (depicted in red) were calculated as described in chapter 2.6.3 (p. 25). The injection volume was 50 µL. 175 µg of total protein was injected in case of the protein standard mix, individual components are labeled with Roman numerals (I: bovine thyroglobulin (~670 kDa), II: bovine blood γ-globulins (~150 kDa), III: chicken egg albumin (~44.3 kDa), IV: bovine pancreas ribonuclease A type I-A (~13.7 kDa), V: p-aminobenzoic acid). 50 µg of Bv*HSS samples were injected. The peak at ~4.6 mL in the* Bv*HSS samples resulted from supplied NAD^+. rel. = relative.*

However, MALS data of such overlapping peaks may not be accurate because the larger oligomers/molecules can be assumed to be present in higher quantities in the unseparated peak and because the scattering contribution of these larger molecules dominates the scattering contribution of smaller ones. SDS-PAGE-analysis did not help discriminating potential impurities from potential monomers either. Both dimers and monomers of *Bv*HSS W229K in addition to protein impurities around ~50 kDa would lie in roughly the same band in a reductive SDS-PAGE. Nevertheless, the predominant proportion of the purified *Bv*HSS W229K sample was present as dimer. The other *Bv*HSS variants in this work were similarly observed to (predominantly) form dimers according to SEC-MALS. Taken together, purified protein samples of wt *Bv*HSS and variants were highly pure according to SDS-PAGE and mostly consisted of dimers as confirmed by SEC-MALS.

3.2 Protein expression and purification of *Pa*HSS

*Pa*HSS was produced in *E. coli* BL21(DE3) gold cells in 4 L expression medium at 25 °C for 20 h. Induction was performed with 0.1 mM IPTG at an OD_{600} = 0.6-0.8. The cells (6 g wet pellet per L_{medium}) were disintegrated by shear force and debris was removed from the soluble fraction by centrifugation. The cell extract was loaded onto an IMAC column to purify the *Pa*HSS via its *N*-terminal 6x histidine-tag from the cell extract. After two washing steps, the *Pa*HSS was eluted from the column by linearly raising the imidazole concentration up to 0.5 M. Imidazole was removed from the sample by gel-filtration and the histidine-tag was removed by incubation with HRV 3C protease overnight. Both the detached histidine-tag and the GST-tagged protease were cleared from the sample by passage through a combination of an IMAC and a glutathione-functionalized column. The *Pa*HSS was further purified by binding to an anion-exchange chromatography (AEX) column and subsequent elution in a linear salt gradient. A final desalting step was performed to remove the salt from the purified *Pa*HSS sample. The yield of finally purified protein was ~8 mg/L_{medium}.

The different chromatography steps were monitored by measurement of the UV absorbance at 280 nm and by SDS-PAGE analysis of the collected chromatography fractions. Apart from the IMAC fractions, a sample of integer harvested cells (P, pellet) and a sample of the clarified cell extract without cell debris (S, supernatant) were separated in an SDS-PAGE gel (Figure 9). The most prominent protein band in the pellet sample was detected at ~50 kDa and would match the M_W of a *Pa*HSS monomer. This band is also distinctly visible in the cell extract sample, albeit far weaker. Taken together, a significant amount of *Pa*HSS is probably not recovered in the soluble cell extract but remains in the cell debris. Aggregation of the protein and formation of inclusion bodies could be an explanation. Early expression experiments with shorter expression times consistently showed stronger ~50 kDa bands in the pellet sample, but not in the cell extract sample (data not shown). Subsequent IMAC chromatography of these samples did not yield significant elution of *Pa*HSS. Only by increasing the expression time to 20 h, soluble *Pa*HSS could be recovered from the cell extract. The *Pa*HSS therefore seems to form inclusion bodies at the beginning of the expression experiment and remains soluble or refolds from the inclusion bodies only at later stages of the expression. A slower expression of *Pa*HSS due to nutrient deprivation after longer incubation time might support the native folding of the *Pa*HSS, explaining the late occurrence of soluble monomers. The IMAC purification chromatogram is visualized in Figure 10 and evaluated via SDS-PAGE analysis of collected fractions (Figure 9).

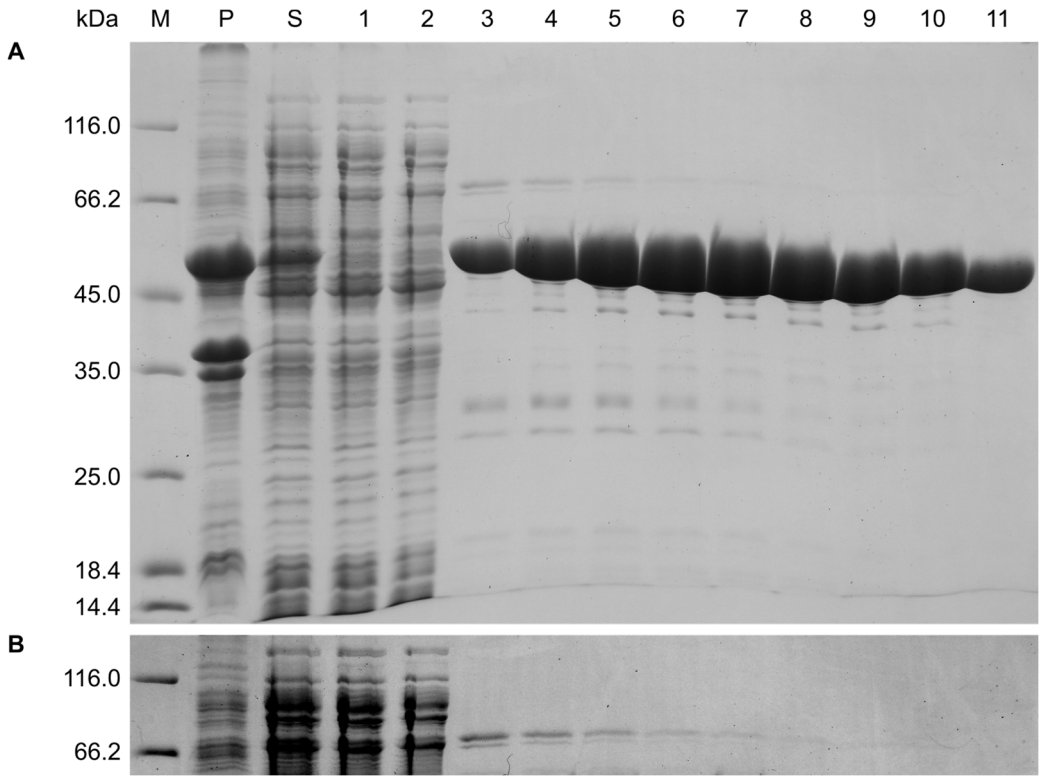

Figure 9: SDS-PAGE analysis of the IMAC purification of *Pa*HSS.

Protein samples were incubated in reductive loading buffer at 98 °C and separated in a 12 % separating gel. M = M_W marker, P = whole cell sample (pellet), S = cell extract without debris (supernatant), 1-11: collected fractions from the Pa*HSS IMAC purification as indicated in Figure 10.* ***(B)*** *shows the oversaturated lower section of (A) to highlight the HMW impurities of samples 3-~7.*

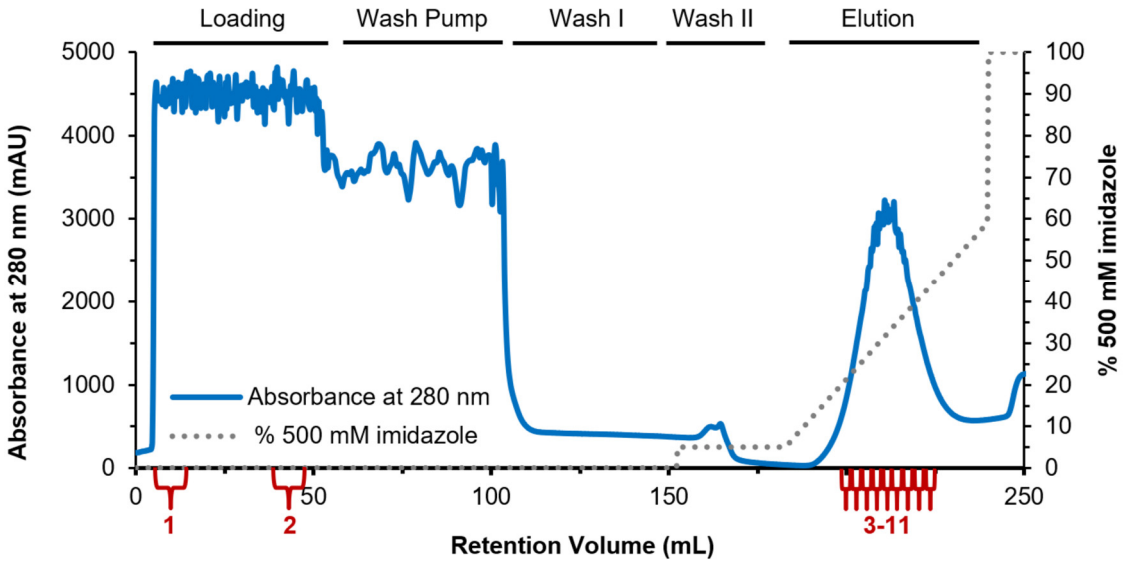

Figure 10: Chromatogram of the IMAC purification of *Pa*HSS.

Cell extract originating from 4 L expression medium was loaded onto a 5 mL HisTrap HP column. The loading, washing and elution steps are indicated above the chromatogram. The "Wash Pump" step flushed the loading pump and was not passed through the column. The buffer of the "Wash II" step contained 25 mM imidazole and the imidazole concentration was linearly increased during "Elution" to 0.5 M. Collected fractions, which were analyzed by SDS-PAGE (Figure 9), are indicated under the x-axis in red.

The cell extract was passed though the IMAC column, resulting in a high absorbance of unbound compounds. Collected fractions from the beginning (1) and ending (2) of the loading step did not show the prominent SDS-PAGE protein band at ~50 kDa. This suggests an efficient binding of *Pa*HSS to the column and would preclude breakthrough of *Pa*HSS due to oversaturation of the column. The first washing step was applied to wash the cell extract from the column, which significantly decreased the absorbance of the flow-through. 25 mM imidazole were supplied in the second washing step to release weakly binding impurities from the column. A tiny absorbance-peak followed by complete decline of the absorbance was consequently measured. High imidazole concentrations were observed to cause turbid *Pa*HSS elution fractions in previous purification experiments, suggesting aggregation of *Pa*HSS (data not shown). Therefore, the imidazole concentration was particularly slowly decreased during elution (5 mM imidazole/mL) to elute the *Pa*HSS at as low imidazole concentration as possible. A large absorbance peak at ~150 mM imidazole was detected in this final elution step. Close inspection of several elution fractions by SDS-PAGE analysis revealed strong ~50 kDa bands for all fractions (3-11). Although the eluted protein was very pure, small amounts of high-molecular-weight (HMW, ~66 kDa) and LMW impurities (~30-45 kDa) were visible in the gel. Especially the amount of HMW impurities was largest in early elution-fractions (3-7, Figure 9B).

After removal of the histidine-tag overnight, these impurities within the IMAC elution fractions were further reduced by AEX (Figure 11).

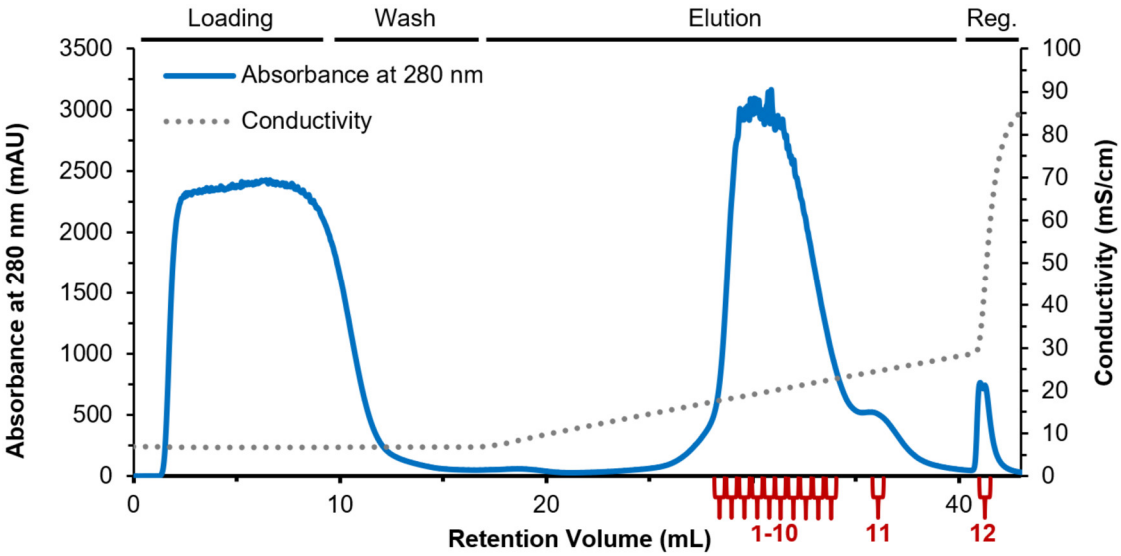

Figure 11: Chromatogram of the AEX purification of *Pa*HSS.

Eluted protein from the IMAC purification (Figure 10) was loaded onto two 1 mL HiTrap Q HP columns. The loading, washing, elution and regeneration steps are indicated above the chromatogram. The NaCl concentration was linearly increased during elution to 0.3 M and to 1 M for regeneration. Collected fractions, which were analyzed by SDS-PAGE (Figure 12), are indicated under the x-axis in red. The pool including fractions 1-10 was additionally analyzed by SEC-MALS (Figure 13).

A high absorbance at 280 nm was detected during loading of the IMAC elution pool onto the AEX column and almost completely decreased to zero during washing. The absorbance of these fractions was far higher at 260 nm than at 280 nm and did not show protein bands in SDS-PAGE analysis (data not shown). This absorbance was caused by the flow-through of NAD^+, which was supplied to the protein sample prior removal of the histidine-tag. For short- or long-term storage of *Pa*HSS, NAD^+ was

always added to increase protein stability as confirmed by TSA (chapter 3.3, p. 40). For elution of the bound *Pa*HSS protein, the NaCl concentration was linearly increased by ~10 mM NaCl/mL. A large absorbance peak was thereby detected between ~18-23 mS/cm (~28-34 mL retention volume, fractions 1-10), followed by a small peak shoulder at ~24.5 mS/cm (36 mL, fraction 11) and a small peak during regeneration at high salt concentration (fraction 12). Several elution fractions were collected to validate the purity of the protein samples by SDS-PAGE analysis in comparison to the initial AEX load pool (Figure 12).

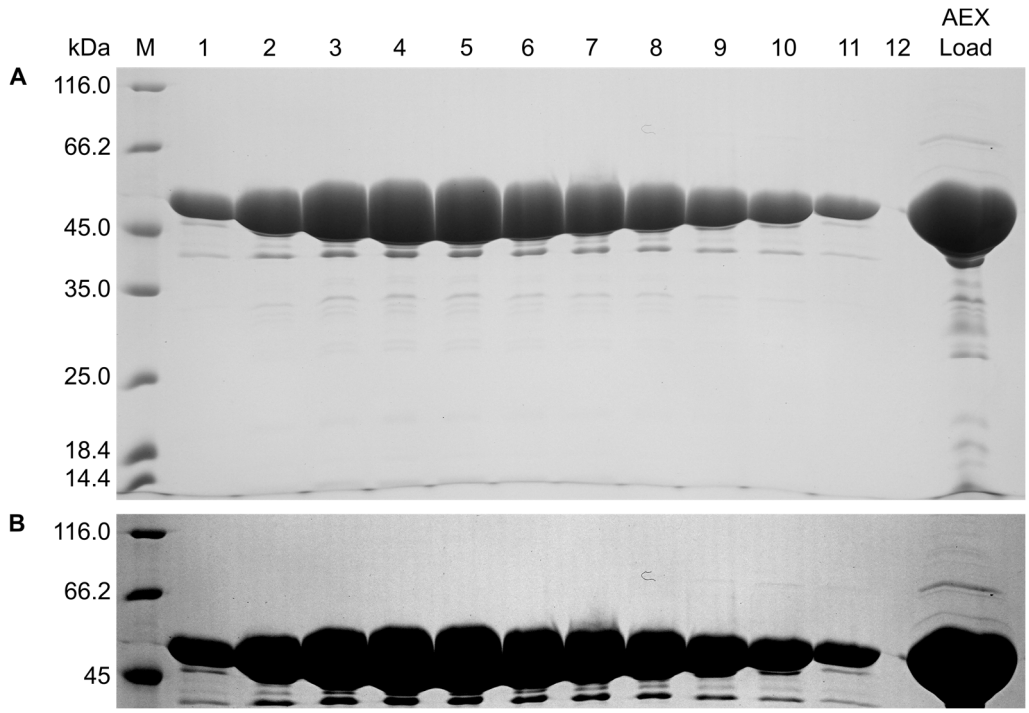

Figure 12: SDS-PAGE analysis of the AEX purification of *Pa*HSS.

Protein samples were incubated in reductive loading buffer at 98 °C and separated in a 12 % separating gel. The lower part shows a section of the gel, which was oversaturated to highlight the HMW impurities of the AEX Load. M = M_W marker, 1-12: collected fractions from the Pa*HSS AEX purification as indicated in Figure 11, AEX Load: initial loading pool of the AEX purification.* ***(B)*** *shows the oversaturated lower section of (A) to highlight the HMW impurities of the AEX Load.*

In all elution fractions but fraction 12 (regeneration), a prominent *Pa*HSS band at ~50 kDa is visible. The elution fraction 12 apparently did not contain any protein but another absorbing compound. The AEX load pool contained the highest amount of protein and therefore shows the strongest *Pa*HSS band in the gel. It also shows comparably weak LMW and HMW impurities, the latter highlighted in Figure 12B. Since the amount of loaded protein is not the same for the separated samples, comparison regarding purity is not clear. It can nevertheless be estimated, that both HMW and LMW impurities are decreased in the AEX elution fractions compared to the initial AEX load pool. As result, few LMW impurities (~40 kDa and ~30 kDa) and no HMW impurities remain detectable in the AEX elution fractions. Concluding, the *Pa*HSS could be purified to a high degree and the AEX step served as final “polishing” step. AEX fractions 1-10 (neglecting fraction 11) were pooled and further processed to provide the finally purified *Pa*HSS sample.

The oligomerization state of this final sample was determined by SEC in reference to a protein standard mix and by coupled MALS analysis (Figure 13).

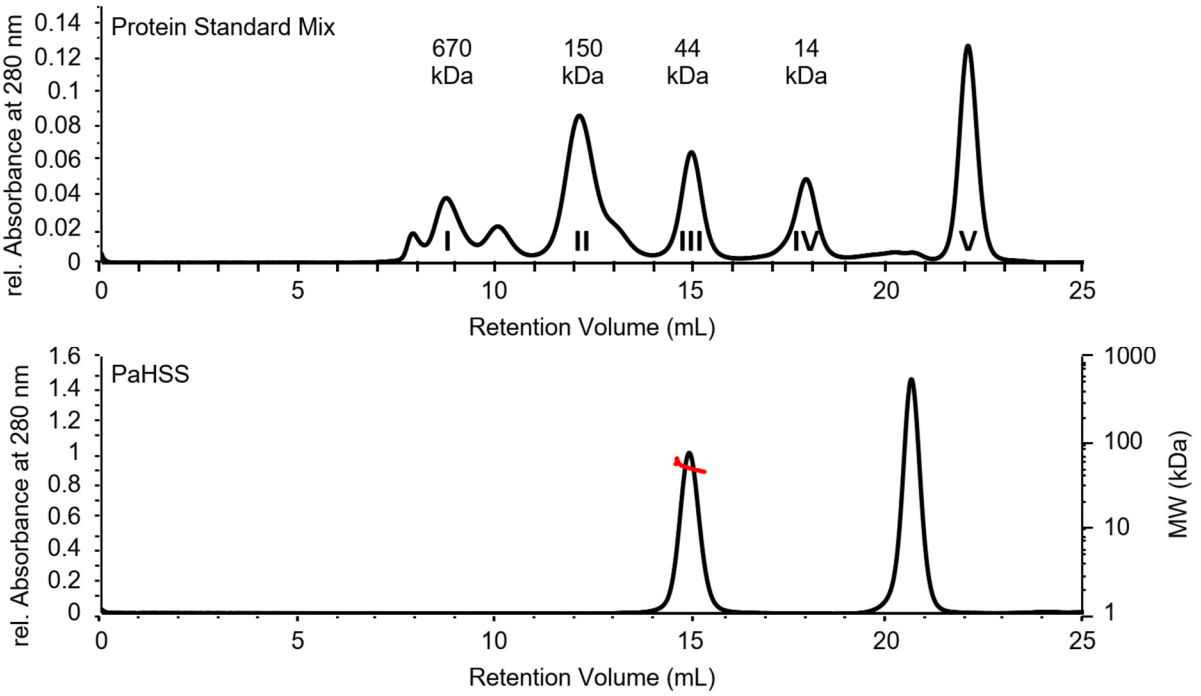

Figure 13: SEC-MALS analysis of *Pa*HSS.

Proteins were separated on a Superdex 200 10/30 column (10x300 mm, 13 µm particle size, GE Healthcare) in PBS (pH 7.4) at 0.5 mL/min. Chromatography was followed by measurement of the absorbance at 280 nm (black graphs), the light scattering at three angles and the change of refractive index. M_W values (depicted in red) were calculated as described in chapter 2.6.3 (p. 25). The injection volume was 100 µL. 50 µg of total protein was injected in case of the protein standard mix, individual components are labeled with Roman numerals (I: bovine thyroglobulin (~670 kDa), II: bovine blood γ-globulins (~150 kDa), III: chicken egg albumin (~44.3 kDa), IV: bovine pancreas ribonuclease A type I-A (~13.7 kDa), V: p-aminobenzoic acid). 100 µg of Pa*HSS sample were injected and a M_W of ~52 kDa was calculated according to the MALS analysis. The peak at ~20.5 mL of the* Pa*HSS sample resulted from supplied NAD⁺. rel. = relative.*

The *Pa*HSS sample gave a single protein absorbance peak at 280 nm after ~15 mL retention volume in the SEC analysis. The peak at ~20.5 mL was caused by the supplied NAD^+ within the protein sample. Comparing the retention volume to the protein standard mix, the *Pa*HSS was eluted at a slightly smaller retention volume than the albumin (III, ~44 kDa). This roughly matches the M_W of a *Pa*HSS monomer (~52 kDa) and was further confirmed by the MALS analysis, giving an accurate M_W of 52 kDa. Concluding, the *Pa*HSS was purified as monomeric protein with high purity.

3.3 Thermal shift assay

Thermal shift assays (TSAs) were performed to find optimal buffer conditions for the purification and storage of the *Pa*HSS. Therefore, *Pa*HSS in different buffer/additive solutions was submitted to a temperature gradient in the presence of a fluorescent dye. In such experiments, proteins unfold from a certain temperature on, exposing hydrophobic core regions. These hydrophobic regions are bound by the dye, which causes an increase of the dye's fluorescence emission. This fluorescence was measured and plotted against the temperature as melting curve. The inflection point of this curve

represents the so-called melting temperature (T_M). Higher T_Ms in certain buffer conditions indicate a higher stability of the protein. The actual increase of fluorescence was not evaluated in the following as it might be influenced by quenching effects of added compounds. For some assay solutions, a high fluorescence was already measured at the start of the temperature gradient without further increase at higher temperatures. These results were interpreted as immediate unfolding of the protein in the assay solution. In such cases, T_Ms are not given in the following tables.

Figure 14 shows TSA curves of *Bv*HSS and *Pa*HSS in their optimal buffers with stabilizing additives.

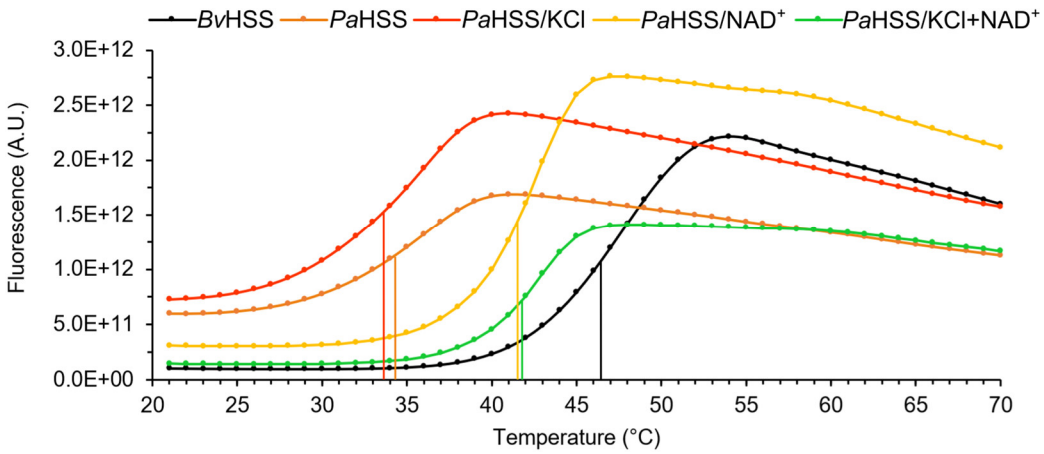

Figure 14: Thermal shift assays of *Pa*HSS and *Bv*HSS.

Melting curves of Bv*HSS and* Pa*HSS under different buffer conditions. The inflection point of each curve is marked by vertical lines, indicating the T_M. 0.2 mg/mL* Bv*HSS (black) were tested in 50 mM BIS-TRIS propane-HCl (pH 9), 25 mM KCl, 76 µM NAD^+ (transferred from added protein sample) and 10x dye. 0.2 mg/mL* Pa*HSS were tested in 0.1 M TRIS-HCl (pH 7.5), 2.5 mM KCl (transferred from added protein sample), 5x dye and additives as indicated above the chromatogram (orange: no additives; red: 25 mM KCl; yellow: 2 mM NAD^+; green: 25 mM KCl, 2 mM NAD^+).*

The curve of *Bv*HSS (black) was measured in 50 mM BIS-TRIS propane-HCl (pH 9), 25 mM KCl, 76 µM NAD^+. The presence of 76 µM NAD^+ was caused by the original *Bv*HSS sample used in this experiment, which contained 2 mM NAD^+. *Bv*HSS exhibited a T_M of ~46 °C in this assay solution, which was the highest in this study. However, the quantitative effect of NAD^+ on the T_M of *Bv*HSS was not systematically evaluated in this thesis. For the *Pa*HSS, a lower T_M (~34 °C) was determined in 0.1 M TRIS-HCl (pH 7.5) both in the absence (orange curve) and presence of additional 25 mM KCl (red curve). However, the original *Pa*HSS protein sample already contained 25 mM KCl, which caused the presence of 2.5 mM KCl in the assay samples. Concluding, an effect of KCl on the T_M cannot be completely ruled out. Addition of 2 mM NAD^+ in the presence (green curve) and absence (yellow curve) of additional 25 mM KCl significantly increased the T_M to ~42 °C. This effect suggests a stabilizing effect of NAD^+ on *Pa*HSS. NAD^+ was therefore principally added to *Pa*HSS samples prior storage.

The effect of pH and salt concentration on the stability of *Pa*HSS was also evaluated (Table 5). Between pH 6.5 and pH 8.5, interpretable melting curves could be measured. While the highest T_Ms were determined between pH 7 and 8 (~34-35 °C), T_Ms at pH 6.5 and 8.5 were reduced (~29-33 °C). At pH <6.5 and >8.5, no increase of fluorescence was detected, hinting at immediate unfolding of the protein. This pH dependency of the *Pa*HSS was in clear contrast to the far more pH tolerant (and in

general more stable) *Bv*HSS.

Table 5: Salt- and pH-dependent melting temperatures of *Pa*HSS.

0.2 mg/mL Pa*HSS were tested in 0.1 M respective buffer (as indicated for each cell in* ***(A)****), 5 mM TRIS-HCl (pH 7.5) and 2.5 mM KCl (both transferred from added protein sample), 0 to 0.5 M NaCl (as indicated in the left column for each row) and 5x dye.* T_M*s are given in °C in* ***(B)****. Empty cells result from melting curves without increase of fluorescence, suggesting immediate unfolding of the protein in the respective assay solution. Adjustment of the pH was performed with the corresponding acids (acetic acid and citric acid) or NaOH (for MES, HEPES, Bicine and CHES).*

A

No Salt	NaAc pH 4	NaAc pH 4.5	Citrate pH 5	Citrate pH 5.5	MES pH 6	MES pH 6.5	HEPES pH 7	HEPES pH 7.5	Bicine pH 8	Bicine pH 8.5	CHES pH 9	CHES pH 9.5
0.1 M NaCl	NaAc pH 4	NaAc pH 4.5	Citrate pH 5	Citrate pH 5.5	MES pH 6	MES pH 6.5	HEPES pH 7	HEPES pH 7.5	Bicine pH 8	Bicine pH 8.5	CHES pH 9	CHES pH 9.5
0.2 M NaCl	NaAc pH 4	NaAc pH 4.5	Citrate pH 5	Citrate pH 5.5	MES pH 6	MES pH 6.5	HEPES pH 7	HEPES pH 7.5	Bicine pH 8	Bicine pH 8.5	CHES pH 9	CHES pH 9.5
0.5 M NaCl	NaAc pH 4	NaAc pH 4.5	Citrate pH 5	Citrate pH 5.5	MES pH 6	MES pH 6.5	HEPES pH 7	HEPES pH 7.5	Bicine pH 8	Bicine pH 8.5	CHES pH 9	CHES pH 9.5

B

No Salt	-	-	-	-	-	29	34	35	35	33	-	-
0.1 M NaCl	-	-	-	-	-	31	34	35	33	31	-	-
0.2 M NaCl	-	-	-	-	-	29	34	35	34	31	-	-
0.5 M NaCl	-	-	-	-	-	33	35	35	35	31	-	-

The absence or presence of NaCl (0-0.5 M) did not influence the T_Ms of *Pa*HSS. Thus, the salt content did neither exert a stabilizing nor a destabilizing effect on the *Pa*HSS. Other tested buffers (not shown) with similar T_Ms between ~33-35 °C were sodium phosphate (pH 7 and 7.5), BES-NaOH (pH 7 and 7.5), MOPS-NaOH (pH 7 and 7.5), PIPES-NaOH (pH 7 and 7.5), TES-NaOH (pH 7, 7.5 and 8), HEPES-NaOH (pH 8), TRIS-HCl (pH 7.5 and 8), Tricine-NaOH (pH 7.5 and 8) and TAPS-NaOH (pH 8). Providing a neutral to slightly basic pH, the buffer compound itself therefore had no effect on the stability of the *Pa*HSS. With these results and economic reasons in mind, *Pa*HSS was purified and stored at neutral pH 7.5 using TRIS-HCl buffer.

In another TSA, an additive screen was performed to find additional stabilizing compounds for the *Pa*HSS (Table 6). This screen can also be helpful for the optimization of crystallization solutions, since stabilizing compounds might cause a higher rigidity of the protein structure, allowing formation of highly ordered protein crystals. However, the pH of most of the additive solutions was not defined. Each assay sample only contained 5 mM TRIS-HCl (pH 7.5) and 2.5 mM KCl, originating from the added *Pa*HSS sample. Due to the low buffer capacity of the assay sample, certain additives could significantly shift the pH above or below the neutral region. Regarding the instability of the *Pa*HSS beyond neutral pH values, destabilizing effects of certain additive solutions might be caused by a potential pH shift and not by the additive itself.

A selection of additives causing the most significant T_M shifts are discussed in the following. To determine a reference T_M without supplemented additives, the protein was mixed with distilled water

(A1, Table 6, T_M ~35 °C). The buffer capacity provided by the original *Pa*HSS sample should be enough to maintain a neutral pH in this assay sample, giving a similar T_M as determined in Figure 14 (orange curve).

Table 6: Additive-dependent melting temperatures of *Pa*HSS.

0.2 mg/mL Pa*HSS were tested in the buffers/additives (as indicated for each cell of* ***(A)****), 5 mM TRIS-HCl (pH 7.5) and 2.5 mM KCl (both transferred from added protein sample) as well as 5x dye. T_Ms are given in °C in* ***(B)****. The cells were colored according to the respective T_M. Empty cells (red in (B)) result from melting curves without increase of fluorescence, suggesting immediate unfolding of the protein in the respective assay solution. Buffer A: 50 mM TRIS-HCl (pH 7.5), 25 mM KCl.*

A

	1	2	3	4	5	6	7	8	9	10	11	12
A	H_2O	2 mM NAD^+ Buffer A	2 mM NAD^+ 0.5 M Imidazole Buffer A	2 mM ATP 5 mM $MgCl_2$	0.15 M GuHCl	0.5 M GuHCl	0.1 M Urea	0.5 M Urea	1 M Urea	2 M Urea	4 M Urea	6 M Urea
B	0.5 M TMAO	1 mM TCEP	0.1 M Trimethyl-amine-HCl	0.1 M CAD	0.1 M PUT	1 mM SPD -HCl	0.1 M AGM	0.1 M DAP	0.1 M Diamino-heptane	5 % PEG 400	5 % PEG 1000	5 % PEG 4000
C	50 mM Gln	10 mM Pro	25 mM His	50 mM Lys	50 mM Gly	50 mM Arg	25 mM Glu	10 mM Betaine	5 mM Folic acid	1 mM Octyl-β-glycoside	0.1 M Sucrose	0.1 M Glucose
D	0.1 M Sorbitol	0.1 M Maltose	2 % Xylitol	15 % Ethanol	5 % Methanol	10 % 2-propanol	1 % Glycerin	5 % Glycerin	10 % Glycerin	20 % Glycerin	3 % Ethylene glycol	3 % DMSO
E	10 % MPD	5 mM EDTA	10 mM DTT	0.1 M NaBr	0.1 M NaI	0.1 M NaF	0.1 M KI	1 mM $MnCl_2$	1 mM $FeCl_3$	0.1 M NaCl	0.1 M NH_4Cl	10 mM $MgCl_2$
F	0.1 M KCl	0.1 M LiCl	10 mM $CaCl_2$	1 mM $ZnCl_2$	0.1 M K_2SO_4	0.1 M $MgSO_4$	0.1 M Na_2SO_4	0.1 M NH_4SO_4	0.1 M $CaAc_2$	0.1 M $(NH_4)_2CO_3$	0.1 M $KHCO_3$	0.1 M KAc
G	0.1 M $NaNO_3$	0.1 M $NaHCO_3$	0.1 M NaAc	0.1 M $Na_2C_3H_2O_4$	0.1 M $Na_3C_6H_5O_7$							

B

	1	2	3	4	5	6	7	8	9	10	11	12
A	35	42	29	44	29	-	34	33	30	-	-	35
B	38	-	33	37	38	36	38	34	-	-	34	32
C	33	33	-	28	33	33	-	-	34	33	33	34
D	34	35	35	-	32	-	34	36	36	38	34	33
E	-	-	33	33	34	35	32	33	-	35	35	34
F	35	34	34	35	35	33	35	36	32	30	35	35
G	33	35	35	35	34							

The optimized buffer conditions (A2: 50 mM TRIS-HCl (pH 7.5), 25 mM KCl, 2 mM NAD^+) yielded a T_M of 42 °C, as equally determined in Figure 14 (green curve). Addition of 0.5 M imidazole to this buffer, which corresponds to the IMAC elution buffer, showed a significant decrease of T_M to 29 °C (A3). Since the pH of this buffer was adjusted to 7.5, the destabilizing effect was caused by the imidazole and not by a pH shift. This result was in line with previous observations, in which higher imidazole concentrations as occurring during IMAC purifications resulted in turbid protein elution pools. As discussed in chapter 3.2 (p. 36), the imidazole concentration was therefore slowly increased during IMAC purifications to elute the *Pa*HSS with as little imidazole as possible. Interestingly, addition of

2 mM ATP (with 5 mM $MgCl_2$, A4) gave the highest T_M in this screen. It should be mentioned that the melting curve showed a relatively little increase of fluorescence over a broad temperature region (not shown). Determination of the T_M therefore remains doubtful. Still, ATP seemed to have a distinctly stabilizing effect on the *Pa*HSS and was consistently found to improve crystallization as discussed in chapter 3.5 (p. 50). A slightly stabilizing influence could be perceived for the main substrate PUT (0.1 M, 38 °C, B5), the diamine CAD (0.1 M, 37 °C, B4) and for AGM (0.1 M, 38 °C, B7), the latter being used as crystallization additive for both *Bv*HSS and *Pa*HSS. While 0.1 M DAP did not seem to change the T_M (34 °C, B8), mixing with 0.1 M diaminoheptane (B9) gave an uninterpretable melting curve which hints at denaturation of the protein. Furthermore, a moderate increase of T_M (38 °C, D10) was determined at a glycerol concentration of at least 20 % (v/v). Of note, 20 % (v/v) glycerol with 80 % reservoir solution was accordingly utilized as cryo-protectant for *Pa*HSS crystals, while addition of PEG 400 or ethylene glycol disrupted diffraction of frozen *Pa*HSS crystals.
In conclusion, the optimized buffer composition for the *Pa*HSS regarding pH (pH 7.5) and addition of NAD^+ was chosen based on the TSA results. Additional additives with stabilizing effects according to the TSA were also found to improve crystallization or cryo-protection (ATP, AGM, glycerol).

3.4 Activity assays

Several *Bv*HSS variants were produced to evaluate the role of certain residues within the reaction mechanism as proposed by Krossa *et al.*. These single residue variants were compared regarding their efficacy to convert PUT into HSP. For the activity assay, protein was incubated with PUT for varying time spans before precipitation and removal of the protein. The amines were subsequently coupled to a fluorescent dye for detection. Separation of the coupled amines on a reversed-phase column allowed quantification of both PUT and HSP via fluorescence detection. This approach allowed quantitative comparison of the catalytic activities of *Pa*HSS, wt *Bv*HSS and *Bv*HSS variants at a single enzyme-saturating PUT concentration (10 mM) under equal assay conditions. However, the enzyme characteristics may not be described according to the Michaelis-Menten equation, because this would require measurement of the catalytic activity at different substrate concentrations (Michaelis et al. 2011).
Figure 15 exemplarily shows the chromatograms of two assay samples using wt *Bv*HSS at 37 °C and stopped after 1 min and 30 min, as described in chapter 2.6.5 (p. 26). Identification of the peaks, as labeled in Figure 15, was achieved by separate injection of fluorescently labeled PUT (~29 min retention time), HSP (~36.5 min retention time) and dye (~7 min and ~25 min retention time). The origin of the peak at ~33 min retention time, which exhibited absorbance at 260 nm in contrast to any other peak, remains unclear.

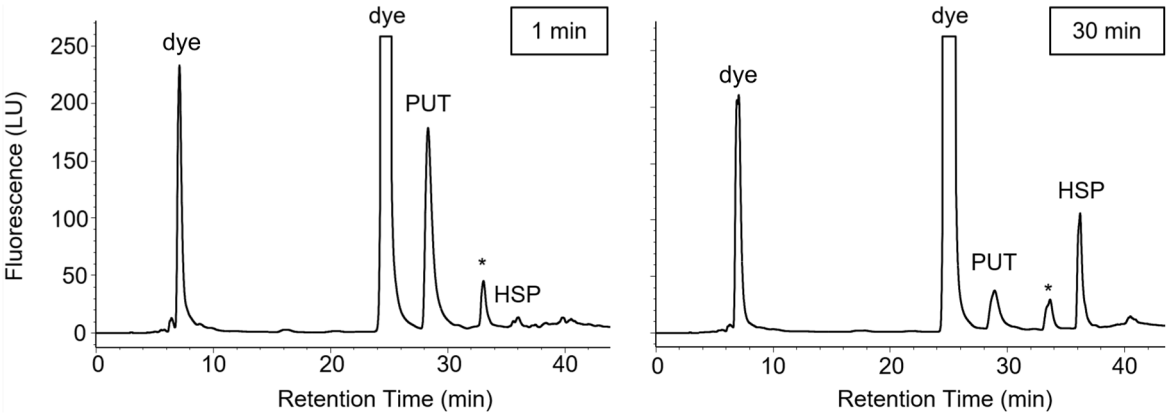

Figure 15: Activity assay measurements of wt *Bv*HSS.

The assay samples were prepared as described in chapter 2.6.5 (p. 26). Wt Bv*HSS was incubated with 10 mM PUT at 37 °C and precipitated after 1 min or 30 min. Amines were coupled with 6-aminoquinolyl-N-hydroxysuccinimidyl carbamate, separated on a C18-column and detected via fluorescence (λ_{ex} = 248 nm, λ_{em} = 398 nm). The identities of the peaks were assigned by individual injection of the respective compounds. The origin of the peak at ~33 min remains unclear.*

Both PUT and HSP peaks were baseline-separated from neighboring peaks and could be quantified by integration. The peak area of PUT clearly decreased from 1 min incubation time to 30 min incubation time, while the peak area of HSP increased. This was caused by constant conversion of PUT to HSP by the wt *Bv*HSS over time. To evaluate the conversion more accurately, the same assay was performed using three reaction pools (independent triple measurement), from which samples were drawn in shorter time intervals. The three values for both the PUT and the HSP peak areas were averaged and plotted against the incubation time (Figure 16).

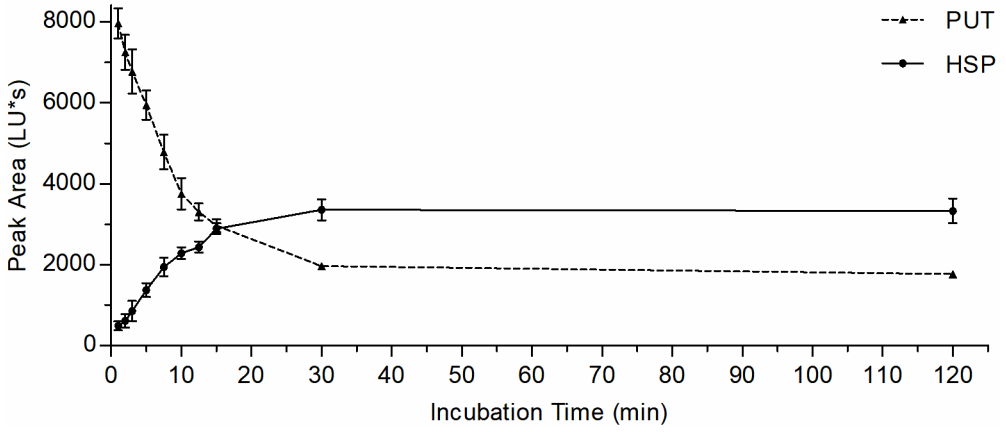

Figure 16: Conversion of PUT to HSP by wt *Bv*HSS over time.

Assay samples were prepared in independent triplicates as described in chapter 2.6.5 (p. 26). Wt Bv*HSS was incubated with 10 mM PUT at 37 °C and precipitated after varying time intervals. Amines were coupled with 6-aminoquinolyl-N-hydroxysuccinimidyl carbamate, separated on a C18-column and detected via fluorescence (λ_{ex} = 248 nm, λ_{em} = 398 nm) as exemplarily depicted in Figure 15. The peak areas of PUT and HSP were averaged and plotted against the incubation time, depicted as dots and connected by lines with two sample standard deviations (equation 13) shown as error bars.*

The sample standard deviation was calculated according to equation 13.

$$s_x = \sqrt{\frac{\sum_{i=1}^{n}(x_i - \bar{x})^2}{n-1}}$$

Equation 13: Calculation of the sample standard deviation.

Plotting of the PUT peak area shows a decreasing hyperbolic curve with a constant slope from 1-10 min incubation time, followed by a decreasing slope between 10 and 30 min and finally a constant PUT peak area from 30 min to 120 min (equilibrium state). The HSP curve is rather sigmoidal with a short lag phase at the start of the reaction (1-2 min), followed by a region showing maximal and relatively constant slope (steady state, 3-7.5 min), a region with decreasing slope (10-30 min) and the equilibrium state (>30 min) with constant peak area of HSP (and PUT). PUT was obviously not completely converted into HSP, which was similarly observed for the *Pa*HSS and active *Bv*HSS variants (not shown). This equilibrium state could be explained by a constant concentration of product and substrate maintained by forward and backward reactions catalyzed by the HSS. SPD as sole substrate was reported to be converted into HSP, PUT and DAP (chapter 1.3, p. 3). This would require catalytic separation of the triamine SPD into one diamine and one aminoaldehyde before formation of HSP. A similar reaction could be possible for HSP, entailing production of an HSP molecule via consumption of a “former” HSP molecule together with a PUT molecule. Although this process might be relatively inefficient, an increasing HSP concentration might compete with the few PUT molecules at the active site and prevent quantitative conversion of two PUT molecules into one HSP molecule.
It should be mentioned, that the absolute peak areas of PUT and HSP may not be compared for quantification due to different fluorescent quantum yields of labeled PAs (Weiss et al. 1997). To quantify the actual production of HSP, increasing amounts of labeled HSP were injected as triple measurements and a standard curve was fitted by linear regression to the peak areas (Figure 17). This standard curve allowed to correlate the HSP peak areas to the actual amounts of HSP.

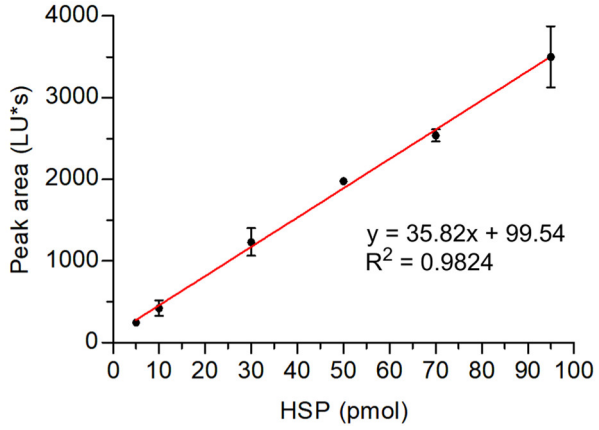

Figure 17: HSP standard curve.

Standard samples of HSP were prepared in triplicates, coupled to 6-aminoquinolyl-N-hydroxysuccinimidyl carbamate, separated on a C18-column as described in chapter 2.6.5 (p. 26) and detected via fluorescence (λ_{ex} = 248 nm, λ_{em} = 398 nm). The HSP peak areas were averaged and plotted against the injected HSP amount, depicted as dots with two sample standard deviations (equation 13) shown as error bars. The linear regression (red line) was used to correlate HSP peak areas to amounts in Figure 18.

Figure 18 depicts the progression curves of the production of HSP by wt and variant enzymes. For simplicity, only the amount of produced HSP is plotted. The catalytic optimum of the wt *Bv*HSS was reported to be at pH 8.8-9 and to increase with the reaction temperature up to 45 °C (Ober et al. 1996). However, activity assays were performed at neutral pH and at 37 °C or 25 °C in this thesis to (I) reflect physiological reaction conditions, (II) mind the instability of the *Pa*HSS at basic pH and elevated temperature (chapter 3.3, p. 40) and (III) facilitate timely manual sample handling and determination of time-resolved reaction curves by decreasing the reaction rate. Most activity assays were performed at 37 °C, only the activities of wt *Bv*HSS and *Pa*HSS were compared at 25 °C.

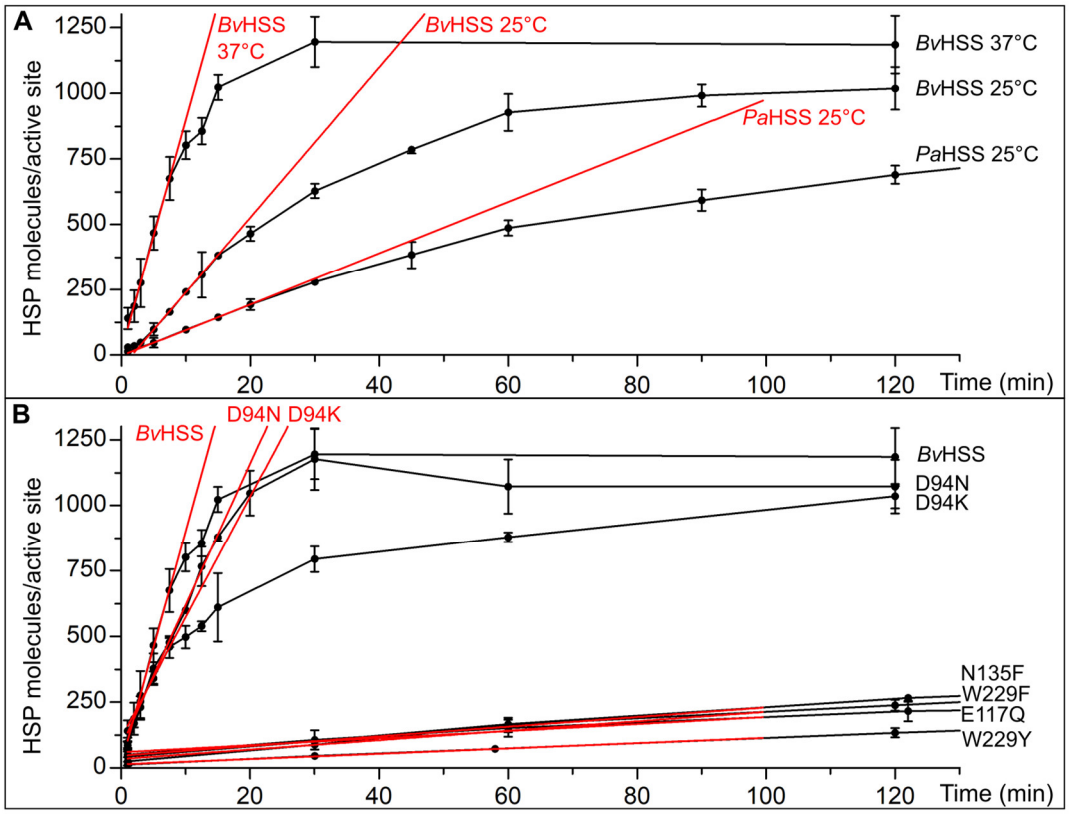

Figure 18: Production of HSP by *Pa*HSS, wt *Bv*HSS and *Bv*HSS variants over time.

*Assay samples were prepared as independent triplicates as described in chapter 2.6.5 (p. 26). Enzymes were incubated with 10 mM PUT at 37 °C or 25 °C (as indicated in **(A)**, 37 °C for **(B)**) and precipitated after varying time intervals. Amines were coupled with 6-aminoquinolyl-N-hydroxysuccinimidyl carbamate, separated on a C18-column and detected via fluorescence (λ_{ex} = 248 nm, λ_{em} = 398 nm) as exemplarily depicted in Figure 15. The peak areas of HSP were averaged and correlated to amounts using the standard curve in Figure 17. The amount of HSP molecules per monomeric enzyme (active site) was plotted against the incubation time, depicted as dots. Dots were connected by black lines for visual convenience. Two sample standard deviations (equation 13) of each triplicate measurement are shown as error bars. Linear regressions (red lines) were calculated at steady state of the curves considering at least three time points. The slopes of these tangents gave the k_{cat} values given in Table 7.*

The progression curves of the wt enzymes exhibit a sigmoidal shape (Figure 18A). The curve of the wt *Bv*HSS at 37 °C in Figure 18A is the same as already discussed in Figure 16 and exhibits the steepest slope. The curves of both wt *Bv*HSS and *Pa*HSS at 25 °C show distinctly smaller slopes at the beginning of the reaction (~3-15 min). Concluding, the wt *Bv*HSS produced HSP the fastest at 37 °C

and significantly slower at 25 °C. The slowest HSP production was achieved by *Pa*HSS at 25 °C, being slower than the wt *Bv*HSS at the same condition. In addition, the amount of HSP at the equilibrium phase was either changed depending on the reaction rate or it took far longer to reach the equilibrium. While wt *Bv*HSS at 37 °C reached ~95 pmol HSP at equilibrium after ~30 min, it only reached ~77 pmol at 25 °C after 2 h. The *Pa*HSS merely reached ~66 pmol after 5 h (not shown).
To facilitate the comparison of *Pa*HSS, *Bv*HSS and *Bv*HSS variants, tangents (red in Figure 18) were fitted to the HSP curves at steady state by linear regression to quantify the slope of the curves and thereby the turnover number k_{cat} (Table 7). Both the initial lag phase and the later transition to the equilibrium state were thereby ignored for tangent fitting. Depending on the activity of each protein, the steady state region of the respective curves differed in length and position regarding the incubation time. However, at least three time points (containing nine data points) were considered for fitting of the tangent.

Table 7: Comparison of k_{cat} values of *Pa*HSS, wt *Bv*HSS and variants.
The activity assay was performed at the indicated temperature (37 °C or 25 °C) and interpreted as described in Figure 18. For each listed protein, an HSP progression curve based on triple measurements was plotted. Linear regression at steady state of each curve gave the k_{cat}. The same was done for the Bv*HSS variants E117K, E210A, E210K, E210Q, W229A, W229E, W229H, W229K. These variants were inactive, not showing any production of HSP within 5 h. The* Bv*HSS variants V116F, Y123E, Y123F, Y123S and Y123K were determined to be "active" by simple qualitative tests (see text).*

Protein	T (°C)	k_{cat} (s^{-1})
*Bv*HSS wt	37	1.474 ± 0.226
*Bv*HSS D94N	37	0.897 ± 0.057
*Bv*HSS D94K	37	0.765 ± 0.080
*Bv*HSS N135F	37	0.031 ± 0.002
*Bv*HSS W229F	37	0.030 ± 0.002
*Bv*HSS E117Q	37	0.022 ± 0.004
*Bv*HSS W229Y	37	0.017 ± 0.001
*Bv*HSS wt	25	0.478 ± 0.038
*Pa*HSS wt	25	0.163 ± 0.017

The wt *Bv*HSS exhibited the highest k_{cat} of ~1.47 s^{-1} at 37 °C, which was decreased at 25 °C to roughly a third (~0.48 s^{-1}). The *Pa*HSS with a k_{cat} of ~0.16 s^{-1} only reached a third of the wt *Bv*HSS activity at 25 °C. In similar assays (50 mM KH_2PO_4 pH 8.5, 0.2 mM NAD^+, 1 mM PUT, 37 °C), the activity of the wt *Bv*HSS was previously reported to reach specific activities of 22 nkat/mg (Böttcher et al. 1994) and 83 nkat/mg (Tholl et al. 1996), corresponding to k_{cat} values of 1.2 s^{-1} and 4.4 s^{-1}, respectively. The reason for the difference between these activities remains elusive, but the wt *Bv*HSS activity determined in this thesis lies in the same range. In addition, the previously published activities were measured at an elevated pH (8.5), which corresponds to the catalytic optimum of the *Bv*HSS. Preliminary activity assays for the wt *Bv*HSS were also conducted at pH 9 in this thesis and an increase of the activity by a factor of roughly 4-5 could be estimated (data not shown). This would match the larger V_{max} reported by Tholl *et al.*. In the following, the activities of the *Bv*HSS variants are

compared to the wt *Bv*HSS (100 % activity) to evaluate the influence of the respective residues on the reaction mechanism. The crystal structures of several variants could additionally be solved and are discussed in chapter 3.6 (p. 53). The negatively charged residues D94 and E117 were proposed to build an “ionic slide”, which attracts and leads positively charged educts into the active site. While residue D94 is located at the entrance to the active site, residue E117 lies deeper in the “tunnel”. Neutralization of the negative charge (D94N and E117Q) and introduction of positively charged residues (D94K and E117K) were performed to disturb the “ionic slide”. The *Bv*HSS variants D94N (~0.9 s^{-1}) and D94K (~0.77 s^{-1}) both showed a reduced but still relatively high activity compared to wt *Bv*HSS (~60 and 50 %). The influence of the residue D94 therefore seemed to be moderate as even introduction of a repulsive positive charge retained ~50 % of the native activity. The activity of variant E117Q (PDB ID 6S6G) was drastically reduced to ~1.5 % (k_{cat} = 0.022 s^{-1}) of the native activity. The variant E117K was completely inactive as production of HSP could not be detected within 5 h (not shown). This was not necessarily caused by introduction of the positive charge but could result from steric repulsion by the lysine residue (structure not available). Still, a far more important contribution to the “ionic slide” seems to be provided by the residue E117.

The variants N135F (PDB ID 6S65) and V116F were designed to sterically obstruct the side pocket of the active site. The activity of variant N135F was significantly reduced to ~2 % (0.031 s^{-1}) compared to the activity of wt *Bv*HSS. The impact of this mutation on the active site and the side pocket are discussed below based on the crystal structure. The activity of the variant V116F was only examined with a qualitative activity test, in which 0.5 mg/mL of the variant were incubated with 2 mM PUT in BIS-TRIS propane-HCl (pH 9), 25 mM KCl and 0.2 mM NAD^+ for 5 min. Under these conditions, the wt *Bv*HSS reaches the equilibrium state characterized by the stable amounts of PUT and HSP within 5 min. The same equilibrium within 5 min was confirmed for the variant V116F. Although the variant was therefore proven to be active, quantitative comparison to the wt activity would need a time-resolved reaction curve. However, the crystal structure of the variant V116F could not be determined due to poor crystal diffraction. The activity of variant V116F was consequently not further examined.

The residue E210 coordinates to the “inner” amino groups of PUT and HSP at the “inner amino site”. All variants tested in this work (E210A (PDB ID 6S49), E210Q (PDB ID 6S3X) and E210K) were inactive (not shown), not showing any production of HSP within 5 h. Concluding, the presence of the negative side chain at the “inner amino site” seems to be mandatory for the activity of the *Bv*HSS.

Another focus was laid on the residue Y123 in the “track-and-trace” loop. This loop was proposed to potentially regulate the entrance to the active site assisted by residue Y123, but the significance of its role remained unclear. Four different variants (Y123E, Y123F, Y123S, Y123K) were designed to evaluate this question. In qualitative activity tests, prepared as described above for variant V116F, the reactions were stopped after 60 min. For all variants, an equilibrium was reached with maximal conversion of PUT to HSP. Although the efficacy of these variants cannot be estimated with these tests, all of them were undoubtedly active. Inspecting the electron density distribution of the Y123 variants, parts of the “track-and-trace” loops and especially residue number 123 were not unambiguously defined for any of the variants. Not being able to draw conclusions from the crystal structures nor detecting severe effects of the mutations on the activities in qualitative tests, the variants were not further examined.

The residue W229 was most closely inspected as it was suggested to play a central role in the reaction mechanism. Throughout the conversion of PUT to HSP, the aromatic side chain of the tryptophan was proposed to stabilize cationic reaction components and/or transition states via cation-π interaction. The variants W229F (PDB ID 6S4D) and W229Y both showed a drastically reduced activity of ~2 % (0.03 s^{-1}) and 1 % (0.017 s^{-1}), respectively. This finding is in line with previous quantum mechanical studies, which relate the strength of cation-π interactions to the electrostatic potential surfaces of the aromatic ring systems and quantitatively compare corresponding interaction energies (Mecozzi et al. 1996a; Reddy and Sastry 2005). According to these calculations, an indole ring has a more negative electrostatic potential than benzene and phenol rings (both having similar electrostatic potentials) and thus provides higher cation-π interaction energies. The remaining W229 variants (W229A (PDB ID 6S72), W229E (PDB ID 6SEP), W229H, W229K) were determined to be completely inactive in this thesis (not shown). Although the variant W229H provides a π-system in the histidine side chain, it seems to be too low to maintain any activity of the enzyme. This is also supported by quantum mechanical studies, disqualifying the imidazole ring for significant cation-π interactions (Mecozzi et al. 1996a; Reddy and Sastry 2005). The variant W229E was designed to provide a negative charge which might stabilize positive intermediates/transition states by ionic interaction instead of cation-π interaction. However, this substitution could not compensate for an aromatic ring system, albeit steric issues are also possible. Taken together, these findings support the role of W229 as cation-π interaction partner.

3.5 Crystallization

Crystallization of *Bv*HSS variants was performed as previously described (Krossa et al. 2016). Successful crystallization as needle clusters and collection of X-ray diffraction data was achieved for the *Bv*HSS variants D94K, D94N, V116F, E117Q, Y123E, Y123F, Y123K, Y123S, N135F, E210A, E210Q, W229A, W229E and W229F. Crystals of the variants D94K, D94N and V116F thereby diffracted too poorly for structure determination. Formation of crystals could not be observed for the variants E117K, E210K, W229H, W229K and W229Y.

The optimal crystallization conditions for the *Pa*HSS were found by consecutive screening steps. The composition of the protein solution, which was mixed with the respective reservoir solutions to provide the hanging drop, was always the same as given in chapter 2.6.6 (p. 27). It always contained 0.2 M agmatine sulfate (0.1 M in the final hanging drop), which generally increased crystal size.
Initial crystallization screens in 96-well format (PEG/Ion screen, Hampton Research) were prepared both with the *Pa*HSS still containing the *N*-terminal histidine-tag (*Pa*HSS_NHis, no AEX purification step) and with the *Pa*HSS lacking the histidine-tag (*Pa*HSS_wo_NHis, AEX-purified). In this screen, crystals were obtained for both proteins using reservoir solutions containing 0.2 M lithium citrate and 20 % (w/v) PEG 3,350 (tube 45). Reproduction in 24-well format gave inhomogeneous and partly split spear-like crystals (Figure 19A/C). Streak-seeding of crushed crystals in similar conditions improved crystal homogeneity (Figure 19B/D), but X-ray diffraction at the synchrotron was limited to ~8 Å for *Pa*HSS_wo_NHis and ~5 Å for *Pa*HSS_NHis. Using the same reservoir solution, a pH-screening was performed. Crystals were grown between pH 9-6, albeit without visible improvement of crystal

appearance. Also, PEG 3,350 could be exchanged for other PEGs with slight adjustment of the respective PEG concentrations. *Pa*HSS_NHis could be crystallized with PEG 6,000, 5,000, 4,000, 3,000, 2,000 and 1,500 and *Pa*HSS_wo_NHis with PEG 6,000, 5,000, 4,000 and 2,000. Crystals showed changes in crystal size and length but no improvement regarding X-ray diffraction.

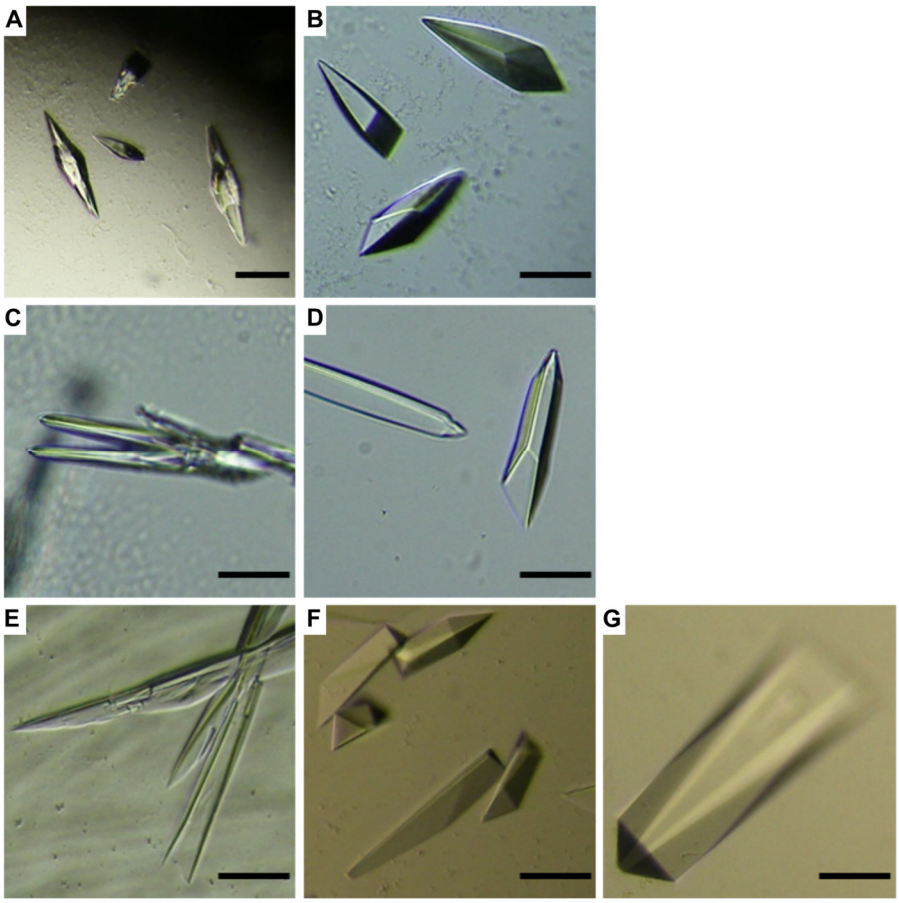

Figure 19: Crystals of *Pa*HSS grown in different crystallization conditions.

Crystals were grown in hanging drops (1 µL protein solution mixed with 1 µL reservoir solution) equilibrated against respective reservoir solutions. The composition of the Pa*HSS protein solutions was the same as stated in chapter 2.6.6 (p. 27) and contained 0.2 M agmatine sulfate. Hanging drops in* ***(A)*** *and* ***(B)*** *were prepared with* Pa*HSS_NHis, drops in* ***(C)-(G)*** *with* Pa*HSS_wo_NHis. Crystals in* ***(B)***, ***(D)***, ***(F)*** *and* ***(G)*** *were grown by streak-seeding. The reservoir solutions were* ***(A)***, ***(B)*** *0.3 M lithium citrate, 20 % (w/v) PEG 3,350;* ***(C)*** *0.2 M lithium citrate, 30 % (w/v) PEG 3,350;* ***(D)*** *0.2 M lithium citrate, 26 % (w/v) PEG 3,350,* ***(E)*** *20 µM $MgCl_2$, 0.1 M HEPES-NaOH (pH 7.5), 26 % (w/v) poly(acrylic acid sodium salt) 5,100;* ***(F)*** *20 µM $MgCl_2$, 0.1 M HEPES-NaOH (pH 7.5), 23 % (w/v) poly(acrylic acid sodium salt) 5,100;* ***(G)*** *0.1 M HEPES-NaOH (pH 7.5), 20 % (w/v) poly(acrylic acid sodium salt) 5,100, 10 µM ATP. The black scale corresponds to 50 µm.*

In another 96-well crystallization screen (PACT *premier*™ HT-96, Molecular Dimensions), *Pa*HSS_NHis but not *Pa*HSS_wo_NHis could be crystallized in several wells. Apart from PEG, these reservoir solutions contained dicarboxylic acids like succinic acid (A6), malonate (E12, G12), DL-malic acid (D4-D6) or citrate (E11). In conclusion, the presence of dicarboxylic acids seemed to be crucial for crystallization of *Pa*HSS_NHis. Still, the crystal shape was similar or worse as observed using lithium citrate and PEG 3,350.

In the JCSG-*plus*™ 96-well screen (Molecular Dimensions), *Pa*HSS_wo_NHis but not *Pa*HSS_NHis could be crystallized with a reservoir solution of 20 µL $MgCl_2$, 0.1 M HEPES-NaOH (pH 7.5) and 22 %

(w/v) poly(acrylic acid sodium salt) 5,100 (reservoir G2, similar in 24-well format in Figure 19E). Carboxylic acid groups of the polyacrylic acid seemed to promote crystallization of *Pa*HSS_wo_NHis as suggested for dicarboxylic acid groups of *Pa*HSS_NHis. Streak-seeding of crushed crystals into similar crystallization conditions gave the first trigonal prism-shaped crystals (Figure 19F). Soaking of these crystals in a mixture of 80 % reservoir solution and 20 % glycerol prior freezing in liquid nitrogen was mandatory for cryo-protection. Diffraction data collection at the synchrotron showed an increased maximal diffraction to ~3.3 Å. To further improve crystal diffraction, an additive screen using *Pa*HSS_wo_NHis and the polyacrylic acid-containing reservoir was performed by the HTX crystallization facility at the EMBL Hamburg, Germany. Significant influence on the crystal appearance was observed for 4 % (v/v) acetone, 4 % (v/v) 2-methylpropan-2-ol, 4 % (v/v) propan-1-ol and for 10 mM ATP (concentrations in reservoir solution). While addition of the organic solvents did not improve diffraction at the synchrotron, ATP significantly increased both crystal size and maximal diffraction resolution.

The optimized reservoir solution used for crystallization and structure determination of *Pa*HSS_wo_NHis (PDB ID 6Y87) finally contained 0.1 M HEPES-NaOH (pH 7.5), 18-23 % (w/v) poly(acrylic acid sodium salt) 5100 and 10 mM ATP. Initial crystals were crushed and streak-seeded into the same, freshly prepared crystallization conditions to improve crystal homogeneity (Figure 19G). Seeding-derived crystals were soaked with a mixture of 80 % reservoir solution and 20 % glycerol prior freezing in liquid nitrogen and diffraction data collection. It should be emphasized, that the concentration of polyacrylic acid within the reservoir solutions should be increased in very small steps, since homogeneous crystals were only obtained in a tiny concentration range.

As presented above, the crystallization of *Pa*HSS strongly depended on the presence or absence of the *N*-terminal histidine-tag and allowed variations of the crystallization conditions. Adjustments regarding pH, different PEGs and additives were tested with different effects on crystal appearance and diffraction quality. Especially the presence of compounds with carboxylic acids seemed to facilitate crystallization of *Pa*HSS. Concluding, further crystallization optimization might produce crystals with even better diffraction data to increase the resolution of the *Pa*HSS structure.

3.6 Structures

After successful crystallization of *Bv*HSS variants and wt *Pa*HSS, synchrotron X-ray diffraction data were collected. The structures were subsequently solved by molecular replacement. Therefore, the wt *Bv*HSS structure served as phasing model for the *Bv*HSS variants and as basis for the calculation of a *Pa*HSS phasing model. The *Bv*HSS variant structures are presented in the following to assess the previously proposed reaction mechanism of the bacterial HSS (Krossa et al. 2016). The gathered knowledge is subsequently transferred to the *Pa*HSS structure.

3.6.1 Overall comparison of Bv*HSS variant structures*

The statistics of the data collection and refinement of the *Bv*HSS variant structures and the *Pa*HSS structure are listed in Table 8. All *Bv*HSS variant structures were solved in space group $P22_12_1$ with similar unit cell dimensions and mostly refined to a resolution below 2 Å (maximum resolutions between 1.6-1.9 Å). The only exception was the structure of *Bv*HSS variant W229E, which could only be refined to a maximum resolution of 2.2 Å due to limited diffraction data quality. All *Bv*HSS structures were solved as dimers in the asymmetric unit with each subunit containing an NAD^+ molecule in the binding pocket. In addition, a PUT molecule was present at the active site of *Bv*HSS variant W229A subunit A.

The activity of each *Bv*HSS variant was tested (chapter 3.4, p. 44) to evaluate the impact of the exchanged residue on the catalytic function. However, reduced or complete loss of function of a variant is not necessarily related to direct interference with the reaction mechanism caused by the exchanged residue. Other indirect effects can also disturb the enzyme function like distortion of the protein fold, blocked access to the binding pocket or unfavorable orientation of critical side chains. Therefore, a variant structure needs to be carefully compared to the wt structure before an effect on the catalytic function can be specifically related to the properties of an individually exchanged residue.

In the following, the subunit B of the wt *Bv*HSS (PDB ID 4TVB, chain B) serves as reference structure for comparison with both the *Bv*HSS variant structures and the *Pa*HSS structure. It was chosen due to the presence of a PUT molecule at its active site, allowing comparison of substrate coordination in different structures. The overall similarity of the structures was quantified by calculating the RMSD between all equivalent atoms of two superimposed subunits. Subunits only containing alternate locations A without hydrogens, waters or ligands apart from the NAD^+ molecules were therefore superimposed in PyMOL using the “super” algorithm over 5 cycles. RMSD values were then calculated with the command “rms_cur” for the complete structures, for the majority of the “track-and-trace” loops (residues 120-130) and exclusively for the NAD^+ molecules. It should be emphasized at this point, that these RMSD values are based on all superimposed atom pairs, neither limited to C_α atoms nor biased by RMSD cutoffs.

Table 8: Data collection and refinement statistics of *Bv*HSS and *Pa*HSS structures.

	***Bv*HSS E117Q PDB ID: 6S6G**	***Bv*HSS N135F PDB ID: 6S65**	***Bv*HSS E210A PDB ID: 6S49**	***Bv*HSS E210Q PDB ID: 6S3X**	***Bv*HSS W229A PDB ID: 6S72**	***Bv*HSS W229E PDB ID: 6SEP**	***Bv*HSS W229F PDB ID: 6S4D**	***Pa*HSS PDB ID: 6Y87**
Space group	$P22_12_1$	$P22_12_1$	$P22_12_1$	$P22_12_1$	$P22_12_1$	$P22_12_1$	$P22_12_1$	$P3_212$
Cell dimensions								
a, b, c [Å]	60.3, 110.6, 158.4	60.7, 110.4, 159.5	60.0, 109.8, 157.3	60.3, 110.1, 158.2	60.1, 110.0, 157.9	60.2, 109.9, 158.2	60.1, 110.0, 158.2	103.2, 103.2, 548.0
α, β, γ [°]	90, 90, 90	90, 90, 90	90, 90, 90	90, 90, 90	90, 90, 90	90, 90, 90	90, 90, 90	90, 90, 120
Resolution [Å]	79.22 - 1.60 (1.63 - 1.60)	90.78 - 1.75 (1.78 - 1.75)	90.04 - 1.69 (1.72 - 1.69)	90.36 – 1.72 (1.75 - 1.72)	90.35 - 1.87 (1.90 - 1.87)	90.31 – 2.20 (2.28 – 2.20)	90.31 - 1.80 (1.83 - 1.80)	85 - 2.15 (2.19 - 2.15)
R_{meas}	0.133 (2.103)	0.193 (2.149)	0.230 (1.176)	0.158 (2.192)	0.197 (1.571)	1.737 (12.725)	0.218 (4.056)	0.370 (3.162)
$\langle I/\sigma I \rangle$	7.1 (0.6)	4.9 (0.4)	5.8 (1.0)	7.3 (1.0)	6.0 (0.6)	3.4 (0.8)	6.3 (0.5)	5.1 (1.0)
Completeness [%]	96.5 (53.0)	98.3 (86.9)	98.7 (73.5)	95.6 (72.0)	98.4 (69.1)	100 (100)	99.1 (98.3)	98.7 (94.1)
Redundancy	5.5 (3.1)	6.9 (6.4)	6.5 (2.5)	5.9 (5.8)	5.7 (2.1)	10.3 (9.6)	6.2 (6.2)	5.9 (5.6)
Refinement								
Resolution	60.38 - 1.60 (1.66 - 1.60)	90.78 - 1.75 (1.81 - 1.75)	63.94 - 1.69 (1.75 - 1.69)	90.36 - 1.72 (1.78 - 1.72)	90.35 - 1.87 (1.94 - 1.87)	90.31 - 2.20 (2.28 – 2.20)	90.31 - 1.80 (1.86 - 1.80)	80.31 - 2.15 (2.23 - 2.15)
No. unique reflections	134783 (9938)	106405 (9830)	115162 (9985)	107034 (8358)	85778 (7435)	53657 (5313)	96772 (9477)	179010 (17270)
R_{work}/R_{free}	0.170 / 0.197	0.180 / 0.217	0.155 / 0.186	0.163 / 0.195	0.162 / 0.205	0.193 / 0.245	0.173 / 0.208	0.203 / 0.244
CC*	0.994 (0.727)	0.999 (0.733)	0.996 (0.858)	0.993 (0.761)	0.997 (0.739)	0.908 (0.636)	0.998 (0.551)	0.993 (0.504)
CC_{work}	0.967 (0.680)	0.963 (0.689)	0.955 (0.792)	0.971 (0.735)	0.965 (0.685)	0.935 (0.520)	0.969 (0.541)	0.946 (0.534)
CC_{free}	0.950 (0.672)	0.954 (0.634)	0.957 (0.787)	0.964 (0.746)	0.939 (0.682)	0.863 (0.324)	0.959 (0.511)	0.915 (0.407)
No. atoms								
Protein	7395	7374	7468	7513	7597	7473	7539	21615
Ligand/ion	199	88	116	116	94	88	127	282
Water	877	599	1106	846	863	770	832	1242
B-factors [Å^2]								
Protein	25.7	34.4	14.9	26.2	24.6	20.9	29.3	34.3
Ligand/ion	22.8	29.7	13.3	24.8	21.5	17.4	32.5	36.1
Water	36.3	40.8	26.5	35.5	33.7	25.1	36.1	34.5
RMS deviations								
Bond lengths [Å]	0.005	0.01	0.011	0.011	0.009	0.003	0.01	0.003
Bond angles [°]	0.95	0.9	1.06	1.142	0.857	0.605	0.847	0.67
Ramachandran outliers [%]	0	0	0	0	0.11	0	0	0.26

As show in Table 9, this was done to compare the wt *Bv*HSS subunit B with the *Bv*HSS variant subunits presented in the following. The RMSD values between the wt *Bv*HSS subunits A and B were additionally calculated. These reflect randomly occurring structural deviations between the subunits of the wt *Bv*HSS dimer and help to assess the magnitude of RMSD values between wt and variant subunits.

Table 9: Superimposition of different *Bv*HSS subunits onto subunit B of wt *Bv*HSS.

The subunits listed in the first column were superimposed onto subunit B of wt Bv*HSS (PDB ID 4TVB, chain B) using the "super" algorithm over 5 cycles in PyMOL (only protein atoms, alternate locations A and NAD⁺ atoms, no hydrogens). RMSD values were calculated with the command "rms_cur" for the complete subunits including the NAD⁺ molecules (column 2), for residues 120-130 (column 3) and exclusively for the NAD⁺ molecules (column 4). In case of* Bv*HSS variant E117Q subunit B, both alternate locations A and B of the NAD⁺ molecule were compared to the NAD⁺ molecule of wt* Bv*HSS subunit B. For each RMSD value, the number of superimposed atom pairs is given in parenthesis. Subunit B of wt* Bv*HSS contains 3752 atoms (only protein atoms, alternate locations A and NAD⁺ atoms, no hydrogens). Superimposition of fewer atoms results from missing "track-and-trace" loop residues (residues 121-127 for variant E117Q (chain B) and residues 121-128 for variant N135F (chain A)), the exchange of a single residue within each variant (omitted for RMSD calculation) and missing terminal residue D477 (variants W229E, E210Q, E210A and E117Q).*

***Bv*HSS (PDB ID 4TVB, chain B) compared to:**	**all residues (incl. NAD⁺)**	**"track-and-trace" loop residues 120-130**	**NAD⁺**
*Bv*HSS (PDB ID 4TVB, chain A)	0.709 Å (3752)	0.566 Å (93)	0.571 Å (44)
*Bv*HSS variant E117Q (PDB ID: 6S6G, chain B)	0.760 Å (3673)	Loop incomplete	A: 0.594 Å (44) B: 0.275 Å (44)
*Bv*HSS variant N135F (PDB ID: 6S65, chain A)	0.682 Å (3674)	Loop incomplete	0.805 Å (44)
*Bv*HSS variant E210A (PDB ID: 6S49, chain A)	0.600 Å (3734)	1.542 Å (93)	0.889 Å (44)
*Bv*HSS variant E210Q (PDB ID: 6S3X, chain A)	0.612 Å (3734)	1.582 Å (93)	0.724 Å (44)
*Bv*HSS variant W229A (PDB ID: 6S72, chain A)	0.598 Å (3737)	1.488 Å (93)	0.758 Å (44)
*Bv*HSS variant W229E (PDB ID: 6SEP, chain B)	0.736 Å (3729)	1.583 Å (93)	0.577 Å (44)
*Bv*HSS variant W229F (PDB ID: 6S4D, chain A)	0.569 Å (3737)	1.509 Å (93)	0.767 Å (44)

The RMSD values between the two structurally very similar wt *Bv*HSS subunits A and B are 0.71 Å for the complete structures and 0.57 Å for both the "track-and-trace" loop residues 120-130 and the NAD⁺ molecules. With RMSD between 0.57-0.76 Å for complete structures, the *Bv*HSS variant subunits are comparably or even "more similar" to the wt subunit B than the wt subunit A. Significantly higher deviations are present for the "track-and-trace" loop residues of the *Bv*HSS variants (1.48-1.58 Å). Due to lack of interpretable electron density, large parts of the "track-and-trace" loops of *Bv*HSS variants E117Q subunit B (residues 121-127) and N135F subunit A (residues 121-128) are missing.

This suggests high flexibility of the loops and large deviations from the wt loop, albeit calculation of RMSD is not possible. The RMSD values for the NAD^+ molecules of the *Bv*HSS variant subunits are between 0.28-0.81 Å. Although only alternate locations A were considered for the other RMSD calculations, the two alternate locations (A and B) of the NAD^+ molecule in the *Bv*HSS variant E117Q subunit B were separately compared to the NAD^+ molecule of the wt *Bv*HSS subunit B. These alternate locations in the variant E117Q are based on the presence of both C3'-endo (alternate location A) and C2'-endo (alternate location B) NAD^+ conformers. In the wt *Bv*HSS structure, the NAD^+ molecule is exclusively present as C2'-endo conformer, explaining the lower RMSD for the C2'-endo conformer of the *Bv*HSS variant E117Q.

Concluding, the RMSD do not suggest significant structural perturbations of the *Bv*HSS variants compared to the wt structure. Increased deviations were only apparent for the "track-and-trace" loop residues 120-130, which were previously described to structurally differ between *Bv*HSS variants (Krossa et al. 2016).

In the following, the focus is shifted from the rather global evaluation of structural similarity to the detailed inspection of relevant residues involved in catalysis. The exchange of a single residue has relatively little effect on the crystal diffraction pattern of a protein. As result, most (rather global) quality criteria for crystallographic structures are not affected by the actual location and conformation of single residues. The reliability of the model regarding the exchanged residues therefore needs to be judged based on local criteria like the corresponding electron density maps. For this purpose, omit maps were calculated for all variants presented in this work (2mFo-DFc omit map in image I and mFo-DFc omit map in image II of respective depictions). This entailed omitting a stretch of 21 residues from the model with the exchanged residue situated in the middle of this stretch or omitting of a single PUT molecule. After refinement of these truncated models including simulated annealing, omit maps were calculated. The resulting maps only rely on the combination of the diffraction data and the phase information of the truncated model. The electron density distribution belonging to the omitted model parts is therefore free from model bias and should indicate the correct location of the omitted model parts. The quality of these maps depends on sufficient diffraction data quality, low flexibility and high occupancy of the omitted model parts. Concluding, the quality of these omit maps reflects the reliability of the modeled residues (and of the PUT molecule) in this work.

In general, the locations of most of the relevant residues (including D94, E117, Y123, E210, W229, E237, H296, E298 and the side pocket residue N135) are highly similar or even identical to the residues of the wt structure. Structural deviations of some residues were still detected, which are discussed below together with the conformation of the intentionally exchanged residues.

3.6.2 Bv*HSS variants targeting residue W229*

The *Bv*HSS residue W229 was proposed to play a central role in the reaction mechanism by stabilizing cationic intermediates/transition states via cation-π interaction. It was possible to solve the structures of the *Bv*HSS variants W229F (PDB ID 6S72), W229E (PDB ID 6SEP) and W229A (PDB ID 6S72). The agreement between the modeled residues at the active sites and their underlying electron density distributions are examined in Figure 20, with images A-C and E showing the same section of the active sites.

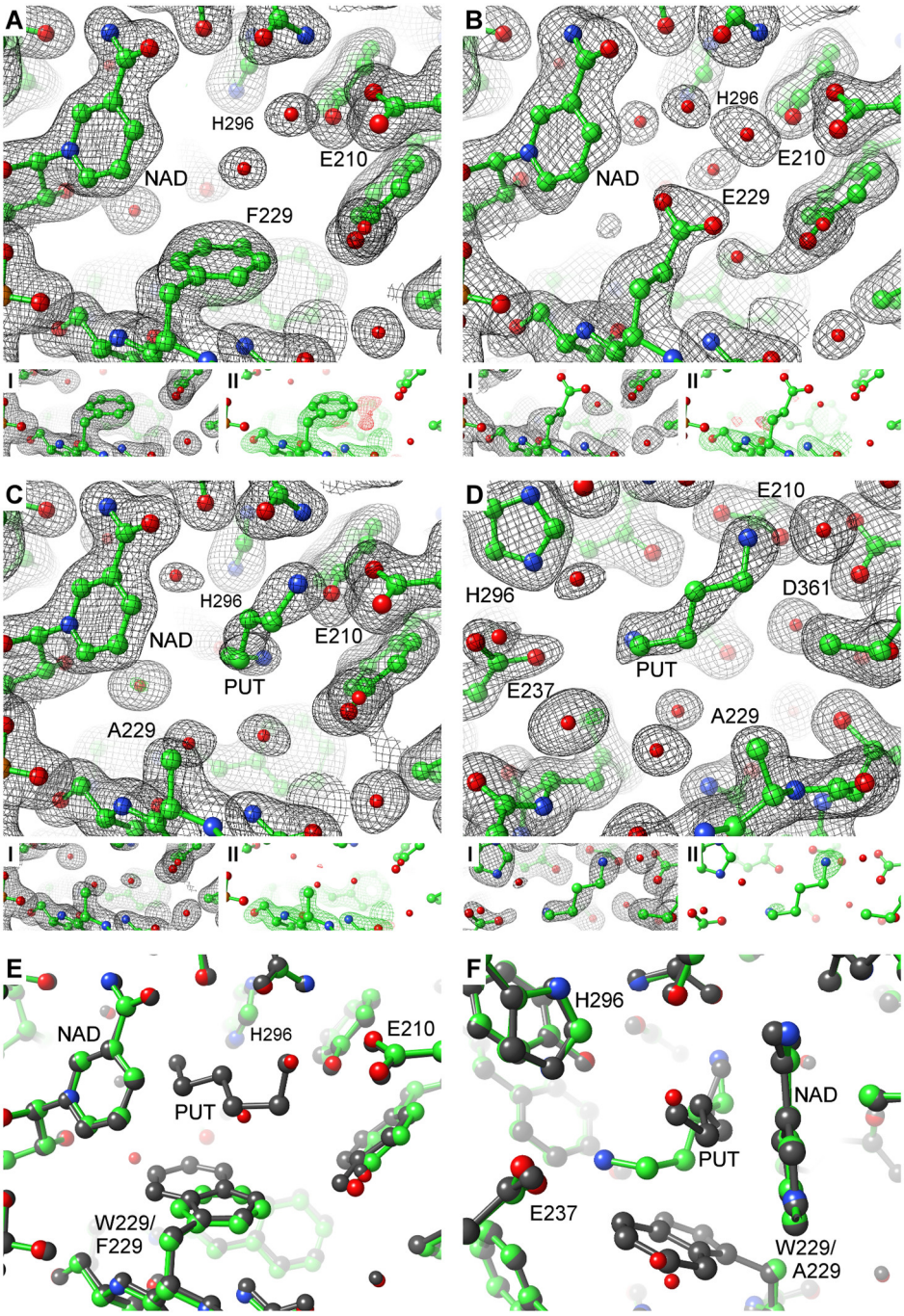

Figure 20: Active sites of *Bv*HSS variants W229F, W229E and W229A.

(A) Bv*HSS variant W229F (PDB ID 6S4D, chain A),* ***(B)*** *variant W229E (PDB ID 6SEP, chain B) and* ***(C/D)*** *variant W229A (PDB ID 6S72, chain A),* ***(E/F)*** *Superposition of the wt BvHSS structure (PDB ID 4TVB, chain B, grey ball-and-stick representation) onto the variant W229F (E) and onto the variant W229A (F). Atomic models of* Bv*HSS variants are depicted as colored ball-and-stick representations and electron density maps as mesh. The contouring was set to 1 σ for 2mFo-DFc maps (black) and to +/- 4 σ for mFo-DFc maps (green/red). (A-D) Large images show the 2mFo-DFc and mFo-DFc maps of the complete models, corresponding omit maps of partial models are given in the smaller images below (2mFo-DFc in* ***I*** *and mFo-DFc in* ***II****). Omit maps were calculated by the composite_omit_map program of Phenix after first omitting residues 219-239 (A-C, I and II) or the PUT molecule (D, I and II) followed by refinement including simulated annealing.*

Most notably, the nicotinamide ring as hydride acceptor/donor, residue H296 as proton acceptor/donor, residue E210 as stabilizer of “inner” amino groups of reaction components and the exchanged residue number 229 are visible. The variant residues F229 and A229 are distinctly contoured by their electron density maps. The conformation of the residue E229 is not completely supported by the omit maps (Figure 20B-I/II) due to lacking contouring of the carboxyl group at 4 σ. A limited map quality in general is perceivable due to the lower resolution of the *Bv*HSS W229E structure compared to the other variants. The poor contouring of residue E229, especially in the omit maps, might be caused by flexibility of the residue or radiation damage (partial loss of the side chain carboxyl group).

Apart from the placement of the exchanged residue in each variant, the complete binding pockets of the variants were evaluated for structural deviations from the wt structure. Superimposition of the wt *Bv*HSS subunit B (PDB ID 4TVB) onto the respective variant subunits shows a high structural conservation of the binding pocket residues. The variant residue F229 almost perfectly aligns to the wt residue W229 with both ring moieties lying in the same plane (Figure 20E). The F229 phenyl ring thereby superimposes onto the pyrrole ring of W229. The variant residue E229 is equally positioned as the wt residue W229 up to atom Cβ. However, the E229 carboxyl group is not lying in the plane of the wt indole ring but points into the space of the active site. The variant residue A229 basically matches to the structure of the wt residue W229 but lacks the bulky indole group. Also, a PUT molecule was located at the active site of the variant W229A subunit A. It is depicted in two orientations (Figure 20C/D) with the image plane of (D) being parallel to the plane of the NAD^+ nicotinamide ring. Although the carbon chain of the PUT molecule is not completely contoured by the mFo-DFc omit map (D-II), the 2mFo-DFc omit map (D-I) more clearly defines the location of the molecule. In (F), the coordination of the PUT molecule is compared between the variant and the wt structure. Superimposition of the two structures reveals an almost identical location of all active site residues. Only the carboxyl group of E237, being part of the catalytic triad, and the NAD^+ amide group slightly differ between both structures due to rotation of these terminal groups by a few degrees. More obviously, the PUT molecules are differently placed in the wt and the W229A variant structure. The “innermost” amino group of both PUT molecules is similarly placed near the carboxyl group of E210 with a distance of 2.7 Å for the variant structure and 3.0 Å for the wt structure (PUT N – E210 OE2). The outermost amino group is shifted towards the carboxyl group of residue E237 in the W229A variant (distance 3.3 Å) compared to the wt protein (distance 4.4 Å). The “wildtype location” of the outer amino group is thereby occupied by a water molecule in the variant structure. This shift of the amino group could be attributed to the missing cation-π interaction partner in the W229A variant. As result, the amino group at the “central amino site” is attracted by the carboxyl group of residue E237 and thereby pulled away from the center of the active site. Such a shift of the “outermost” PUT nitrogen would be energetically unfavorable in the wt structure due to steric repulsion by the W229 indole ring.

Concluding, the active sites of the presented variants are structurally intact with differences mainly limited to the exchanged residues. Decreased or lacking activity should therefore be caused by the respective exchange of residue W229. To discuss the role of residue W229 in the following, the structural evaluation of the corresponding *Bv*HSS variants is combined with the results of their activity assays.

The variant residue A229 cannot stabilize cationic reaction components and was consistently shown to be completely inactive.

The variant residue E229 could potentially serve as salt bridge interaction partner for cations via its carboxyl group but also turned out to be inactive. The failure to compensate for a tryptophan residue could be based on the different interaction principles (cation-π interaction vs. salt bridge). Another explanation would be a steric clash between substrate and the E229 carboxyl group, which points into the active site. A future *Bv*HSS W229D variant with less steric requirement of the side chain could further elucidate this question.

The *Bv*HSS variants W229F and W229Y (failed crystallization) were shown to produce HSP, albeit with very little activity. In the structure of the W229F variant, the phenyl ring lies in the same plane as the indole ring. Regarding the high similarity of both structures apart from the size of the side chain rings, the decreased activity of the variant should be caused by a less efficient cation-π interaction. First, the phenyl ring exhibits weaker cation-π interaction potential due to a smaller π-electron system with less negative partial charge compared to the indole ring (Mecozzi et al. 1996a; Reddy and Sastry 2005). Second, the center of the F229 phenyl ring aligns to the center of the pyrrole moiety but not to the benzene moiety of the wt W229 indole ring. Comparing the (imagined) interaction geometry between (I) the amino group at the “center amino site” and (II) the variant F229 phenyl ring or the wt W229 benzene moiety, the variant phenyl ring is more “off-centered” and therefore energetically less favorably positioned for cation-π interaction (Marshall et al. 2009).

The *Bv*HSS variants W229K and W229H were both inactive and could not be crystallized. The variant W229K served as “negative control” since the basic residue K229 should electrostatically repel basic reaction components. However, steric repulsion of the substrate by the long side chain of lysine could also render the variant inactive. With the findings of the other variants sufficiently confirming the role of residue W229, the exact reason becomes obsolete. Failing to crystallize the *Bv*HSS variant W229H, the orientation of the H229 side chain as prerequisite for efficient cation-π interaction could not be determined. However, notable stabilization of cationic reaction components by the π-system of the imidazole ring, even providing optimal interaction geometry, can be doubted. The imidazole ring was previously disqualified regarding cation-π interactions based on quantum mechanical calculations (Mecozzi et al. 1996a; Reddy and Sastry 2005). Altogether, the presented W229 variant structures together with the activity assays confirm the role of W229 as cation-π interaction partner in the reaction mechanism.

3.6.3 Bv*HSS variants targeting residue E210*

The *Bv*HSS residue E210 was shown to coordinate to the “innermost” amino group of reaction components throughout the reaction mechanism. The structures and electron density maps of the variants E210Q and E210A with focus on the exchanged residues are depicted in Figure 21A/B. Superimposition of the variant structures onto the wt structure revealed nearly identical locations of the binding pocket residues. In fact, the variant residue Q210 and the wt residue E210 are almost equally situated and are not distinguishable based on their electron densities. For both variants, the exchanged residues are strongly supported by their respective omit maps. Concluding, the inactivity of both variants can be explained by the removal of the indispensable negative charge at position 210.

In line with this, the *Bv*HSS variant E210K with its positive charge as “negative control” was also inactive, albeit crystallization and structural inspection was not possible.

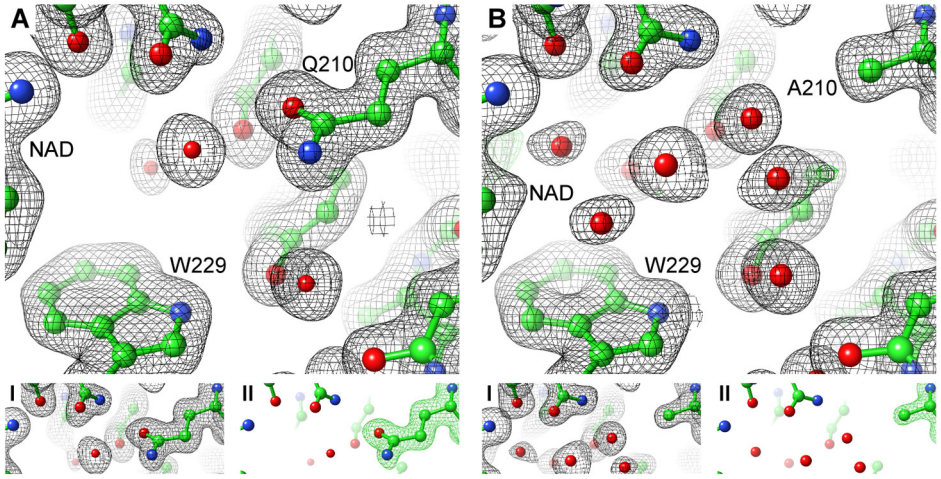

Figure 21: Binding pocket sections of *Bv*HSS variants E210Q and E210A.
(A) *BvHSS variant E210Q (PDB ID 6S3X, chain A),* ***(B)*** *variant E210A (PDB ID 6S49, chain A). Atomic models are depicted as ball-and-stick representations and electron density maps as mesh. The contouring was set to 1 σ for 2mFo-DFc maps (black) and to +/- 4 σ for mFo-DFc maps (green/red). Large images (A/B) show the 2mFo-DFc and mFo-DFc maps of the complete models, corresponding omit maps of partial models are given in the smaller images below (2mFo-DFc in* ***I*** *and mFo-DFc in* ***II****). Omit maps were calculated by the composite_omit_map program of Phenix after first omitting residues 200-220 followed by refinement including simulated annealing.*

3.6.4 Bv*HSS variants targeting residues E117 and D94*

The *Bv*HSS residue E117 is part of the “ionic slide”, which is proposed to lead substrates from the pocket entrance into the active site. Figure 22A illustrates the “ionic slide” of the *Bv*HSS variant E117Q together with corresponding electron density maps. The section depicts a view from the pocket entrance into the binding pocket. Most important, the residue D94 as upper part of the “ionic slide”, the variant residue Q117 and parts of the nicotinamide riboside moiety of the NAD^+ molecule are visible. The exchanged residue Q117 is distinctly contoured by electron density, including the omit maps. However, die variant structure partly deviates from the wt structure as shown in the superposition of both structures (Figure 22B). The complete residue Q117, including its main chain and side chain, is shifted compared to the wt residue E117. In addition, the electron density of the nicotinamide riboside moiety was interpreted as two alternate locations composed of a C2’-endo and a C3’-endo conformer. The shift of residue Q117 can be explained by an increased flexibility of the variant “track-and-trace” loop. Due to lack of interpretable electron density, a large part of the loop could not be modelled in the variant structure (residues 123-127 and 121-127 missing in subunit A and B, respectively). The traceable remaining part of the loop, especially residue Q117, is still moderately affected by this deviation. Alternate locations for the “track-and-trace” loop have been described before and were suggested to regulate the accessibility to the binding pocket (Krossa et al. 2016). The absence of traceable electron density in the *Bv*HSS variant E117Q complicates predictions about the pocket accessibility. Still, a complete occlusion of the entrance by a highly flexible loop is rather unlikely.

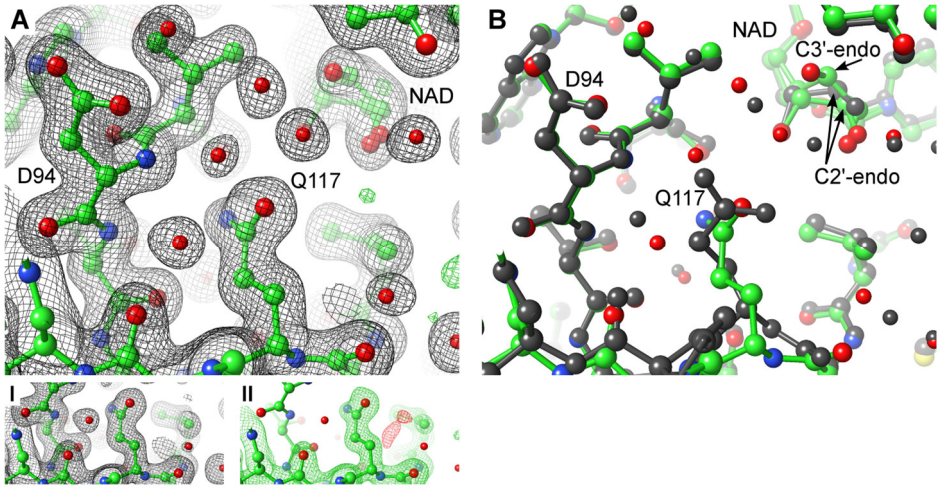

Figure 22: Binding pocket section of *Bv*HSS variant E117Q.

The atomic model of Bv*HSS variant E117Q (PDB ID 6S6G, chain B) is depicted as colored ball-and-stick representation and electron density maps as mesh. The contouring was set to 1 σ for 2mFo-DFc maps (black) and to +/- 4 σ for mFo-DFc maps (green/red).* ***(A)*** *The large image shows the 2mFo-DFc and mFo-DFc maps of the complete model, corresponding omit maps of the partial model are given in the smaller images below (2mFo-DFc in* ***I*** *and mFo-DFc in* ***II****). Omit maps were calculated by the composite_omit_map program of Phenix after first omitting residues 107-127 followed by refinement including simulated annealing.* ***(B)*** *Superimposition of the wt* Bv*HSS structure (PDB ID 4TVB, chain B, grey ball-and-stick representation) onto the variant structure E117Q.*

The shifted residue Q117, including its main chain, does not block the pocket entrance as its side chain is rather shifted away from the entrance tunnel. Comparing the NAD^+ molecules, the wt structure exclusively contains the C2'-endo conformer with the corresponding C2D atom lifted farther out of the furanose plane compared to the C2'-endo conformer of the variant. The NAD^+ O2D oxygens of both the C2'-endo and the C3'-endo conformers in the variant structure are shifted compared to the wt C2'-endo conformer, slightly narrowing the solvent-accessible space of the active site (not shown). In addition, the O2D oxygen was previously shown to be involved in the coordination of the N11 nitrogen ("outer amino site") of the HSP molecule in the wt structure (PDB ID 4TVB, chain A) (Krossa et al. 2016). The *Bv*HSS variant E117Q subunit B was superimposed onto the wt subunit A to measure the distances between the HSP N11 atom (of the wt structure) and the respective O2D atoms of the wt and variant structures. These amounted to 3 Å for the wt structure and 2.5 Å/2.6 Å for the two conformers of the variant structure. Taken together, the coordination of the HSP N11 atom in the variant should be stronger but the active site space slightly smaller.

In summary, the *Bv*HSS variant E117Q exhibits a highly flexible and partly not traceable "track-and-trace" loop, a shifted location of residue Q117 and alternate locations for the ribose of the nicotinamide riboside moiety. The variant was shown to only retain little activity. This could be attributed to the disruption of the "ionic slide" by removal of the acidic carboxyl group. Still, an influence of the other structural deviations on the activity cannot be ruled out. Introduction of a basic side chain by generation of the *Bv*HSS variant E117K completely inactivated the enzyme. However, crystallization of this variant was not possible so that steric repulsion caused by the long lysine side chain or other structural disturbances are possible. The activities of the *Bv*HSS variants D94N and D94K were only moderately decreased with D94N being more active than D94K. Structural inspection of these variants was not possible due to poor X-ray diffraction by their crystals. Assuming that the activities of the

variants were governed by electrostatic and not structural effects, two conclusions can be drawn. First, the degree of shifting the negative electrostatic potential to positive potential correlates to decreasing catalytic activity for both residues D94 and E117. Second, the electrostatic potential of residue E117 thereby exerts a higher influence on the activity than the electrostatic potential of residue D94. Consistently, sequence alignment of bacterial HSS orthologues reveals that only ~40 % of HSS orthologues contain an acidic residue at the position equivalent to *Bv*HSS D94 (Shaw et al. 2010), suggesting lesser importance of a negative charge at this position.

3.6.5 *BvHSS variants targeting residues N135 and V116*

The binding pocket of *Bv*HSS exhibits a significant side pocket, which was speculated to allow accommodation of larger reaction components. Since the function of this side pocket was not experimentally examined so far, *Bv*HSS variants were designed in this thesis to modify the side pocket. Relevant side chains, which mainly form the side pocket without major contribution to the architecture of the active site, belong to the residues V115, V116, N135, L138, C158 and N297. Aiming to fill the side pocket with a bulky side chain without constriction of the active site space, the *Bv*HSS variants V116F and N135F were designed. The structure and electron density maps of the variant residue F135 are depicted in Figure 23, together with the side pocket residues V115, L138 and the “ionic slide” residue E117.

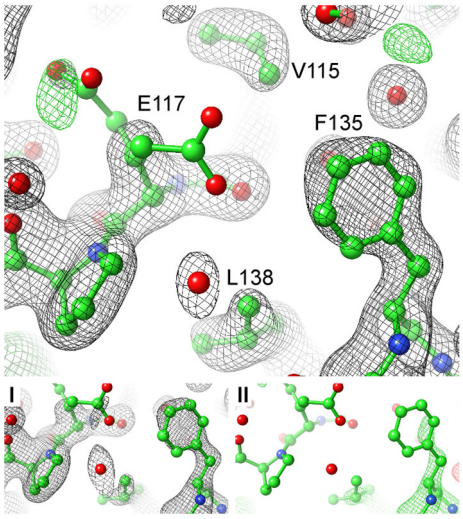

Figure 23: Binding pocket section of *Bv*HSS variant N135F.
The atomic model of Bv*HSS variant N135F (PDB ID 6S65, chain A) is depicted as ball-and-stick representation and electron density maps as mesh. The contouring was set to 1 σ for 2mFo-DFc maps (black) and to +/- 4 σ for mFo-DFc maps (green/red). The large image shows the 2mFo-DFc and mFo-DFc maps of the complete model, corresponding omit maps of the partial model are given in the smaller images below (2mFo-DFc in* ***I*** *and mFo-DFc in* ***II****). Omit maps were calculated by the composite_omit_map program of Phenix after first omitting residues 125-145 followed by refinement including simulated annealing.*

The electron density map of the complete model in combination with the omit maps clearly outlines the location of F135, although the phenyl ring is not completely supported by positive density in the mFo-DFc map at 4 σ. The electron density for the side chain of residue E117, however, is not visible in the 2mFo-DFc map at a contouring of 1 σ. The residue was placed at two alternate locations based on a

lower contouring level. However, a high conformational flexibility of this residue not restricted to these conformers should be assumed for the following discussion. Several additional structural deviations from the wt structure were detected for the *Bv*HSS variant N135F. These deviations and the impact on the solvent-accessible surface of the binding pocket are illustrated in Figure 24.

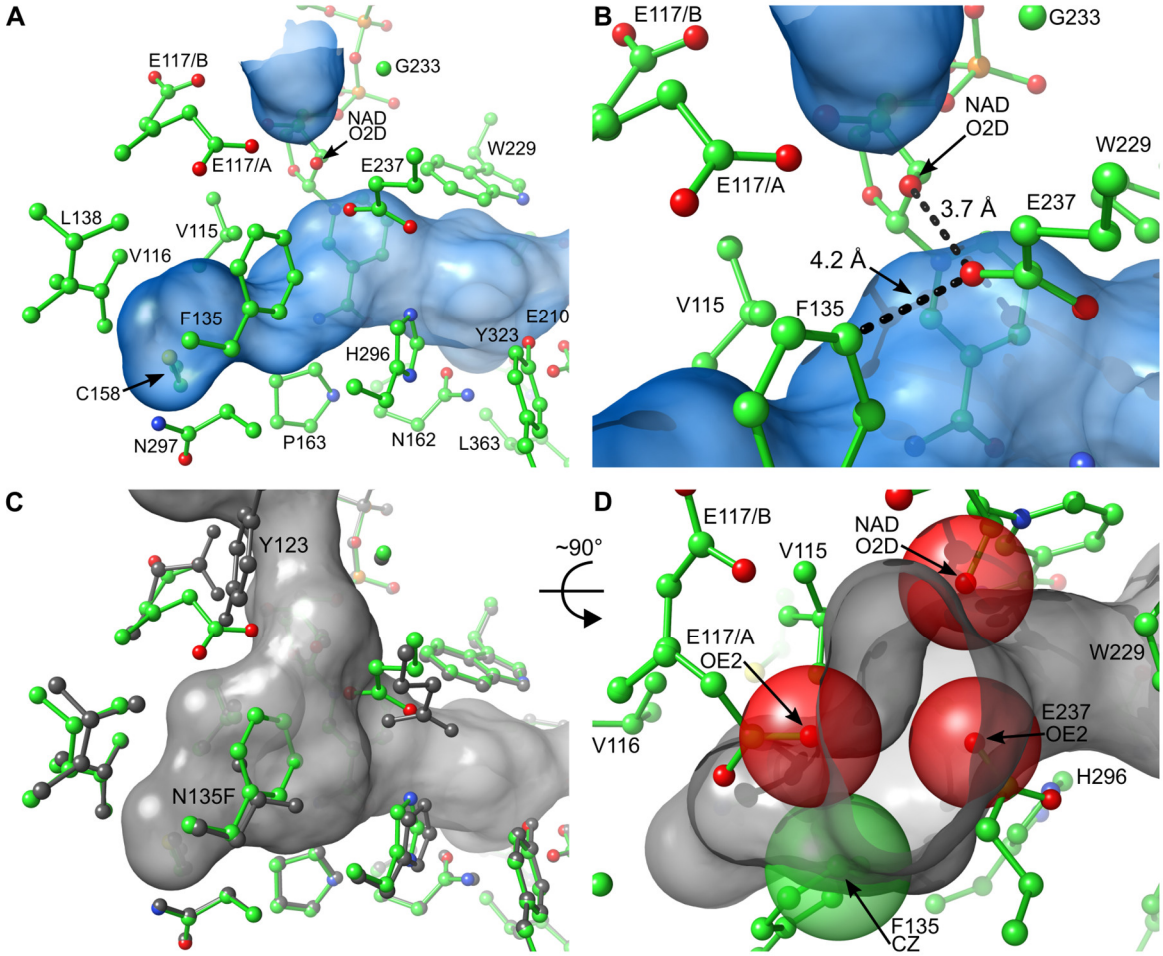

Figure 24: Constriction of the binding pocket entrance of the *Bv*HSS variant N135F.

The surfaces of solvent-accessible binding pockets are rendered transparent and colored grey for the wt Bv*HSS (PDB ID 4TVB, chain B) and blue for the* Bv*HSS variant N135F (PDB ID 6S65, chain A). The corresponding side chains contributing to the respective surfaces are shown as ball-and-stick representation.* ***(A)*** *Side chains and binding pocket of* Bv*HSS variant N135F with constriction of the lower part of the entrance tunnel near oxygen O2D of NAD⁺ and carboxyl group oxygens of E237 and E117 (alternative conformation A). Due to the absence of the "track-and-trace" loop in the model, including residue Y123, the upper part/pore of the binding pocket entrance is not definable.* ***(B)*** *Enlarged section of (A) with distances between the variant atoms NAD⁺ O2D - E237 OE2 - F135 CZ, calculated by the program PyMOL and depicted as dashed lines.* ***(C)*** *The wt* Bv*HSS together with the surface of its binding pocket (both in grey) was superimposed onto the* Bv*HSS variant N135F (colored). The same side chains as in (A) are shown together with corresponding wt side chains and wt side chain Y123. High deviations between variant and wt residues with impact on the binding pocket occur for E117, L138, E237, H296 and due to the mutation N135F.* ***(D)*** *Enlarged and rotated section of (C) without the residues of wt* Bv*HSS. Van der Waals surfaces of NAD⁺ O2D, E237 OE2 and E117 OE2 (alternative conformation A) and F135 CZ are shown as transparent spheres (oxygen: r = 1.52 Å, red; carbon: r = 1.70 Å, green).*

Large stretches of the "track-and-trace" loop could not be traced for the variant due to a lack of electron density (residues 121-128 and 121-130 missing in subunit A and B, respectively). These

missing parts of the loop, especially residue Y123, are involved in the formation of the pore and entrance tunnel of the binding pocket. Only the lower part of the solvent-accessible pocket surface, including the active site and the side pocket, could therefore be calculated. This surface together with the contributing side chains is depicted in Figure 24A. The variant side chain F135 borders the side pocket and causes a constriction with its phenyl ring. Still, a complete occlusion of the side pocket was not achieved. Far more significantly, an obstruction of the entrance tunnel is visible, separating the upper and lower part of the binding pocket. The constriction is caused by the carboxyl group oxygen OE2 of E237, by E117 OE2 (alternate location A) and by the atom O2D of the NAD^+ molecule. Even more, E117 (alternate location A) is considered as upper border of the variant side pocket in the surface calculation due to absence of the “track-and-trace” loop. Assuming the side chain of E117 to be quite flexible, the alternate location A of residue E117 should not permanently contribute to the constrictions, neither regarding the entrance tunnel nor the side pocket border. As result, the uncertain location of the side chain E117 together with the missing residue Y123 in the *Bv*HSS variant N135F prevent unambiguous calculation of the surfaces of the tunnel entrance and of the side pocket. Still, several assumptions were made by the following approach. An enlarged section of the tunnel constriction with distance measurements between atoms NAD^+ O2D, E237 OE2 and F135 CZ is depicted in Figure 24B. The smallest distance of 3.7 Å was measured between E237 OE2 and NAD^+ O2D, while the distance between E237 OE2 and F135 CZ amounts to 4.2 Å. To better assess the meaning of these distance measurements and the structural differences between the *Bv*HSS variant N135F and the wt structure, both structures were superimposed onto each other (Figure 24C). The same side chains of *Bv*HSS variant N135F as shown in Figure 24A are depicted together with the corresponding wt side chains. In addition, the wt side chain Y123 was added, which is missing in the variant structure. The surface of the wt binding pocket is also shown to clarify the effects of the variant structure on the surface of its binding pocket. Minor structural deviations are visible for the variant side chains L138, slightly shifted away from the wt surface, and H296, slightly shifted towards the surface. Residue L138 thereby expands the side pocket in the variant while residue H296 narrows the active site, albeit both effects are relatively small. Far more significantly, the phenyl ring of the variant side chain F135 penetrates the wt surface, causing the mentioned narrowing of the side pocket. Similarly, atom E237 OE2 deeply penetrates the wt binding pocket, while atoms NAD^+ O2D and E117 OE2 (alternate location A) are merely shifted towards the wt surface. Magnification of Figure 24C and rotation by ~90° results in Figure 24D. Only the side chains belonging to the *Bv*HSS variant N135F are shown for simplicity. To illustrate the constricting effect of the respective side chains, the van der Waals radii (r_W) of atoms NAD^+ O2D, E117 OE2 (alternate location A), F135 CZ and E237 OE2 are depicted as transparent spheres (oxygen: r_W = 1.52 Å, red; CZ: r_W = 1.70 Å, green). For the calculation of the solvent-accessible surface of the binding pocket using the program HOLLOW, the r_W of the protein atoms and the “void-filling” dummy atoms (r_W = 1.4 Å) are considered. Thereby, dummy atoms were placed into the pocket without overlap with protein atoms at the level of their r_W. Figure 24D exemplifies how atom E237 OE2, supported by atoms NAD^+ O2D and F135 CZ occludes the entrance to the active site. The distance between the spheres/van der Waals surfaces can be calculated by subtraction of the respective r_W from the distance measurements in Figure 24B. These distances amount to 0.66 Å for NAD^+ O2D - E237 OE2 and to 0.98 Å for E237 OE2 - F135 CZ. Concluding,

these atoms do not leave enough space for passage of a water molecule (r_W of 1.44 Å) and consistently prevent access to the active site. This constriction is independent of the (presumably flexible) side chain E117. However, these assumptions are principally based on the superimposition of the *Bv*HSS variant N135F structure onto the wt binding pocket surface. As mentioned before, absence of the “track-and-trace” loop and unsure location of the side chain E117 in the variant structure prevent definite calculation of its binding pocket surface.

Activity measurement revealed little activity of the *Bv*HSS variant N135F. Introduction of phenylalanine at position 135, however, did not completely occlude the side pocket. Instead, the reduced activity can be assumed to mostly originate from the steric constriction of the binding pocket entrance, which is caused by the exchange of residue N135 together with other structural perturbations. The remaining activity could be attributed to the presumably flexible “track-and-trace” loop, providing limited access to the active site. Concluding, the *Bv*HSS variant N135F does not qualify for the evaluation of the side pocket function. The *Bv*HSS variant V116F, also designed to modify the side pocket, did not show significantly reduced activity in a qualitative activity test. Also, poor diffraction of the crystals prevented determination of the structure. The influence of residue F116 on the side pocket therefore remains unknown and the role of the side pocket could not be elucidated in this thesis.

3.6.6 B*v*HSS variants targeting residue Y123

The *Bv*HSS residue Y123 together with the residual “track-and-trace” loop was previously proposed to regulate the dimension of the pocket entrance (Krossa et al. 2016). Several variants with exchange of the tyrosine (Y123E, Y123F. Y123S, Y123K) were designed in this thesis to examine effects on the “track-and-trace” loop and the pore dimensions. In qualitative activity tests, these variants were confirmed to be active. The majority of the “track-and-trace” loop, including residue 123, was not traceable in the variant structures due to lack of interpretable electron density. Neither being able to locate the exchanged residues in the structures nor detecting a significant effect on the activity, these structures were not further examined. Missing parts of the “track-and-trace” loop were similarly observed for the *Bv*HSS variants E117Q and N135F and could be explained by a high flexibility of the loop. Evaluation of various structures revealed a tendency of the “track-and-trace” loop to be more defined and therefore “rigid” in structures of completely inactive variants (*Bv*HSS variants E210Q, E210A, W229A, W229E in this thesis and variant E237Q described by Krossa *et al.*. In the inactive variant H296S, the electron density of the “track-and-trace” loop was interpreted as two alternate locations by Krossa *et al.*. One explanation for the rigidity could be a reduced shuttling of reaction components in inactive variants, allowing the loop to settle in a defined location. If the loop “actively” regulates the dimensions of the pocket entrance or rather passively adopts to the shuttling of reaction components, remains to be determined.

3.6.7 Comparison of P*aHSS molecules in the asymmetric unit*

Hoping that structural insights retrieved from the *Bv*HSS variants are transferable to medically more relevant enzymes, the structure of the *Pa*HSS was solved. The corresponding data collection and refinement statistics are listed in Table 8 (p. 54). The *Pa*HSS structure was solved in space group $P3_212$ with six *Pa*HSS molecules in the asymmetric unit, refined to a maximum resolution of 2.15 Å. All

residues of molecule A could be modeled into the electron density distribution, including a leftover residue of the cleaved affinity tag at the N-terminus (residue 0). Due to absence of interpretable electron density, the other molecules lack a few residues belonging to the N-terminal loop and/or to a loop near the C-terminus (missing residues in *Pa*HSS molecules B: 1-3; C: 1-5 and 449-458; D: 1-4 and 449-457; E: 1-3 and 451-456; F: 1-3 and 450-457). These two incomplete loops are exposed to the solvent at the protein surface, neither affecting the binding pocket nor the (crystalline) dimer interface (see below). While all six *Pa*HSS molecules contain an NAD^+ molecule in their binding pockets, PUT molecules are additionally present at the active sites of molecules A, C and E. Crystal contacts between the individual protein molecules were determined by the web server PDBsum (Laskowski et al. 2018). Apart from various smaller to moderate contact interfaces between the molecules, the largest interface areas were detected between the pairwisely associated molecules A - B (1381 $Å^2$-1401 $Å^2$), C - D (1328 $Å^2$-1332 $Å^2$) and E - F (1379 $Å^2$-1370 $Å^2$). Although the *Pa*HSS was shown by SEC-MALS to be a monomer in solution, the interface areas qualify for stable dimerization of the six protein molecules into three dimers within the asymmetric unit. Superimposition of these *Pa*HSS dimers onto the wt *Bv*HSS dimer (PDB ID 4TVB) revealed a highly similar quaternary structure of both *Bv*HSS and *Pa*HSS dimers. Concluding, both *Bv*HSS and (crystalline) *Pa*HSS dimers associate via equivalent dimerization interfaces. In addition, each (crystalline) *Pa*HSS dimer in the asymmetric unit exhibits one PUT molecule within one subunit. If this distribution of PUT molecules is caused by a structural regulation or just coincidence, remains unknown.

The degree of structural similarity between the *Pa*HSS molecules was examined by comparing the individual molecules to the completely modeled molecule A using the “super” algorithm and the “rms_cur” command in PyMOL (Table 10).

Table 10: Superimposition of the *Pa*HSS molecules onto *Pa*HSS molecule A.

The structural similarity of the Pa*HSS molecules (PDB ID 6Y87) was examined by superimposition onto molecule A using the “super” algorithm over 5 cycles in PyMOL (only protein atoms, alternate locations A and NAD^+ atoms, no hydrogens). RMSD values were calculated with the command “rms_cur” for the complete protein molecules including the NAD^+ molecules (column 2), for residues 110-119 (column 3), for residues 120-124 (column 4) and exclusively for the NAD^+ molecules (column 5). For each RMSD value, the number of compared, superimposed atom pairs is given in parenthesis. These numbers differ due to missing residues depending on the* Pa*HSS molecule (see text).*

***Pa*HSS chain A (PDB ID: 6Y87) compared to:**	**all residues (incl. NAD^+)**	**“track-and-trace” loop**		**NAD^+**
		residues 110-119	**residues 120-124**	
*Pa*HSS chain B	0.791 Å (3675)	0.548 Å (80)	1.603 Å (38)	0.300 Å (44)
*Pa*HSS chain C	0.828 Å (3597)	0.529 Å (80)	0.985 Å (38)	0.638 Å (44)
*Pa*HSS chain D	0.807 Å (3605)	0.578 Å (80)	0.949 Å (38)	0.708 Å (44)
*Pa*HSS chain E	0.827 Å (3640)	0.668 Å (80)	2.228 Å (38)	0.384 Å (44)
*Pa*HSS chain F	0.729 Å (3619)	0.559 Å (80)	1.078 Å (38)	0.370 Å (44)

The overall structure of the molecules is very similar with RMSD (including all atoms, not limited to C_α) ranging between 0.73-0.83 Å. Distinct structural differences are limited to loop regions at the surface,

which are neither part of the binding pocket nor of the (crystalline) dimer interface. An equivalent “track-and-trace” loop, named according to the corresponding loop in the *Bv*HSS structure, is also present in the *Pa*HSS structure (residues 110-124). The largest part of this loop (residues 110-119), which is lining the binding pocket, is very similarly located in the *Pa*HSS molecules (RMSD between 0.53 Å-0.67 Å). Relatively high structural deviations only occur for a small stretch of residues 120-124 outside the binding pocket (0.95 Å-1.08 Å for molecules C, D and F; 1.60 Å and 2.23 Å for molecules B and E). As determined via the PDBsum web server, each *Pa*HSS molecule within the asymmetric unit exhibits crystal contacts between this outer part of the “track-and-trace” loop and residues of another protein molecule. Without going into detail, two different patterns of crystal contacts were found in the crystal. The first pattern includes loop residues P122 and T123 of molecules C, D and F, which show similar, weak non-bonded crystal contacts to residues I68 and Q67 of a symmetry-related molecule C, molecule F and molecule D, respectively. The second pattern comprises loop residues D121, P122 and T123 of molecule A, B and E in contact with Y39, K59, I61 and I77 of a symmetry-related molecule C, molecule F and a symmetry-related molecule D, respectively. Apart from non-bonded contacts, residue D121 of both molecules B and E thereby forms a salt bridge to residue K59 of molecule F and of the symmetry-related molecule D, respectively. In addition, residue D121 of molecule E also forms a hydrogen bond to residue Y39 of the symmetry-related molecule D.
In conclusion, the outer parts of the “track-and-trace” loops (residues 120-124) of molecule B and even more of molecule E are involved in the strongest crystal contacts. Simultaneously, these loop parts of molecules B and E exhibit the highest RMSD compared to molecule A. The high structural deviations of residues 120-124 should therefore rather be based on different crystal contacts of the respective *Pa*HSS molecules than on physiological conformations of the “track-and-trace” loop.

3.6.8 Binding pocket and active site of Pa*HSS*

The overall structure of the *Pa*HSS molecule A including the bound NAD^+ molecule and the solvent-accessible surface of the binding pocket is depicted in Figure 25A. Same as the *Bv*HSS and confirmed by the CATH database (Knudsen and Wiuf 2010), the *Pa*HSS is composed of an “NAD(P)-binding Rossmann-like” domain (residues 1-155 and 389-419) and an “HSS-like” domain (residues 156-388 and 420-469). According to the CATH database, only residues 400-409 of the α-helix comprising residues 389-409 were ascribed to the Rossmann-like domain. This would assign one half of the helix to the HSS-like domain and thereby fuse both domains via this helix. Consistent with the definition of the Rossmann-like domain (β-sheet containing up to seven β-strands sandwiched by a varying number of α-helices) and based on the spatial assembly of the secondary structures, the complete α-helix was assigned to the Rossmann-like domain in this thesis. The binding pocket is formed between both domains and accommodates an NAD^+ molecule. The nicotinamide moiety thereby reaches into the pocket and is part to the active site. The surface of the binding pocket surrounded by the catalytically relevant residues (and residues Y119 and N131) is depicted in Figure 25B. From this point of view, the NAD^+ molecule contributes to the back of the binding pocket together with the “ionic slide” formed by residues D90 and E113. Residue Y119 as part of the “track-and-trace” loop lines the left side of the entrance. The side pocket is the extension at the bottom left, confined by residue N131.

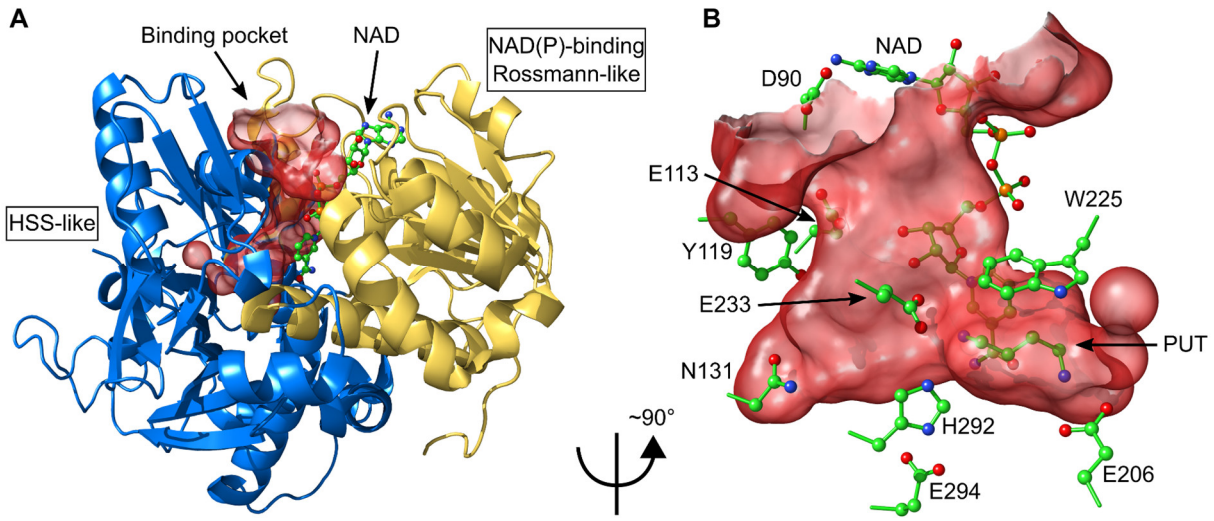

Figure 25: Structure and binding pocket of *Pa*HSS.

(A) *Cartoon representation of* Pa*HSS (PDB ID 6Y87, chain A) with the "NAD(P)-binding Rossmann-like" domain colored in yellow (residues 1-155 and 389-419) and the "HSS-like" domain in blue (residues 156-388 and 420-469). The solvent-accessible surface of the binding pocket is depicted in transparent red with the entrance pointing upwards. The NAD⁺ molecule lining the surface of the pocket is shown as ball-and-stick representation.* ***(B)*** *The solvent-accessible surface of the binding pocket was counter clock-wisely rotated by an angle of ~90° around the y-axis in relation to (A). Selected side chains lining the pocket surface, the NAD⁺ molecule and a PUT molecule within the active site are depicted as ball-and-stick representation.*

The catalytic triad is composed of the residues E294, H292 and E233. The "center amino site"/active site is situated between the indole ring plane of W225, the nicotinamide ring plane and residue H292. The PUT molecule is located with its "outer" amino group and atom C4 at the "center amino site"/active site and with the "inner" amino group near residue E206 at the "inner amino site". PUT molecules were detected at the active sites of *Pa*HSS molecules A, C and E as shown in Figure 26.

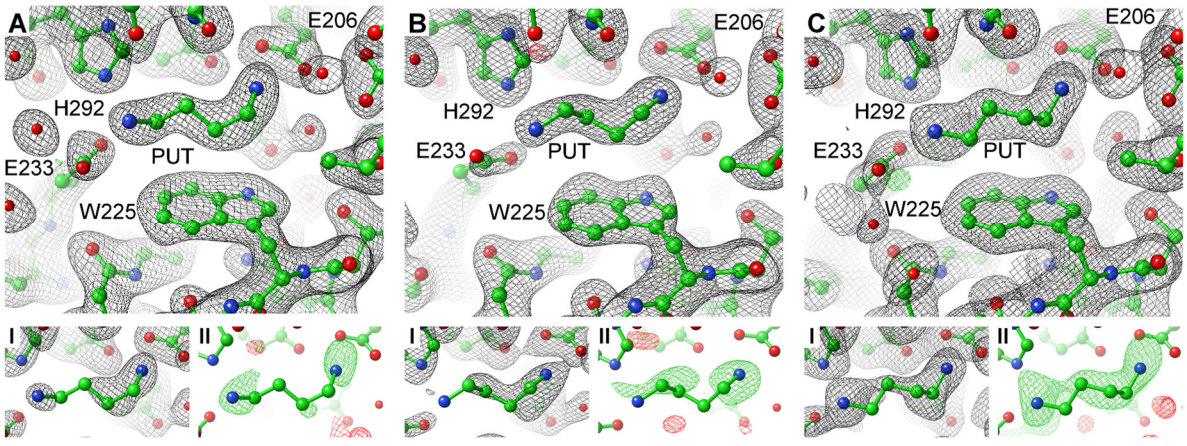

Figure 26: Active sites of three *Pa*HSS molecules with bound PUT molecules.

Atomic models of Pa*HSS molecules (PDB ID 6Y87, chain A* ***(A)****, chain C* ***(B)*** *and chain E* ***(C)****) are depicted as ball-and-stick representation and electron density maps as mesh. Large images (****A-C****) show the 2mFo-DFc map (1 σ, black) and mFo-DFc map (+/- 4 σ, green/red) of the complete models. Corresponding omit maps based on models lacking the respective PUT molecule are given in the smaller images below (****I:*** *2mFo-DFc, black, 1 σ;* ***II:*** *mFo-DFc, green/red, +/- 3 σ). Omit maps were calculated by the composite_omit_map program of Phenix after first omitting the respective PUT molecule followed by refinement including simulated annealing.*

The residues E206 and E233, providing the “amino sites”, together with residues H292 and W225 are visible in the depicted section of the active site. According to the omit maps, the PUT molecule in molecule E is most convincingly supported by electron density. Incomplete contouring of the other two PUT molecules by the respective omit maps might be caused by higher flexibility or lower occupancy of the respective PUT molecules. Both the architecture of the active sites and the location of the PUT molecules are very similar. The “inner” and “outer” amino groups of the PUT molecules are coordinated to the carboxyl oxygens of residues E206 and E233, respectively. Distances between 2.8-3.2 Å were measured, while the shortest distances are between the “inner” amino group and residue E206. The conformation of the three PUT carbon chains varies between the respective *Pa*HSS molecules. The exact tracing of the carbon chains might be complicated by their assumed flexibility and the relatively low resolution of the structure. At the active site of molecule D, only water molecules could be detected. At the active site of molecule F, the electron density distribution could not unambiguously be interpreted. Although the shape of the density hints at a PUT molecule, it did not support convincing fitting of such a molecule. The occupancy of the PUT molecule in this *Pa*HSS molecule could be too low or its flexibility too high to provide an interpretable electron density. In the *Pa*HSS molecule B, a unique density distribution is present as depicted in Figure 27 from two points of view.

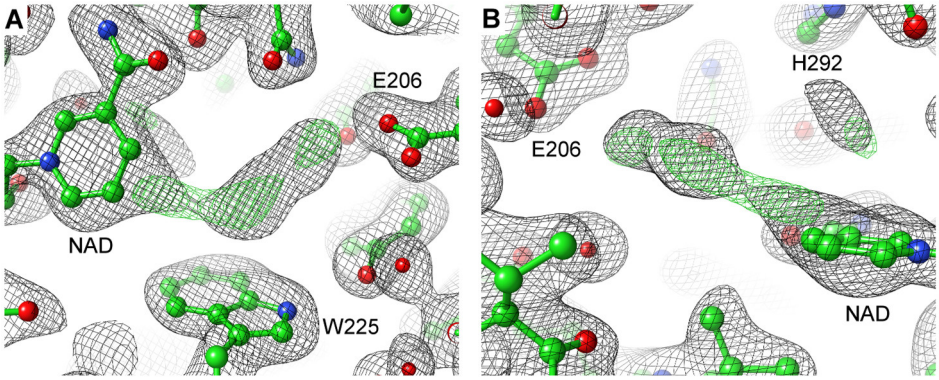

Figure 27: Active site of a *Pa*HSS molecule with a potential NAD⁺ adduct.
The atomic model of the Pa*HSS molecule (PDB ID 6Y87, chain B) is depicted as ball-and-stick representation in two orientations in* ***(A)*** *and* ***(B)*** *with electron density maps as mesh. The contouring was set to 1 σ for the 2mFo-DFc map (black) and to +/- 4 σ for the mFo-DFc map (green/red). The central electron density distribution could originate from a substitution at the nicotinamide ring (adduct formation) but was not interpreted by model atoms.*

A longitudinal density both in the 2mFo-DFc map and in the mFo-DFc map reaches from the proximity of side chain E206 to the bond between atoms C4N and C5N of the nicotinamide ring. Close inspection of the 2mFo-DFc map reveals a distortion of electron density distribution contouring the nicotinamide ring, hinting at a non-planar geometry of the ring structure. This could be interpreted as a covalent nicotinamide adduct occurring as intermediate in the reaction mechanism. NAD adducts were previously described in different enzymes (chapter 4.3, p. 80). Not knowing the definite composition of the potential adduct and relying on a moderate resolution, the density in the *Pa*HSS molecule B was not interpreted. In the wt *Bv*HSS structure (PDB ID 4TVB, chain A), an HSP molecule was modeled into the active site (Krossa et al. 2016). In this structure, the HSP C05 atom (former PUT C4 atom) approaches the NAD⁺ C4N atom from “above” the NAD⁺ ring plane up to merely 2.1 Å. The proximity

of both atoms was interpreted as hydride transfer from NADH C4N to the oxidized HSP C05 atom. The orientation of the proposed (partial) bond between C4N and C05, defined by the connecting electron density, thereby suggests a tetrahedral geometry and thus sp^3 hybridization of carbon C4N. In contrast to this situation, the uninterpreted electron density distribution in the *Pa*HSS molecule B rather laterally overlaps with the density of the NAD^+ atoms C4N/C5N, neither perfectly matching a tetrahedral (sp^3 hybridization) nor trigonal geometry (sp^2 hybridization) of the respective nicotinamide carbon. Also, the uninterpreted density can only accommodate a smaller intermediate like an aminobutyl moiety. Further research is required to confirm the potential presence of such an intermediate covalently bound to the nicotinamide ring.

3.6.9 Structural comparison of PaHSS with B*v*HSS

The structural similarity between *Pa*HSS molecule A and *Bv*HSS subunit B (PDB ID 4TVB) was examined in a first approach by the tool “MatchMaker” implemented in UCSF Chimera 1.14. Global comparison of both molecules results in C_α RMSD of 0.89 Å for pruned C_α pairs (RMSD below 2 Å, 397 pairs) and 2.80 Å for all C_α pairs (464 pairs). These numbers indicate that a large portion of the two structures (397 C_α pairs) is in good agreement while the remaining portion (67 C_α pairs) is more divergent. In the structure-based sequence alignment depicted in Figure 28, only residues with C_α RMSD below 5 Å are aligned. It shows a sequence identity of ~44 % with both structures almost completely aligning to each other. The few and short gaps in the structural alignment are exclusively caused by solvent exposed parts of both structures, mostly loop regions. These parts are neither involved in the formation of the binding pocket nor in the coordination of the respective NAD^+ molecules. The only secondary structures deviating between the two structures are two α-helices of the Rossmann-like domain at the protein surface (*Pa*HSS helix residues 32-36 and 48-57; *Bv*HSS helix residues 37-39 and 47-57). These helices are partially misaligned (C_α RMSD > 5 Å) due to shifted locations and differing lengths. However, the Rossmann-like domains are in good agreement apart from these helices, including the relevant regions forming the binding pocket and coordinating the NAD^+ molecules. The locations of the relevant *Bv*HSS residues examined in this thesis (red frames) and of the residues forming the catalytic triad (blue frames) are conserved in the *Pa*HSS structure. For future referencing, it should be noted that the position of these residues is shifted by “-4” in the *Pa*HSS sequence compared to the *Bv*HSS sequence. Concluding, both *Bv*HSS and *Pa*HSS structures are very similar and share the same relevant residues involved in the reaction mechanism.

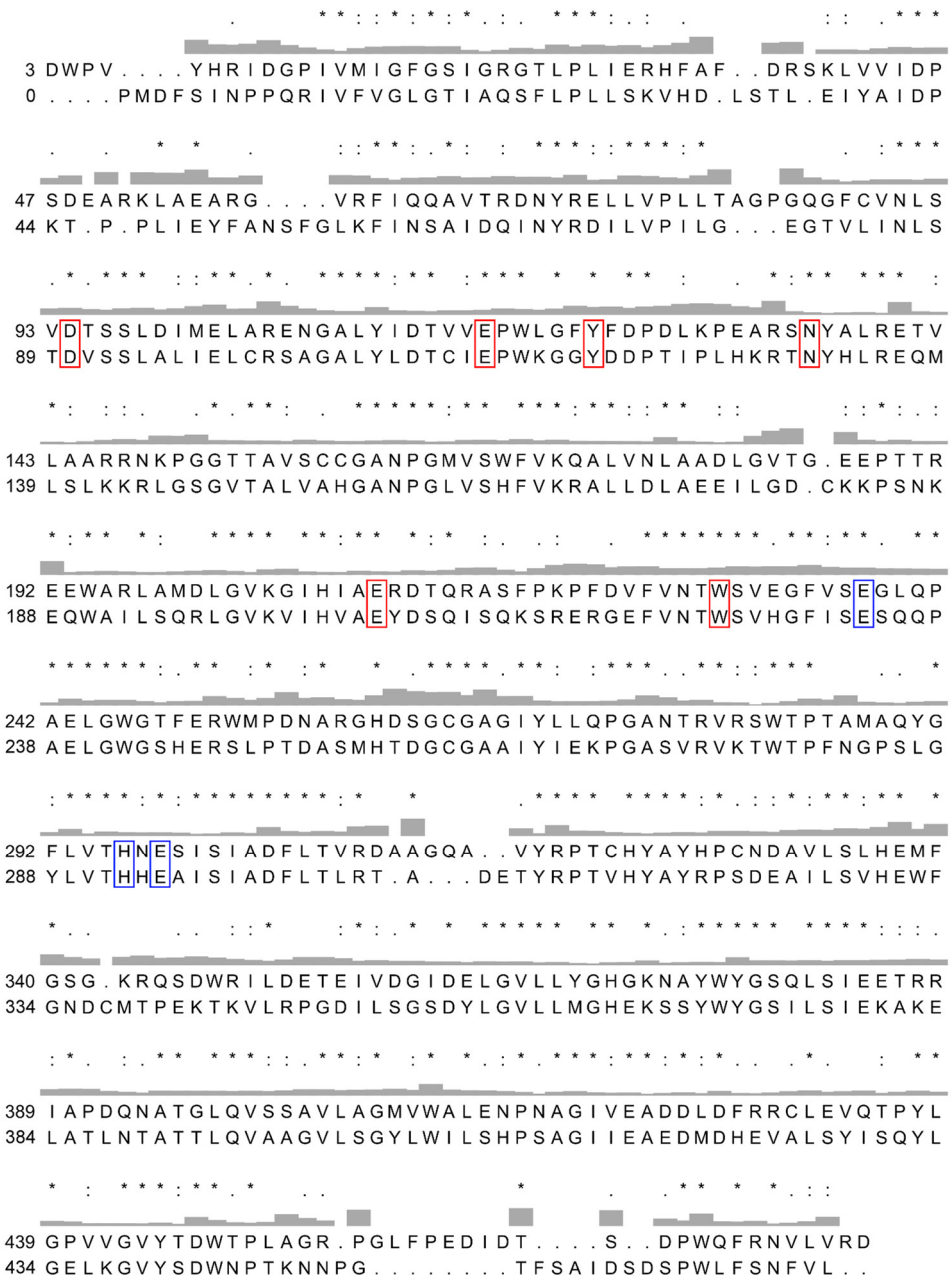

Figure 28: Structure-based sequence alignment of *Bv*HSS and *Pa*HSS.

The structures of Bv*HSS (upper sequence, PDB ID 4TVB, chain B) and* Pa*HSS (lower sequence, PDB ID 6Y87, chain A) were superimposed onto each other with the UCSF Chimera 1.14 "MatchMaker" tool, followed by structure-based sequence alignment with a C_α residue-residue distance cutoff of 5 Å. The numbers correspond to the amino acid sequences of the respective proteins. Residue number "0" of* Pa*HSS corresponds to the* N*-terminal proline, a leftover of the expression tag. Above the aligned sequences, conservation is depicted as Clustal symbols according to the PAM250 matrix (* = identical, : = high similarity, . = low similarity) and RMSD values between complete residues are given as histogram (highest value: 5.03 Å for T452(*Pa*HSS)/T464(*Bv*HSS)). The relevant residues exchanged within the respective* Bv*HSS variants (D94, E117, Y123, N135, E210 and W229) and corresponding* Pa*HSS residues are highlighted with red boxes, the catalytic triad composed of* Pa*HSS/*Bv*HSS residues E233/E237, H292/H296 and E294/E298 with blue ones.*

The superimposed structures of *Pa*HSS and *Bv*HSS are depicted in Figure 29 with focus on the volume and the relevant residues of the binding pocket.

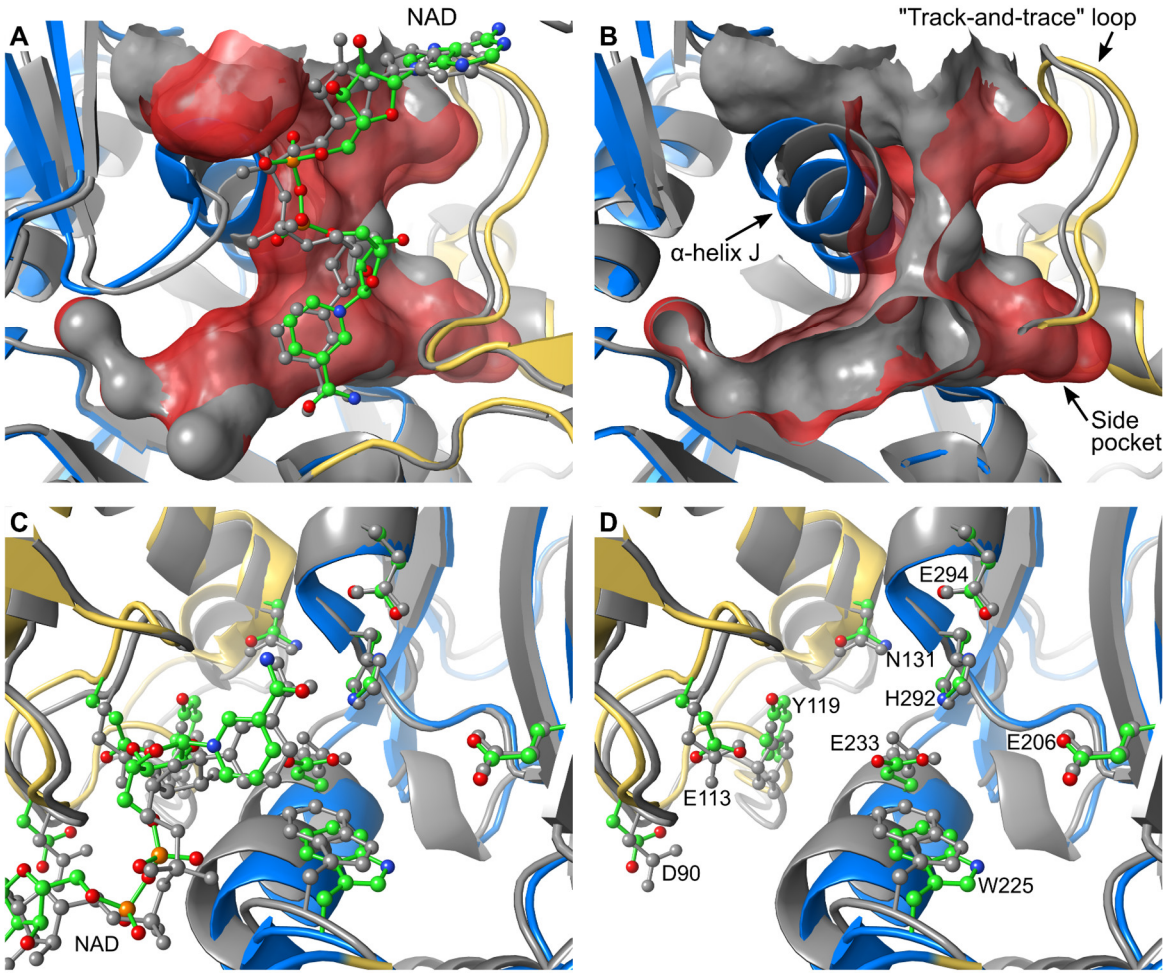

Figure 29: Comparison of the binding pockets of *Pa*HSS and *Bv*HSS.

The atomic models of Pa*HSS (PDB ID 6Y87, chain A) and* Bv*HSS (PDB ID 4TVB, chain B) were superimposed onto each other using the "MatchMaker" tool of UCSF Chimera 1.14. The models are depicted as cartoon representation with side chains of selected residues and NAD⁺ molecules shown as ball-and-stick. Bound PUT molecules are not shown (see Figure 26, Figure 31). The* Pa*HSS model and the surface of its solvent-accessible binding pocket is colored as in Figure 25, the model and surface of* Bv*HSS in grey. The numbering of the labeled side chains corresponds to the amino acid sequence of* Pa*HSS.* ***(A/B)*** *Overall comparison of binding pockets surrounded by respective α-helix J, "track-and-trace" loop and NAD⁺ molecule. In (B), the binding pocket surfaces were clipped and the NAD⁺ molecules were hidden for clarification.* ***(C/D)*** *Comparison of selected binding pocket residues with (C) and without (D) depiction of NAD⁺ molecules.*

In Figure 29A, the surfaces of the binding pockets are illustrated, surrounded by the respective "track-and-trace" loop, the α-helix J (*Pa*HSS residues 226-236, *Bv*HSS residues 230-240) and the NAD⁺ molecule. The NAD⁺ molecules similarly insert their nicotinamide rings into the active site of the binding pockets, albeit with a slight offset (RMSD 1.21 Å as determined by the PyMOL command "rms_cur"). In addition, both the α-helix J and the "track-and-trace" loop of *Pa*HSS are shifted, providing more space for the pocket entrance and the below tunnel leading into the active site. This effect becomes more obvious in Figure 29B, showing the interior of the clipped binding pockets. The *Pa*HSS entrance tunnel is significantly broader due to the shift of the α-helix J. The "bottom" of the

binding pocket, containing the active site, is barely affected by this shift and provides comparable space in both structures. The side pocket of *Pa*HSS is slightly enlarged by the shift of the “track-and-trace” loop and mainly due to movement of residue I112 (not shown).

In Figure 29C/D, the interiors of the superimposed binding pockets are depicted with focus on relevant side chains. These side chains are numbered according to the *Pa*HSS sequence and drawn as ball-and-stick representation, same as the NAD^+ molecules. The remaining structures are shown as cartoon representation for simplicity. In Figure 29D, the NAD^+ molecules are hidden to uncover all relevant residues. From this point of view, the entrance tunnel including residues D90, E113 and Y119 is situated at the bottom left corner of the images. The active site with residue W225 and the catalytic triad (E233, H292, E294) is located in the middle. The site pocket containing residue N131 is at the back and the “inner amino site” represented by E206 at the right. In general, the *Pa*HSS and *Bv*HSS side chains align with good agreement, albeit not to the same degree. Side chains E206, H292 and E294 align almost perfectly. Minor deviations are visible for side chains N131 and E233. Although residue E233 is thereby part of the α-helix J, which is significantly displaced in the *Pa*HSS structure, the carboxyl groups are still very similarly placed in both *Pa*HSS and *Bv*HSS structures. Residue W225 belongs to a short loop region directly preceding α-helix J and is also affected by its shift. Apart from a little offset comparing both residues, the indole rings are equally oriented and parallel to each other (see Figure 31 for more details). The same principle is true for the NAD^+ molecules. These adopt highly similar conformations but are shifted with respect to one another (nicotinamide ring centroid distance 0.8 Å). Still, the nicotinamide rings align in the same plane. While residues E113 and Y119 belong to the shifted “track-and-trace” loop, residue D90 is part of another slightly displaced loop. Again, residues D90 and Y119 exhibit a certain offset but retain highly similar conformations. Residue E113 adopts a different conformation in the *Pa*HSS molecule A compared to the *Bv*HSS residue E117. Still, both carboxyl groups are placed at similar locations. In summary, the architecture of both binding pockets and especially the orientation of relevant side chains are highly similar in both *Pa*HSS and *Bv*HSS structures. Except for some minor deviations, the most significant difference in the *Pa*HSS structure is the broader entrance tunnel of the binding pocket.

The exact dimensions of the entrance tunnels of *Pa*HSS and *Bv*HSS are examined in Figure 30A/B. The entrance is seen from “above” with a view into the interior of the binding pocket. Only parts of the structures involved in the formation of the entrance tunnels are shown together with the surface of the binding pockets. The entrance tunnel dimensions are quantified by indicated distance measurements. In principle, the *Pa*HSS tunnel entrance is confined from four sides. From this point of view, the α-helix J forms the bottom border (residues S232, G229 and S226), residue Y119 as part of the “track-and-trace” loop the left and the phosphate groups of NAD^+ the right. The top border is composed of the residues D90 and E113 as “ionic slide” together with T89 and the ribose moiety attached to the nicotinamide ring. The *Pa*HSS opening preceding the entrance tunnel is relatively large with maximal dimensions of 4.7 x 8.6 Å measured in the same plane. However, the below entrance tunnel constricts from 4.7 Å to maximally 3.5 Å.

As discussed above, the α-helix J in the *Bv*HSS structure provides less space for the entrance tunnel compared to the *Pa*HSS structure. As result, the *Bv*HSS entrance tunnel is formed in a rather triangular fashion.

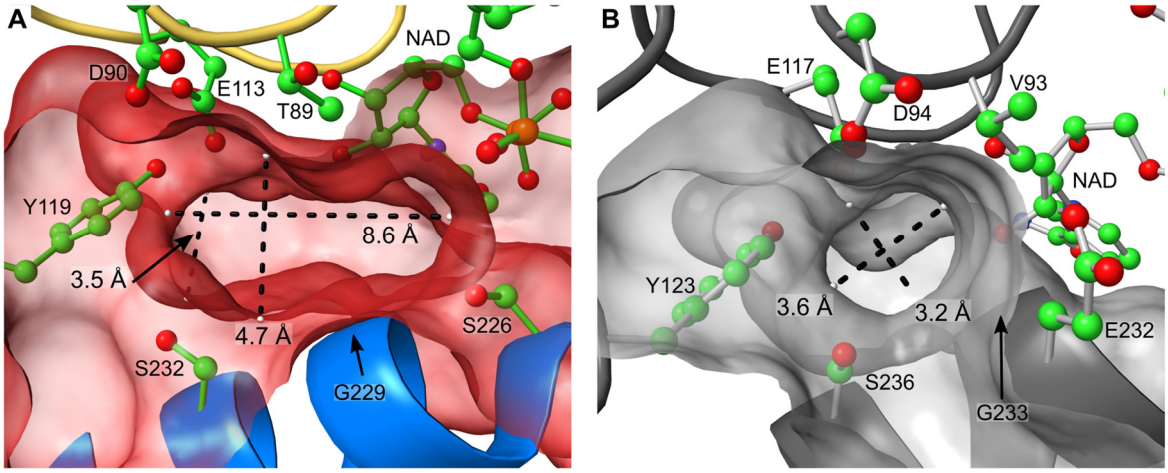

Figure 30: Dimensions of the binding pocket entrance of *Pa*HSS and *Bv*HSS.

The models are depicted as cartoon representation with side chains of selected residues and NAD⁺ molecules shown as ball-and-stick. For clarification, only side chains lining the upper entrance tunnel of the binding pockets are given as ball-and-stick representation. The surfaces of the solvent-accessible binding pockets were rendered transparent. Distances were measured with the program PyMOL and illustrated by dashed lines connecting white spheres at the surface of the binding pockets. The locations of the residues G229 and G233, which are implicit in the cartoon representation due to absence of a side chain, are indicated by arrows. ***(A)*** *PaHSS (PDB ID 6Y87, chain A, colors as in Figure 25), the upper entrance dimensions (4.7 Å x 8.6 Å) were measured in the same plane and the tunnel narrowing (to a maximum of 3.5 Å) further below.* ***(B)*** *BvHSS (PDB ID 4TVB, chain B), the distances were measured in the same plane.*

Referring to the perspective of Figure 30B, the α-helix J thereby confines both the bottom (residue S236 and G233) and the right side (residue E232) of the entrance tunnel. Residue Y123 borders the left side and residues D94, E117 and V93 (superimposes with *Pa*HSS T89) the top side. The phosphate groups of the NAD⁺ molecule do not contribute to the tunnel surface in the *Bv*HSS structure. As result, the *Bv*HSS pocket entrance has narrower dimensions of 3.2 x 3.6 Å as determined in the same plane. Concluding, the *Pa*HSS structure exhibits a rather funnel-like pocket entrance and the *Bv*HSS a pore-like entrance. However, the *Pa*HSS entrance confines on its way into the binding pocket to similar dimensions as the *Bv*HSS pore. Similar steric restrictions should therefore apply for the access of compounds into the active sites of both structures.

3.6.10 Cation-π interaction geometry in Pa*HSS and* Bv*HSS*

The superimposition of relevant *Pa*HSS and *Bv*HSS residues and of the nicotinamide rings was discussed above (Figure 29C/D). While most of the active site residues are in nearly perfect alignment, moderate structural deviations are present for the nicotinamide rings and the tryptophan indole rings.

The nicotinamide rings lie in the same plane but are slightly shifted. Comparing the *Pa*HSS (PDB ID 6Y87, chain E) and *Bv*HSS (PDB ID 4TVB, chain B) structures with bound PUT molecules, the distance between PUT C4 and NAD⁺ C4N is 2.2 Å for the *Bv*HSS and 3.4 Å for the *Pa*HSS. The longer distance in the *Pa*HSS would suggest less efficient hydride transfer. However, the location of PUT C4 differs between the different PUT-containing molecules within the asymmetric unit. *Pa*HSS molecule E was chosen for the distance measurements, since the bound PUT molecule is most

strongly supported by electron density and exhibits the most similar conformation compared to the PUT molecule in the *Bv*HSS. Still, a certain flexibility of the PUT carbon chain and movement during the reaction mechanism can be assumed. An effect of the nicotinamide ring shift on the respective enzyme activities is therefore hard to predict.

The geometric relations between the PUT molecules and tryptophan indole rings in the *Pa*HSS and *Bv*HSS structures are depicted in Figure 31. These relations allow to estimate the strength of the cation-π interaction in both structures. Again, *Pa*HSS molecule E was chosen for this comparison due to its most reliable conformation of the contained PUT molecule.

Before evaluating the cation-π interaction geometries in both structures, geometric requirements for this interaction type are recapitulated in the following. Numerous studies have calculated cation-π interaction energies between various interaction partners based on quantum mechanical computations (Mahadevi and Sastry 2013). Often, these studies exclusively consider the optimal interaction geometry by placing the cation perpendicularly above the aromatic ring centroid at a θ-angle of 0° (angles θ and φ are explained in Figure 31). However, such an optimal interaction is not necessarily possible in the context of steric constraints in biological structures. In fact, examination of (proposed) cation-π interactions in PDB-deposited protein structures revealed numerous examples of non-optimal geometries. One study inspected the distances between positively charged amino groups of protein side chains and ring centroids of aromatic side chains. Amino groups were preferentially placed within 3.4-6 Å (maximal occupancy at 4.75 Å) of the centroids at a θ-angle of 30-40° (Burley and Petsko 1986). Another study correlated the distance between the amino group of lysine side chains and the ring centroids of phenylalanine residues to the angle θ (Chipot et al. 1996). This situation more closely applies to the cation-π interaction in this thesis, since the side chain of lysine is a structural analogue of PUT. While small θ-angles of maximally 10° were associated with short centroid-amino group distances around 3 Å, larger angles of 40° occurred with longer distances around ~5 Å. The correlation of larger θ-angles with longer centroid-amino group distances in protein structures was also shown in another study for lysine and tryptophan as interaction partners (Minoux and Chipot 1999).

The previously reported interaction partners may not perfectly apply to the cation-π interaction presented in this thesis. Protein residues including their side chains are more sterically restrained within the protein main chain in contrast to a non-covalently bound PUT molecule. However, these studies demonstrate the presence of non-optimal cation-π interaction geometries between amino groups and aromatic side chains in protein structures. This was further supported by quantum mechanical computations, which specifically calculated binding energies of an ammonium ion (and other cations) to benzene at non-optimal geometries (Marshall et al. 2009). Maximal binding energies were determined for an optimal θ-angle of 0°. Although increase of the θ-angle decreased the binding energy, up to 30 % of the maximal energy could still be determined at a θ-angle of 90° (side-on geometry). In addition, the influence of angle φ increased with larger θ-angles. A φ-angle of 30° thereby represents optimal positioning of the cation between two ring hydrogens (refer to the orthogonal projection of the cation onto the ring plane). A φ-angle of 30° was energetically favored compared to a φ-angle of 0°, the latter meaning coincidence of a ring carbon (and its respective ring hydrogen) with the orthogonal projection of the cation onto the ring plane.

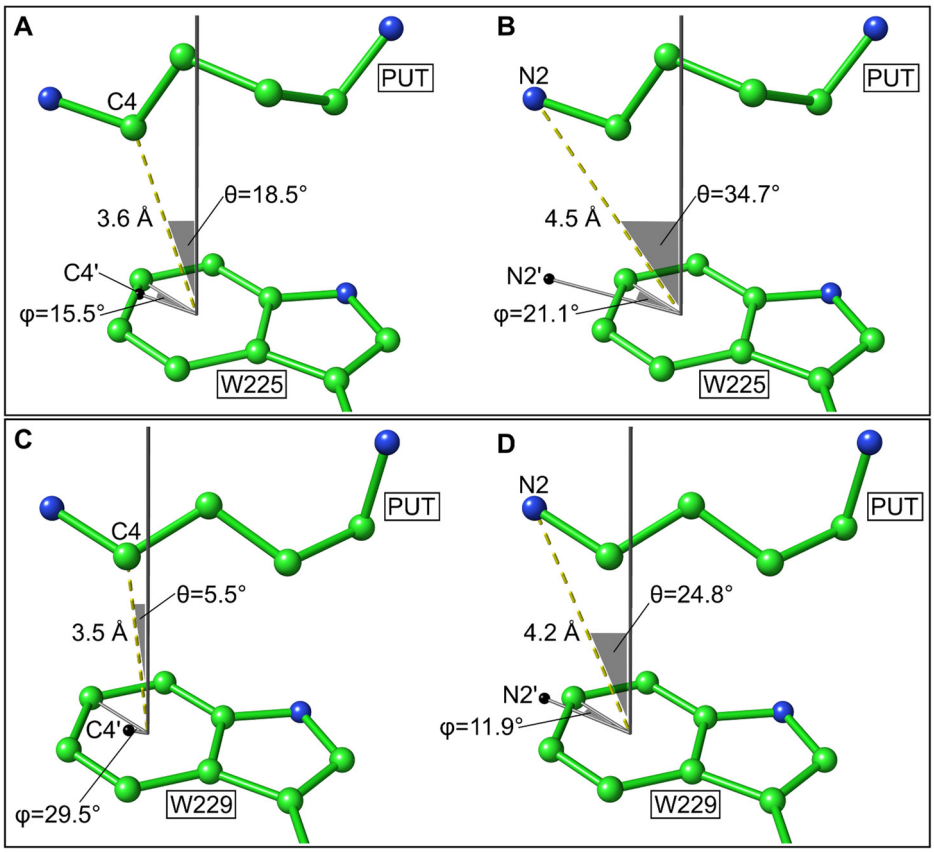

Figure 31: Geometry of cation-π interaction between PUT and tryptophan in *Pa*HSS and *Bv*HSS.
Interaction geometry between the PUT atoms C4 and N2 and the tryptophan benzene moiety in ***(A/B)*** Pa*HSS (PDB ID 6Y87, chain E) and* ***(C/D)*** Bv*HSS (PDB ID 4TVB, chain B). Structures are given as ball-and-stick representation, distances as yellow dashed lines, additional angle legs as grey lines and angles as grey transparent triangles (not visible for φ in (C)). The orthogonal projections of C4 and N2 onto the ring planes are shown as black spheres (C4' and N2'). All angle legs originate from the centroid of the benzene moiety, including the dashed distance vectors from the centroid to C4 and N2. Angle θ is spanned by the vector orthogonal to the ring plane (grey, infinitely pointing upwards) and the C4 or N2 distance vector (yellow, dashed). Angle φ is between the vector pointing to C4' or N2' and the vector pointing to ring carbon CH2.*

As rule of thumb, the strength of the cation-π interaction between the respective PUT atoms and the benzene moiety of tryptophan should increase with (I) decreasing centroid-cation distance, (II) decreasing θ-angle (maximum at 0°) and (III) increasing φ-angle (maximum at 30°). The φ-angle, however, only exerts a minor effect on the binding energy at large θ-angles (Marshall et al. 2009) and should be neglectable at the θ-angles below 35° occurring in this thesis.
The geometry between PUT C4 and the benzene moiety in the *Pa*HSS (molecule E) exhibits an atom-centroid distance of 3.6 Å, a θ-angle of 18.5° and a φ-angle of 15.5°. In the *Bv*HSS, the distance is 3.5 Å, the θ-angle 5.5° and the φ-angle 29.5°. For the proposed stabilization of a positive partial charge at PUT C4 during catalysis, the cation-π interaction geometry is almost optimal in the *Bv*HSS. A distance of 3.5 Å in combination with a small θ-angle approaches optimal orthogonal positioning of the C4 atom above the ring centroid. The C4-centroid distance in the *Pa*HSS is very similar, but the θ-angle provides a less favored geometry. Although the geometry in the *Pa*HSS should allow significant cation-π interaction between C4 and the benzene moiety, the binding strength should consistently be higher in the *Bv*HSS. In this context, the PUT C4 in *Pa*HSS molecule E adopts the most favored

cation-π interaction geometry compared to the C4 atoms in the *Pa*HSS molecules A and C. It should be noted, that the PUT structures should represent regularly bound PUT molecules and not carbocation intermediates. As result, the depicted C4 atoms should not participate in significant cation-π interactions at this state. This would explain a certain flexibility of the PUT carbon chain and different locations for the C4 atoms in the respective *Pa*HSS molecules.

The PUT N2 atom should be positively charged at physiological pH as primary ammonium ion, allowing constant cation-π interaction with the benzene moiety of the tryptophan. Consistently, the N2 atoms are similarly located in the *Bv*HSS and the three *Pa*HSS molecules containing bound PUT molecules. In the *Pa*HSS, the N2-centroid distance is 4.5 Å at a θ-angle of 34.7° and a φ-angle of 21.1°. In the *Bv*HSS, the distance amounts to 4.2 Å with a θ-angle of 24.8° and a φ-angle of 11.9°. Both geometries satisfy the prerequisites for efficient cation-π interaction. Again, the cation-π interaction should be stronger in the *Bv*HSS due to a smaller cation-centroid distance and a smaller θ-angle. In general, the combinations of cation-centroid distances and θ-angles for atoms C4 and N2 of PUT are in good agreement with geometries previously found in protein structures as discussed above.

In this thesis, the activity of the *Pa*HSS was roughly a third of the *Bv*HSS at the same assay conditions (Table 7, p.48). The reason for this difference cannot be proven without additional experiments at this point. Differences between both proteins were discussed including the reduced stability of the *Pa*HSS, different oligomerization states, deviating dimensions of the binding pocket entrances and slightly shifted nicotinamide rings. The less optimal geometric prerequisites in the *Pa*HSS for cation-π interactions between PUT C4/N2 and the benzene moiety of residue W225 could be another reason. The major importance of a functional and strong cation-π interaction is highly suggested by the drastically reduced or even impaired activity of the *Bv*HSS W229 variants. Exchange of W229 for phenylalanine or tyrosine, both providing a smaller π-system with less negative electrostatic potential, retained only little activity. Concluding, the activity of the *Bv*HSS seems to strongly correlate with the strength of the cation-π interaction. This correlation between cation-π interaction strength and protein function has previously been shown in other proteins by exchange of the involved aromatic residues, e.g. for the nicotinic receptor (Zhong et al. 1998), terpenoid cyclases (Morikubo et al. 2006; Faraldos et al. 2011; Aiba et al. 2018) and retinoid isomerohydrolase (Redmond et al. 2010). Concluding, the inferior cation-π interaction geometry in the *Pa*HSS compared to the *Bv*HSS could attribute for its reduced activity.

4 Summary and Outlook

4.1 Summary

This thesis deepens the understanding of the reaction mechanism harnessed by the bacterial HSS. Introduction of single residue mutations into the *Bv*HSS allowed to evaluate the role of critical residues based on activity assays and X-ray structures. This knowledge could be transferred to the *Pa*HSS after solving its X-ray structure for the first time.

The main findings are summarized in the following, referring to the *Bv*HSS residue numbering. The residues D94 and E117, providing the “ionic slide” into the binding pocket, were shown to promote efficient HSP production. The degree of changing the acidic character of the residues to neutral or even basic character correlated with decreasing variant activity. Residue E117 thereby was more important for the enzyme function than residue D94. The negative charge provided by residue E210 at the “inner amino site” was essential for catalysis, not tolerating any modification. The different variants targeting residue W229 strongly support the role of the W229 indole ring as cation-π interaction partner for positively charged reaction components. Exchange for a phenylalanine or tyrosine residue merely retained little activity, replacement by histidine, glutamate, lysine and alanine caused complete inactivity of the variants. Potential roles of the “track-and-trace” loop (containing residue Y123) and the side pocket (containing residues V116 and N135) remain to be elucidated. The essential role of the catalytic triad (E237, H296, E298) was previously described (Krossa et al. 2016). Relevant structural differences of the *Pa*HSS compared to the *Bv*HSS were limited to a larger entrance into the binding pocket and a less favorable cation-π interaction geometry. In the following, approaches for future research on the *Pa*HSS are proposed.

4.2 Cation-π interaction

The results inferred from the *Bv*HSS W229 variants clearly suggest a major dependency on strong cation-π interaction for catalysis. However, the experiments given in this thesis do not provide definite “proof” for such a cation-π interaction. Another explanation could be the requirement for the bulky indole moiety of W229 for steric restriction of reaction components to a defined location within the active site. This could e.g. be needed to decrease the flexibility of reaction components and to facilitate hydride transfer to and from the nicotinamide ring by optimal positioning of respective reaction components. In fact, studies on the β-amyrin synthase have previously distinguished specific aromatic residues for cation-π interaction (Ito et al. 2013; Ito et al. 2017; Aiba et al. 2018) and others merely for steric “placeholding” (Ito et al. 2014; Ito et al. 2017). However, these studies rely on comparison of the product distribution ratio of single residue variants without evaluation of corresponding structures. To unambiguously “prove” the cation-π interaction in the bacterial HSS, tryptophan derivatives with very similar van der Waals radii as native tryptophan need to be incorporated. This can be achieved with the “fluorination strategy” (Davis and Dougherty 2015), which entails replacement of relevant aromatic residues with fluorinated derivatives. The electron-withdrawing fluorine was calculated by quantum mechanical methods to decrease the cation-π interaction energy with progressive fluorine substitution at the ring system. Exchange of aromatic residues involved in cation-π interaction for such derivatives consistently correlated with decreasing

protein function in several studies (Zhong et al. 1998; Beene et al. 2002; Torrice et al. 2009; Xiu et al. 2009; Pless et al. 2011). In addition, a gain-of-function variant of the HSS could be designed by either incorporating a larger π-system than the indole ring or by adding electron-donating substituents to the ring. This approach might be challenging since the indole ring already provides a comparably negative electrostatic potential. Larger π-systems or electron-donating substituents capable of significantly increasing this potential might cause steric issues in the confined active site.

A completely different strategy to detect cation-π interactions might be provided by spectroscopic techniques. By laser-induced optoacoustic spectroscopy (LIOAS), molecules (presumably) exhibiting tryptophan-mediated cation-π interaction were demonstrated to absorb at 532 nm (Roveri et al. 1990; Roveri and Braslavsky 2012). Absorption was confirmed for aqueous tryptophan with HCl (5 N), copolymers containing tryptophan and basic amino acids (lysine, arginine, ornithine) and for proteins including bovine and human serum albumin. Different molar absorption coefficients were thereby proposed to reflect the strength of cation-π interactions. Recently, “regular” spectroscopy in the visible range of the spectrum was used to attribute spectral properties of molecules to indole-based cation-π interactions (Juszczak and Eisenberg 2017). The examined molecules were indole (titrated with NH_4OH or NaOH), tryptophan-containing dipeptides and human serum albumin. In general, absorption peaks between ~460-470 nm and at ~500 nm together with fluorescence emission between ~500-520 nm were detected depending on the aqueous sample. Glycerol was thereby added to the protein sample to roughly match the refractive indices of the sample buffer and the protein. Light scattering by the protein was minimized this way, which otherwise interferes with detection of the weak cation-π-induced absorption. Unique spectral properties including different wavelengths for absorption and fluorescence emission, varying extinction coefficients as well as quantum yields were again proposed to correlate with respective characteristics of the cation-π interactions. Still, the mentioned findings are limited to a few examples and were not quantitatively evaluated for different proteins and cation-π interactions. Signals were assumed to quantitatively depend on the cationic partner and the interaction geometry, but limits of detection were not systematically tested so far. In addition, the proposed cation-π interactions in the HSS are not “stable” but form and break constantly between the indole ring and reaction components and/or transition states. Time-resolved detection of these interactions would consequently require LIOAS instead of regular spectrophotometry.

4.3 Potential NAD^+ adduct

The electron density distribution in *Pa*HSS molecule B revealed a longitudinal density reaching from the “inner amino site” (near residue E206) to the bond between the NAD^+ atoms C4N and C5N. The size and location of this density distinctly distinguishes it from the electron density distribution interpreted as HSP molecule in the *Bv*HSS (Krossa et al. 2016). Considering its overlap with the nicotinamide ring density, this finding strongly suggests an adduct formation between a PUT molecule and the nicotinamide ring. The geometry between the longitudinal uninterpreted density and the nicotinamide ring plane resembles a transition between a side-on geometry (sp^2 hybridization) and a tetrahedral geometry (sp^3 hybridization) of the nicotinamide ring carbon, not clearly matching any of them. Regarding the small size of the uninterpreted electron density and in context of the proposed reaction mechanism, only a 1-aminobutane would fit into the density but not a PUT or a 4-

aminobutanal. The amino group of the 1-aminobutane would be coordinated to residue E206 and the terminal carbon atom covalently bound to carbon C4N or C5N of the nicotinamide ring. This would require adduct formation after deamination of PUT. The formed adduct could be an intermediate "waiting" for a second PUT molecule and subsequent HSP formation. The necessary mechanism for formation of such an adduct remains elusive at this point. Also, unambiguous interpretation of the electron density distribution is not possible without additional experiments due to the limited resolution of the structure.

In general, various molecules have already been reported to form adducts with the nicotinamide ring of NAD(P) via atom C2N or C4N. These include inhibitory compounds like ketones and pyrazole in alcohol dehydrogenase (Becker and Roberts 1984; Benach et al. 1999; Rubach and Plapp 2003), finasteride in human steroid 5α-reductase (Bull et al. 1996), 5-hydroxy-4-oxonorvaline in homoserine dehydrogenase (Jacques et al. 2003) and sanguinarine (Sandor et al. 2018), which is nonenzymatically reduced by NADH via a covalent adduct. Not limited to inhibitors, adducts were also shown as regular intermediates during catalysis for glycerol-3-phosphate dehydrogenase (Choe et al. 2003), for lactate dehydrogenase at high pyruvate concentrations (Gutfreund et al. 1968; Everse et al. 1971), for enoyl-thioester reductases (Rosenthal et al. 2015; Vögeli et al. 2018) and crotonyl-CoA carboxylase/reductase (Rosenthal et al. 2014). A unique situation was found in the crystal structure of the C-terminal domain of 10-formyltetrahydrofolate dehydrogenase. One alternate conformation of a cysteine residue in the active site was reported to form a covalent bond between its sulfur atom and atom C4N of the $NADP^+$ nicotinamide ring (Tsybovsky Y et al. 2007). The authors also mentioned a similar (until then unnoticed) situation in the structure of a glyceraldehyde-3-phosphate dehydrogenase (Pohl et al. 2002).

A multitude of methods was applied to confirm and characterize the mentioned adducts in the above cited publications. These methods represent possible approaches to demonstrate adduct formation in the *Pa*HSS (and possibly also in the *Bv*HSS) and are briefly summarized in the following. In several cases, adducts formed via atom C4N of the nicotinamide rings were detected in crystal structures (PDB IDs listed above). The bonds between atom C4N and the added molecules thereby exhibit lengths between 1.5-1.7 Å. The orientation of these bonds together with the distorted electron density distributions of the nicotinamide rings reflects a (partial) tetrahedral geometry at C4N and consistently a non-planar ring conformation. The geometry of such a nicotinamide ring adduct could most accurately be determined at almost atomic resolution for two NAD^+-pyrazole adducts in the alcohol dehydrogenase (Rubach and Plapp 2003). These geometries were inferred to represent a boat conformation of the nicotinamide ring with single bonds between C3N-C4N and C4N-C5N.

Apart from X-ray crystallography, NAD(P) adducts were detected and characterized via spectrophotometry, NMR spectroscopy and mass spectrometry. If possible, adducts were purified by HPLC with half-lives between several minutes to days, depending on the adduct and its experimental treatment (Everse et al. 1971; Becker and Roberts 1984; Bull et al. 1996; Rosenthal et al. 2014). Depending on the identity and bonding site (C2N/C4N) of the added moiety, NAD(P) adducts exhibited characteristic absorbance peaks at ~320-330 nm for C4N adducts and ~370 nm for C2N adducts (Gutfreund et al. 1968; Everse et al. 1971; Bull et al. 1996; Jacques et al. 2003; Tsybovsky Y et al. 2007; Rosenthal et al. 2014; Rosenthal et al. 2015). Protein fluorescence was shown to be quenched

by the adducts (Gutfreund et al. 1968; Everse et al. 1971). NMR spectroscopy was performed with native adduct-forming molecules or with isotopically labeled ones. Integrating the ^{1}H-NMR peaks of the involved molecules even allowed to observe the time-resolved formation and further conversion of the adduct during catalysis (Rosenthal et al. 2014; Rosenthal et al. 2015). NMR spectroscopy of ^{13}C-labeled NAD^+ enabled to confirm the change of hybridization of the nicotinamide atom C4N from sp^2 to sp^3 (Jacques et al. 2003).

Concluding, unambiguous detection and chemical characterization of NAD(P) adducts is in principle possible via various methods. Before choosing the appropriate method for the detection of such an adduct, one should always consider its lifetime as "window of detection". Adducts formed by inhibitors are "stable" dead-end products. Adducts occurring as catalytic intermediates, as would be the case for the *Pa*HSS, are harder to detect due to direct conversion into products. Analysis of such short-lived adducts was previously done via stopped-flow techniques, at low temperatures to decrease the conversion rate or with enzyme variants unable to further convert the intermediate adduct (Rosenthal et al. 2014). The reaction rate of the *Pa*HSS can easily be adjusted by the temperature and was also significantly reduced by single residue mutations. If a PaHSS variant can be produced which is unable to further convert the proposed NAD^+ adduct, cannot be predicted. Another challenge in case of the HSS is the presumably stable, albeit non-covalent binding of the NAD^+ molecule as prosthetic group. An isolation of the proposed adduct would consistently be quite complicated.

4.4 *Pa*HSS as potential antibiotic target

Polyamine (PA) biosynthesis and uptake pathways in *P. aeruginosa* were presented in chapter 1.6 (p. 8). Studies on endogenous PA function and effects of exogenously applied PAs were summarized in chapter 1.7 (p. 10). Although PA research remains complicated and incomplete, several medically relevant roles of PAs were found in *P. aeruginosa*. In short, PAs were demonstrated to influence the susceptibility to different antibiotics, the virulence and the biofilm formation. However, the role of HSP in *P. aeruginosa* was not examined so far. HSP does not seem to be essential for growth since the lab strain PAO1 completely lacks the *Pa*HSS gene. However, the presence of the *Pa*HSS in more virulent strains like PA7 and PA14 might be caused by its role in pathogenicity. Inhibition of the *Pa*HSS in combination with other therapies might therefore improve the chances of recovery from a *Pseudomonas* infection. To elucidate this question, genetically engineered strains lacking and expressing *Pa*HSS could be compared in terms of growth, biofilm formation and antibiotic susceptibility, among others. Therefore, the *Pa*HSS gene could either be introduced into a PAO1 strain or removed from PA7/PA14 strains. Independent of its function in *P. aeruginosa*, the bacterial HSS is also present in other pathogenic bacteria including *L. pneumophila* and *Brucella* spp. (Shaw et al. 2010). Concluding, the findings presented in this thesis are not limited to *Bv*HSS and *Pa*HSS but might also be transferred to the HSS of other pathogenic bacteria.

The following structural premises might facilitate an *in silico* drug design targeting the active site of the *Pa*HSS. The dimensions of the entrance tunnel together with the acidic character of the residues attracting and coordinating substrates at the active site ("ionic slide", "amino sites") impose strict structural requirements on potential inhibitors. Access to the active site will mainly be restricted to small linear molecules with adequately distanced basic groups. This is also reflected by the tolerated

substrates of the *Pa*HSS (PUT, SPD and diamines of certain lengths, 1.3, p. 3) and the solely known competitive inhibitor DAP. An inhibitor would consistently need to mimic a reaction component of the *Pa*HSS. However, such an inhibitor could pose severe risks to patients by interference with e. g. the human DHS and SPD synthase.

A unique feature found in the *Pa*HSS could be exploited to circumvent this complication. The *Pa*HSS harbors a cysteine residue (C111) within the binding pocket between the active site and the side pocket. Its sulfur atom is positioned at the pocket surface between residue E113 (part of the "ionic slide") and oxygen O2D of NAD^+ (part of the "outer amino site"). Shuttling reaction components need to pass this cysteine residue when entering and leaving the active site. Even more, the "outer" amino group of a second PUT molecule or of a produced HSP molecule comes in close proximity to the sulfur atom. These are favorable prerequisites for design of a targeted covalent inhibitor (TCI) (Lonsdale and Ward 2018). TCIs are composed of (I) a highly selective, reversibly associating "binding group" to target the enzyme of interest combined with (II) a "functional group" for covalent bonding with the target. The reactivity of the "functional group" can be adjusted by selection of an appropriate moiety and should generally be low. Covalent bonding should only succeed after strong and selective binding via the "binding group", decreasing the number of inappropriately bound off-targets. In our case, the selective "binding group" could simply be a PUT molecule for targeting to the active site of the *Pa*HSS. The "functional group" could be an acrylamide group (e.g. directly connected to one amino group of PUT) which is capable of covalent bonding to the thiol side chain of C111 (Lonsdale and Ward 2018). Considering the most obvious off-targets when using such an TCI, the human DHS (PDB ID 6XXM) does not exhibit a cysteine residue in or near its binding pocket (Wątor et al. 2020). Covalent bonding of a TCI to the DHS would consistently not be possible. The PUT binding site of the human SPD synthase (PDB ID 2O06) does not contain a cysteine residue either (Wu et al. 2007). However, access to the binding site is regulated by a flexible "gate-keeping loop". Considering a large opening of the binding pocket, an inhibitor might come into contact with a cysteine residue near the opening (C25). In addition, the SPD synthase forms a side pocket for the accommodation of the aminopropyl group of the product SPD, provided by dcSAM (PDB ID 2O07). Another cysteine residue (C71) is located in this side pocket and could possibly interact with an inhibitor. Still, initial non-covalent binding of an adequately designed TCI should be far more favorable at the active site of the *Pa*HSS than near the mentioned cysteine residues in the SPD synthase. It should be kept in mind, that PAs bind to various compounds due to their small size and chemical simplicity. Therefore, a TCI with a PA-based "binding group" should non-covalently bind to a relatively high number of off-targets, increasing the risk of covalent bonding via its "functional group".

5 Appendix

CCATGGGAACCGATTGGCCGGTTTATCACCGCATCGATGGTCCGATCGTGATGATCGGCTTCGGCTCGATTGGCCGGGGC
ACGCTGCCCTTGATCGAACGTCACTTCGCGTTCGACCGGTCCAAGCTGGTGGTGATCGATCCCAGCGACGAGGCTCGTAA
GCTGGCCGAGGCGCGCGGCGTGCGCTTCATCCAGCAGGCGGTGACGCGCGACAACTATCGCGAACTCCTGGTGCCGCT
GCTCACCGCCGGGCCGGGGCAGGGCTTTTGCGTCAACCTCTCGGTCGACACCTCATCGCTCGACATCATGGAACTCGCCC
GCGAGAACGGCGCGCTCTACATCGACACCGTGGTCGAGCCGTGGCTTGGCTTCTATTTCGACCCCGACCTGAAGCCGGA
GGCGCGCTCGAACTACGCGCTGCGCGAGACCGTGCTGGCGGCGCGGCGCAACAAGCCGGGCGGCACCACTGCGGTGTC
GTGCTGCGGCGCCAACCCCGGCATGGTGTCGTGGTTCGTCAAGCAGGCGCTGGTCAACCTTGCCGCCGACCTCGGCGTG
ACGGGCGAGGAGCCCACCACCCGCGAGGAATGGGCGCGGCTTGCGATGGATCTCGGCGTCAAGGGCATCCACATCGCC
GAGCGCGACACCCAGCGCGCCAGCTTCCCCAAGCCGTTCGACGTGTTCGTCAACACCTGGTCGGTCGAGGGTTTCGTGTC
GGAGGGCCTGCAGCCGGCCGAGCTCGGCTGGGGCACCTTTGAGCGCTGGATGCCGGACAACGCCCGCGGCCACGACAG
CGGCTGCGGCGCGGGGATCTACCTGCTCCAGCCCGGCGCCAACACCCGCGTGCGGTCGTGGACGCCGACCGCGATGGC
GCAATACGGCTTCCTGGTCACCCACAACGAATCGATCTCGATCGCCGACTTCCTCACCGTGCGCGACGCTGCGGGCCAGG
CGGTCTACCGGCCGACCTGCCACTACGCCTACCACCCGTGCAACGACGCGGTGCTGTCGCTGCACGAGATGTTCGGCTC
GGGCAAGCGCCAGTCGGACTGGCGGATCCTGGACGAGACCGAAATCGTCGACGGCATCGACGAACTCGGCGTGCTGCTC
TACGGCCACGGCAAGAACGCCTATTGGTACGGCTCGCAGCTCTCGATCGAGGAGACGCGGCGGATCGCGCCCGACCAGA
ACGCCACCGGGCTGCAGGTGTCGTCGGCCGTGCTGGCGGGCATGGTGTGGGCGCTGGAAAACCCGAACGCCGGCATCG
TCGAGGCCGACGATCTCGACTTTCGCCGCTGCCTGGAGGTGCAGACGCCCTATCTCGGCCCGGTGGTCGGCGTCTACAC
CGACTGGACGCCGCTTGCCGGCCGGCCGGGCCTGTTCCCGGAGGACATCGACACCTCCGACCCGTGGCAGTTCCGCAAC
GTGCTGGTGCGGGACTGACTCGAG

Figure 32: DNA sequence of *Bv*HSS including cloning sites and stop codons.

The Bv*HSS-coding DNA was kindly provided by Dr. Krossa (Krossa et al. 2016) cloned into the pETM-14 plasmid via NcoI/XhoI-restriction sites. The 5'-CC- (green) and TGACTCGAG-3'-flanking DNA sequences are also given for clarity and provide 5'-NcoI (underlined) and 3'-XhoI (blue, underlined) restriction sites and one stop codon (red).*

CCATGGATTTTAGCATTAATCCGCCGCAGCGTATTGTTTTTGTTGGTCTGGGTACCATTGCGCAGTCATTTCTGCCGCTGCT
GAGCAAAGTTCATGATCTGTCTACCCTGGAAATTTATGCCATTGATCCGAAAACCCCGCCGCTGATTGAATATTTTGCCAAT
TCTTTTGGCCTGAAATTTATTAATAGCGCCATTGATCAGATTAATTATCGCGATATTCTGGTGCCGATTCTGGGCGAAGGTAC
CGTGCTGATTAATCTGTCAACCGATGTGAGCAGCCTGGCCCTGATTGAACTGTGCCGCTCTGCTGGTGCGCTGTATCTGGA
TACCTGCATTGAACCGTGGAAAGGTGGTTATGATGATCCGACCATTCCGCTGCATAAACGTACCAATTATCATCTGCGCGAA
CAGATGCTGAGCCTGAAAAAACGCCTGGGTAGTGGCGTGACCGCTCTGGTTGCCCACGGTGCTAATCCGGGTCTGGTTTC
ACATTTTGTGAAACGTGCCCTGCTGGATCTGGCAGAAGAAATTCTGGGTGATTGCAAAAAACCGTCTAATAAAGAACAGTGG
GCCATTCTGTCTCAGCGTCTGGGCGTGAAAGTTATTCATGTTGCAGAATATGATTCACAGATTTCTCAGAAATCACGCGAAC
GCGGTGAATTTGTGAATACCTGGAGCGTGCATGGCTTTATTTCAGAAAGCCAGCAGCCGGCGGAACTGGGTTGGGGTTCT
CATGAACGTTCACTGCCGACCGATGCTAGTATGCATACCGATGGCTGTGGTGCGGCAATTTATATTGAAAAACCGGGTGCC
AGCGTTCGTGTGAAAACCTGGACCCCGTTTAATGGCCCGTCTCTGGGTTATCTGGTTACCCATCATGAAGCCATTTCAATTG
CGGATTTTCTGACCCTGCGCACCGCGGATGAAACCTATCGCCCGACCGTTCATTATGCTTATCGTCCGAGTGATGAAGCTA
TTCTGTCTGTTCATGAATGGTTTGGCAATGATTGTATGACCCCGGAAAAAACCAAAGTTCTGCGTCCGGGCGATATTCTGAG
CGGTTCTGATTATCTGGGCGTGCTGCTGATGGGCCATGAAAAATCAAGCTATTGGTATGGCAGTATTCTGAGCATTGAAAAA
GCTAAAGAACTGGCGACCCTGAATACCGCTACCACCCTGCAGGTGGCAGCAGGCGTTCTGTCAGGCTATCTGTGGATTCT
GTCTCATCCGTCAGCAGGTATTATTGAAGCAGAAGATATGGATCATGAAGTTGCACTGAGTTATATTAGTCAGTATCTGGGT
GAACTGAAAGGTGTTTATAGTGATTGGAATCCGACCAAAAATAATCCGGGCACCTTTAGTGCGATTGATAGTGATAGTCCGT
GGCTGTTTAGTAATTTTGTGCTGTAATAACTCGAG

Figure 33: DNA sequence of *Pa*HSS including cloning sites and stop codons.

The Pa*HSS amino acid sequence (UniProtKB Q6X2Y9) was back-translated into an* E. coli *K12 codon-optimized DNA sequence (black). Addition of 5'-CC (green) and TAATAACTCGAG-3' to the termini of the DNA sequence provided 5'-NcoI (underlined) and 3'-XhoI (blue, underlined) restriction sites and two stop codons (red).*

6 References

Adair CG, Gorman SP, Feron BM, Byers LM, Jones DS, Goldsmith CE, Moore JE, Kerr JR, Curran MD, Hogg G, et al. 1999. Implications of endotracheal tube biofilm for ventilator-associated pneumonia. Intensive Care Med. 25(10):1072–1076. eng. doi:10.1007/s001340051014.

Afonine PV, Grosse-Kunstleve RW, Echols N, Headd JJ, Moriarty NW, Mustyakimov M, Terwilliger TC, Urzhumtsev A, Zwart PH, Adams PD. 2012. Towards automated crystallographic structure refinement with phenix.refine. Acta Crystallogr D Biol Crystallogr. 68(Pt 4):352–367. eng. doi:10.1107/S0907444912001308.

Aiba Y, Watanabe T, Terasawa Y, Nakano C, Hoshino T. 2018. Strictly Conserved Residues in Euphorbia tirucalli β-Amyrin Cyclase: Trp612 Stabilizes Transient Cation through Cation-π Interaction and CH-π Interaction of Tyr736 with Leu734 Confers Robust Local Protein Architecture. Chembiochem. 19(5):486–495. eng. doi:10.1002/cbic.201700572.

Anantharajah A, Mingeot-Leclercq M-P, van Bambeke F. 2016. Targeting the Type Three Secretion System in Pseudomonas aeruginosa. Trends Pharmacol Sci. 37(9):734–749. eng. doi:10.1016/j.tips.2016.05.011.

Baars O, Morel FMM, Zhang X. 2018. The purple non-sulfur bacterium Rhodopseudomonas palustris produces novel petrobactin-related siderophores under aerobic and anaerobic conditions. Environ Microbiol. 20(5):1667–1676. eng. doi:10.1111/1462-2920.14078.

Bae D-H, Lane DJR, Jansson PJ, Des Richardson R. 2018. The old and new biochemistry of polyamines. Biochim Biophys Acta Gen Subj. 1862(9):2053–2068. eng. doi:10.1016/j.bbagen.2018.06.004.

Becerra-Rivera VA, Bergström E, Thomas-Oates J, Dunn MF. 2018. Polyamines are required for normal growth in Sinorhizobium meliloti. Microbiology (Reading, Engl). 164(4):600–613. eng. doi:10.1099/mic.0.000615.

Becker NN, Roberts JD. 1984. Structure of the liver alcohol dehydrogenase-NAD+-pyrazole complex as determined by 15N NMR spectroscopy. Biochemistry. 23(14):3336–3340. eng. doi:10.1021/bi00309a034.

Beene DL, Brandt GS, Zhong W, Zacharias NM, Lester HA, Dougherty DA. 2002. Cation-pi interactions in ligand recognition by serotonergic (5-HT3A) and nicotinic acetylcholine receptors: The anomalous binding properties of nicotine. Biochemistry. 41(32):10262–10269. eng. doi:10.1021/bi020266d.

Benach J, Atrian S, Gonzàlez-Duarte R, Ladenstein R. 1999. The catalytic reaction and inhibition mechanism of Drosophila alcohol dehydrogenase: Observation of an enzyme-bound NAD-ketone adduct at 1.4 Å resolution by X-ray crystallography. J Mol Biol. 289(2):335–355. doi:10.1006/jmbi.1999.2765.

Bencini A, Bianchi A, Garcia-España E, Micheloni M, Ramirez JA. 1999. Proton coordination by polyamine compounds in aqueous solution. Coord Chem Rev. 188(1):97–156. doi:10.1016/S0010-

8545(98)00243-4.

Berube BJ, Rangel SM, Hauser AR. 2016. Pseudomonas aeruginosa: Breaking down barriers. Curr Genet. 62(1):109–113. eng. doi:10.1007/s00294-015-0522-x.

Bitonti AJ, McCann PP, Sjoerdsma A. 1982. Restriction of bacterial growth by inhibition of polyamine biosynthesis by using monofluoromethylornithine, difluoromethylarginine and dicyclohexyl ammonium sulphate. Biochem J. 208(2):435–441. eng. doi:10.1042/bj2080435.

Bolard A, Schniederjans M, Haussler S, Triponney P, Valot B, Plesiat P, Jeannot K. 2019. Production of norspermidine contributes to aminoglycoside resistance in pmrAB mutants of Pseudomonas aeruginosa. Antimicrob Agents Chemother. eng. doi:10.1128/AAC.01044-19.

Boles BR, Singh PK. 2008. Endogenous oxidative stress produces diversity and adaptability in biofilm communities. Proc Natl Acad Sci USA. 105(34):12503–12508. eng. doi:10.1073/pnas.0801499105.

Bontemps-Gallo S, Lawrence KA, Richards CL, Gherardini FC. 2018. Borrelia burgdorferi genes, bb0639-0642, encode a putative putrescine/spermidine transport system, PotABCD, that is spermidine specific and essential for cell survival. Mol Microbiol. 108(4):350–360. eng. doi:10.1111/mmi.13940.

Borrell A, Culianez-Macia FA, Altabella T, Besford RT, Flores D, Tiburcio AF. 1995. Arginine Decarboxylase Is Localized in Chloroplasts. Plant Physiol. 109(3):771–776. eng. doi:10.1104/pp.109.3.771.

Borrero-de Acuña JM, Timmis KN, Jahn M, Jahn D. 2017. Protein complex formation during denitrification by Pseudomonas aeruginosa. Microb Biotechnol. 10(6):1523–1534. eng. doi:10.1111/1751-7915.12851.

Böttcher F, Ober D, Hartmann T. 1994. Biosynthesis of pyrrolizidine alkaloids: Putrescine and spermidine are essential substrates of enzymatic homospermidine formation. Canadian Journal of Chemistry. 72(1):80–85. doi:10.1139/v94-013.

Bowie D. 2018. Polyamine-mediated channel block of ionotropic glutamate receptors and its regulation by auxiliary proteins. J Biol Chem. 293(48):18789–18802. eng. doi:10.1074/jbc.TM118.003794.

Brünger AT. 1992. Free R value: A novel statistical quantity for assessing the accuracy of crystal structures. Nature. 355(6359):472–475. eng. doi:10.1038/355472a0.

Bull HG, Garcia-Calvo M, Andersson S, Baginsky WF, Chan HK, Ellsworth DE, Miller RR, Stearns RA, Bakshi RK, Rasmusson GH, et al. 1996. Mechanism-Based Inhibition of Human Steroid 5α-Reductase by Finasteride: Enzyme-Catalyzed Formation of NADP−Dihydrofinasteride, a Potent Bisubstrate Analog Inhibitor. J Am Chem Soc. 118(10):2359–2365. doi:10.1021/ja953069t.

Burley SK, Petsko GA. 1986. Amino-aromatic interactions in proteins. FEBS Lett. 203(2):139–143. doi:10.1016/0014-5793(86)80730-X.

Burnat M, Li B, Kim SH, Michael AJ, Flores E. 2018. Homospermidine biosynthesis in the cyanobacterium Anabaena requires a deoxyhypusine synthase homologue and is essential for

normal diazotrophic growth. Mol Microbiol. 109(6):763–780. eng. doi:10.1111/mmi.14006.

Burrell M, Hanfrey CC, Murray EJ, Stanley-Wall NR, Michael AJ. 2010. Evolution and multiplicity of arginine decarboxylases in polyamine biosynthesis and essential role in Bacillus subtilis biofilm formation. J Biol Chem. 285(50):39224–39238. eng. doi:10.1074/jbc.M110.163154.

Cardile AP, Woodbury RL, Sanchez CJ, Becerra SC, Garcia RA, Mende K, Wenke JC, Akers KS. 2017. Activity of Norspermidine on Bacterial Biofilms of Multidrug-Resistant Clinical Isolates Associated with Persistent Extremity Wound Infections. Adv Exp Med Biol. 973:53–70. eng. doi:10.1007/5584_2016_93.

Casero RA, Murray Stewart T, Pegg AE. 2018. Polyamine metabolism and cancer: Treatments, challenges and opportunities. Nat Rev Cancer. 18(11):681–695. eng. doi:10.1038/s41568-018-0050-3.

Chattopadhyay MK, Park MH, Tabor H. 2008. Hypusine modification for growth is the major function of spermidine in Saccharomyces cerevisiae polyamine auxotrophs grown in limiting spermidine. Proc Natl Acad Sci USA. 105(18):6554–6559. eng. doi:10.1073/pnas.0710970105.

Chattopadhyay MK, Tabor CW, Tabor H. 2003. Polyamines protect Escherichia coli cells from the toxic effect of oxygen. Proc Natl Acad Sci USA. 100(5):2261–2265. eng. doi:10.1073/pnas.2627990100.

Chattopadhyay MK, Tabor CW, Tabor H. 2009. Polyamines are not required for aerobic growth of Escherichia coli: Preparation of a strain with deletions in all of the genes for polyamine biosynthesis. J Bacteriol. 191(17):5549–5552. eng. doi:10.1128/JB.00381-09.

Chen D, Shao Q, Yin L, Younis A, Zheng B. 2018. Polyamine Function in Plants: Metabolism, Regulation on Development, and Roles in Abiotic Stress Responses. Front Plant Sci. 9:1945. eng. doi:10.3389/fpls.2018.01945.

Chipot C, Maigret B, Pearlman DA, Kollman PA. 1996. Molecular Dynamics Potential of Mean Force Calculations: A Study of the Toluene−Ammonium π-Cation Interactions. J Am Chem Soc. 118(12):2998–3005. doi:10.1021/ja950302e.

Choe J, Guerra D, Michels PAM, Hol WGJ. 2003. Leishmania mexicana glycerol-3-phosphate dehydrogenase showed conformational changes upon binding a bi-substrate adduct. J Mol Biol. 329(2):335–349. eng. doi:10.1016/s0022-2836(03)00421-2.

Chou HT, Hegazy M, Lu C-D. 2010. L-lysine catabolism is controlled by L-arginine and ArgR in Pseudomonas aeruginosa PAO1. J Bacteriol. 192(22):5874–5880. eng. doi:10.1128/JB.00673-10.

Ciofu O, Tolker-Nielsen T. 2019. Tolerance and Resistance of Pseudomonas aeruginosa Biofilms to Antimicrobial Agents-How P. aeruginosa Can Escape Antibiotics. Front Microbiol. 10:913. eng. doi:10.3389/fmicb.2019.00913.

Cohen SS. 1998. A guide to the polyamines. New York, NY: Oxford Univ. Press. 595 p. ISBN: 0195110641.

Collard F, Fagan RL, Zhang J, Nemet I, Palfey BA, Monnier VM. 2011. The cation-π interaction between Lys53 and the flavin of fructosamine oxidase (FAOX-II) is critical for activity. Biochemistry.

50(37):7977–7986. eng. doi:10.1021/bi1020666.

Craig L, Pique ME, Tainer JA. 2004. Type IV pilus structure and bacterial pathogenicity. Nat Rev Microbiol. 2(5):363–378. eng. doi:10.1038/nrmicro885.

Crowley PB, Golovin A. 2005. Cation-pi interactions in protein-protein interfaces. Proteins. 59(2):231–239. eng. doi:10.1002/prot.20417.

Dasu VV, Nakada Y, Ohnishi-Kameyama M, Kimura K, Itoh Y. 2006. Characterization and a role of Pseudomonas aeruginosa spermidine dehydrogenase in polyamine catabolism. Microbiology (Reading, Engl). 152(Pt 8):2265–2272. eng. doi:10.1099/mic.0.28920-0.

Davis MR, Dougherty DA. 2015. Cation–π interactions: Computational analyses of the aromatic box motif and the fluorination strategy for experimental evaluation. Phys Chem Chem Phys. 17(43):29262–29270. doi:10.1039/C5CP04668H.

Dettman JR, Rodrigue N, Aaron SD, Kassen R. 2013. Evolutionary genomics of epidemic and nonepidemic strains of Pseudomonas aeruginosa. Proc Natl Acad Sci USA. 110(52):21065–21070. eng. doi:10.1073/pnas.1307862110.

Diaz MH, Shaver CM, King JD, Musunuri S, Kazzaz JA, Hauser AR. 2008. Pseudomonas aeruginosa induces localized immunosuppression during pneumonia. Infect Immun. 76(10):4414–4421. eng. doi:10.1128/IAI.00012-08.

Diederichs K. 2010. Quantifying instrument errors in macromolecular X-ray data sets. Acta Crystallogr D Biol Crystallogr. 66(Pt 6):733–740. eng. doi:10.1107/S0907444910014836.

Diederichs K, Karplus PA. 1997. Improved R-factors for diffraction data analysis in macromolecular crystallography. Nat Struct Mol Biol. 4(4):269–275. doi:10.1038/nsb0497-269.

Diederichs K, Karplus PA. 2013. Better models by discarding data? Acta Crystallogr D Biol Crystallogr. 69(Pt 7):1215–1222. eng. doi:10.1107/S0907444913001121.

Ding Y, Peng N, Du Y, Ji L, Cao B. 2014. Disruption of putrescine biosynthesis in Shewanella oneidensis enhances biofilm cohesiveness and performance in Cr(VI) immobilization. Appl Environ Microbiol. 80(4):1498–1506. eng. doi:10.1128/AEM.03461-13.

Dougherty DA. 1996. Cation-pi interactions in chemistry and biology: A new view of benzene, Phe, Tyr, and Trp. Science. 271(5246):163–168. eng. doi:10.1126/science.271.5246.163.

Du Q-S, Meng J-Z, Liao S-M, Huang R-B. 2012. Energies and physicochemical properties of cation-π interactions in biological structures. J Mol Graph Model. 34:38–45. eng. doi:10.1016/j.jmgm.2011.12.002.

Emsley P, Lohkamp B, Scott WG, Cowtan K. 2010. Features and development of Coot. Acta Crystallogr D Biol Crystallogr. 66(Pt 4):486–501. eng. doi:10.1107/S0907444910007493.

Ernst RK, Adams KN, Moskowitz SM, Kraig GM, Kawasaki K, Stead CM, Trent MS, Miller SI. 2006. The Pseudomonas aeruginosa lipid A deacylase: Selection for expression and loss within the cystic fibrosis airway. J Bacteriol. 188(1):191–201. eng. doi:10.1128/JB.188.1.191-201.2006.

Evans PR. 2011. An introduction to data reduction: Space-group determination, scaling and intensity statistics. Acta Crystallogr D Biol Crystallogr. 67(Pt 4):282–292. eng. doi:10.1107/S090744491003982X.

Everse J, Barnett RE, Thorne CJR, Kaplan NO. 1971. The formation of ternary complexes by diphosphopyridine nucleotide-dependent dehydrogenases. Arch Biochem Biophys. 143(2):444–460. doi:10.1016/0003-9861(71)90230-X.

Faraldos JA, Antonczak AK, González V, Fullerton R, Tippmann EM, Allemann RK. 2011. Probing eudesmane cation-π interactions in catalysis by aristolochene synthase with non-canonical amino acids. J Am Chem Soc. 133(35):13906–13909. eng. doi:10.1021/ja205927u.

Faure E, Kwong K, Nguyen D. 2018. Pseudomonas aeruginosa in Chronic Lung Infections: How to Adapt Within the Host? Front Immunol. 9:2416. eng. doi:10.3389/fimmu.2018.02416.

Ferioli M. 2000. Prolactin and polyamine catabolism: Specific effect on polyamine oxidase activity in rat thymus. Mol Cell Endocrinol. 165(1-2):51–56. doi:10.1016/S0303-7207(00)00264-1.

Frimmersdorf E, Horatzek S, Pelnikevich A, Wiehlmann L, Schomburg D. 2010. How Pseudomonas aeruginosa adapts to various environments: A metabolomic approach. Environ Microbiol. 12(6):1734–1747. eng. doi:10.1111/j.1462-2920.2010.02253.x.

Gale EF, Epps HM. 1944. Studies on bacterial amino-acid decarboxylases: 1. l(+)-lysine decarboxylase. Biochem J. 38(3):232–242. eng. doi:10.1042/bj0380232.

Galle M, Carpentier I, Beyaert R. 2012. Structure and function of the Type III secretion system of Pseudomonas aeruginosa. Curr Protein Pept Sci. 13(8):831–842. eng.

Gallivan JP, Dougherty DA. 1999. Cation-pi interactions in structural biology. Proc Natl Acad Sci USA. 96(17):9459–9464. eng. doi:10.1073/pnas.96.17.9459.

Gasteiger E, Hoogland C, Gattiker A, Duvaud S'e, Wilkins MR, Appel RD, Bairoch A. 2005. Protein Identification and Analysis Tools on the ExPASy Server. In: Walker JM, editor. The Proteomics Protocols Handbook. Totowa, NJ: Humana Press Inc. p. 571–607 (Methods in Molecular Biology).

Gooderham WJ, Hancock REW. 2009. Regulation of virulence and antibiotic resistance by two-component regulatory systems in Pseudomonas aeruginosa. FEMS Microbiol Rev. 33(2):279–294. eng. doi:10.1111/j.1574-6976.2008.00135.x.

Green R, Hanfrey CC, Elliott KA, McCloskey DE, Wang X, Kanugula S, Pegg AE, Michael AJ. 2011. Independent evolutionary origins of functional polyamine biosynthetic enzyme fusions catalysing de novo diamine to triamine formation. Mol Microbiol. 81(4):1109–1124. eng. doi:10.1111/j.1365-2958.2011.07757.x.

Griffiths GL, Sigel SP, Payne SM, Neilands JB. 1984. Vibriobactin, a siderophore from Vibrio cholerae. J Biol Chem. 259(1):383–385. eng.

Gutfreund H, Cantwell R, McMurray CH, Criddle RS, Hathaway G. 1968. The kinetics of the reversible inhibition of heart lactate dehydrogenase through the formation of the enzyme-oxidized nicotinamide-adenine dinucleotide-pyruvate compounds. Biochem J. 106(3):683–687. eng.

doi:10.1042/bj1060683.

Ha HC, Sirisoma NS, Kuppusamy P, Zweier JL, Woster PM, Casero RA. 1998. The natural polyamine spermine functions directly as a free radical scavenger. Proc Natl Acad Sci USA. 95(19):11140–11145. eng. doi:10.1073/pnas.95.19.11140.

Hamana K, Matsuzaki S. 1992. Polyamines as a chemotaxonomic marker in bacterial systematics. Crit Rev Microbiol. 18(4):261–283. eng. doi:10.3109/10408419209113518.

Hamana K, Saito T, Okada M, Sakamoto A, Hosoya R. 2002. Covalently linked polyamines in the cell wall peptidoglycan of Selenomonas, Anaeromusa, Dendrosporobacter, Acidaminococcus and Anaerovibrio belonging to the Sporomusa subbranch. J Gen Appl Microbiol. 48(3):177–180. eng.

Hamana K, Sato W, Gouma K, Yu J, Uemura Y, Mochizuki C, Takatsuka K, Kasai H, Yokota A. 2007. Cellular polyamine catalogues of the five classes of the phylum Proteobacteria: Distributions of homospermidine within the class Alphaproteobacteria, hydroxyputrescine within the class Betaproteobacteria, norspermidine within the class Gammaproteobacteria, and spermidine within the classes Deltaproteobacteria and Epsilonproteobacteria. Ann Gunma Health Sci. 27:1–16.

Hamasaki-Katagiri N, Katagiri Y, Tabor CW, Tabor H. 1998. Spermine is not essential for growth of Saccharomyces cerevisiae: Identification of the SPE4 gene (spermine synthase) and characterization of a spe4 deletion mutant. Gene. 210(2):195–201. doi:10.1016/S0378-1119(98)00027-4.

Hancock RE, Mutharia LM, Chan L, Darveau RP, Speert DP, Pier GB. 1983. Pseudomonas aeruginosa isolates from patients with cystic fibrosis: A class of serum-sensitive, nontypable strains deficient in lipopolysaccharide O side chains. Infect Immun. 42(1):170–177. eng.

Handa AK, Fatima T, Mattoo AK. 2018. Polyamines: Bio-Molecules with Diverse Functions in Plant and Human Health and Disease. Front Chem. 6:10. eng. doi:10.3389/fchem.2018.00010.

Hanfrey CC, Pearson BM, Hazeldine S, Lee J, Gaskin DJ, Woster PM, Phillips MA, Michael AJ. 2011. Alternative spermidine biosynthetic route is critical for growth of Campylobacter jejuni and is the dominant polyamine pathway in human gut microbiota. J Biol Chem. 286(50):43301–43312. eng. doi:10.1074/jbc.M111.307835.

Hatherley R, Brown DK, Glenister M, Tastan Bishop Ö. 2016. PRIMO: An Interactive Homology Modeling Pipeline. PLoS ONE. 11(11):e0166698. eng. doi:10.1371/journal.pone.0166698.

Hauser AR. 2009. The type III secretion system of Pseudomonas aeruginosa: Infection by injection. Nat Rev Microbiol. 7(9):654–665. eng. doi:10.1038/nrmicro2199.

Hibasami H, Tanaka M, Nagai J, Ikeda T. 1980. Dicyclohexylamine, a potent inhibitor of spermidine synthase in mammalian cells. FEBS Lett. 116(1):99–101. eng. doi:10.1016/0014-5793(80)80537-0.

Hill RM, Smith WV. 1951. Microwave Collision Diameters and Associated Quadrupole Moments. Phys Rev. 82(3):451. doi:10.1103/PhysRev.82.451.

Hirao T, Sato M, Shirahata A, Kamio Y. 2000. Covalent linkage of polyamines to peptidoglycan in

Anaerovibrio lipolytica. J Bacteriol. 182(4):1154–1157. eng. doi:10.1128/jb.182.4.1154-1157.2000.

Ho BK, Gruswitz F. 2008. HOLLOW: Generating Accurate Representations of Channel and Interior Surfaces in Molecular Structures. BMC Struct Biol. 8(1):49. doi:10.1186/1472-6807-8-49.

Hobley L, Kim SH, Maezato Y, Wyllie S, Fairlamb AH, Stanley-Wall NR, Michael AJ. 2014. Norspermidine is not a self-produced trigger for biofilm disassembly. Cell. 156(4):844–854. eng. doi:10.1016/j.cell.2014.01.012.

Hobley L, Li B, Wood JL, Kim SH, Naidoo J, Ferreira AS, Khomutov M, Khomutov A, Stanley-Wall NR, Michael AJ. 2017. Spermidine promotes Bacillus subtilis biofilm formation by activating expression of the matrix regulator slrR. J Biol Chem. 292(29):12041–12053. eng. doi:10.1074/jbc.M117.789644.

Horcajada JP, Montero M, Oliver A, Sorlí L, Luque S, Gómez-Zorrilla S, Benito N, Grau S. 2019. Epidemiology and Treatment of Multidrug-Resistant and Extensively Drug-Resistant Pseudomonas aeruginosa Infections. Clin Microbiol Rev. 32(4). eng. doi:10.1128/CMR.00031-19.

Horvath MP, Schweiker VL, Bevilacqua JM, Ruggles JA, Schultz SC. 1998. Crystal Structure of the Oxytricha nova Telomere End Binding Protein Complexed with Single Strand DNA. Cell. 95(7):963–974. doi:10.1016/S0092-8674(00)81720-1.

Igarashi K, Kashiwagi K. 2019. The functional role of polyamines in eukaryotic cells. Int J Biochem Cell Biol. 107:104–115. eng. doi:10.1016/j.biocel.2018.12.012.

Ikai H, Yamamoto S. 1994. Cloning and expression in Escherichia coli of the gene encoding a novel L-2,4-diaminobutyrate decarboxylase of Acinetobacter baumannii. FEMS Microbiol Lett. 124(2):225–228. doi:10.1111/j.1574-6968.1994.tb07288.x.

Ikai H, Yamamoto S. 1997. Identification and analysis of a gene encoding L-2,4-diaminobutyrate:2-ketoglutarate 4-aminotransferase involved in the 1,3-diaminopropane production pathway in Acinetobacter baumannii. J Bacteriol. 179(16):5118–5125. eng. doi:10.1128/jb.179.16.5118-5125.1997.

Illingworth C, Mayer MJ, Elliott K, Hanfrey C, Walton NJ, Michael AJ. 2003. The diverse bacterial origins of the Arabidopsis polyamine biosynthetic pathway. FEBS Lett. 549(1-3):26–30. eng. doi:10.1016/s0014-5793(03)00756-7.

Ito R, Hashimoto I, Masukawa Y, Hoshino T. 2013. Effect of Cation-π Interactions and Steric Bulk on the Catalytic Action of Oxidosqualene Cyclase: A Case Study of Phe728 of β-Amyrin Synthase from Euphorbia tirucalli L. Chem. Eur. J. 19(50):17150–17158. doi:10.1002/chem.201301917.

Ito R, Masukawa Y, Nakada C, Amari K, Nakano C, Hoshino T. 2014. β-Amyrin synthase from Euphorbia tirucalli. Steric bulk, not the π-electrons of Phe, at position 474 has a key role in affording the correct folding of the substrate to complete the normal polycyclization cascade. Org. Biomol. Chem. 12(23):3836–3846. doi:10.1039/C4OB00064A.

Ito R, Nakada C, Hoshino T. 2017. Correction: B-Amyrin synthase from Euphorbia tirucalli L. functional analyses of the highly conserved aromatic residues Phe413, Tyr259 and Trp257 disclose the

importance of the appropriate steric bulk, and cation–π and CH–π interactions for the efficient catalytic action of the polyolefin cyclization cascade. Org. Biomol. Chem. 15(3):717. doi:10.1039/C6OB90192A.

Jacques SL, Mirza IA, Ejim L, Koteva K, Hughes DW, Green K, Kinach R, Honek JF, Lai HK, Berghuis AM, et al. 2003. Enzyme-assisted suicide: Molecular basis for the antifungal activity of 5-hydroxy-4-oxonorvaline by potent inhibition of homoserine dehydrogenase. Chem Biol. 10(10):989–995. eng. doi:10.1016/j.chembiol.2003.09.015.

Janowitz T, Kneifel H, Piotrowski M. 2003. Identification and characterization of plant agmatine iminohydrolase, the last missing link in polyamine biosynthesis of plants. FEBS Lett. 544(1-3):258–261. eng. doi:10.1016/s0014-5793(03)00515-5.

Jensen LH. 1985. Overview of refinement in macromolecular structure analysis. In: Wyckoff HW, editor. Diffraction methods for biological macromolecules. Vol. 115. New York, NY: Acad. Press. p. 227–234 (Methods in Enzymology; vol. 115).

Jesaitis AJ, Franklin MJ, Berglund D, Sasaki M, Lord CI, Bleazard JB, Duffy JE, Beyenal H, Lewandowski Z. 2003. Compromised host defense on Pseudomonas aeruginosa biofilms: Characterization of neutrophil and biofilm interactions. J Immunol. 171(8):4329–4339. eng. doi:10.4049/jimmunol.171.8.4329.

Johnson L, Mulcahy H, Kanevets U, Shi Y, Lewenza S. 2012. Surface-localized spermidine protects the Pseudomonas aeruginosa outer membrane from antibiotic treatment and oxidative stress. J Bacteriol. 194(4):813–826. eng. doi:10.1128/JB.05230-11.

Jones TA, Zou JY, Cowan SW, Kjeldgaard M. 1991. Improved methods for building protein models in electron density maps and the location of errors in these models. Acta Crystallogr A. 47 (Pt 2):110–119. eng. doi:10.1107/s0108767390010224.

Joshi GS, Spontak JS, Klapper DG, Richardson AR. 2011. Arginine catabolic mobile element encoded speG abrogates the unique hypersensitivity of Staphylococcus aureus to exogenous polyamines. Mol Microbiol. 82(1):9–20. eng. doi:10.1111/j.1365-2958.2011.07809.x.

Jung IL, Kim IG. 2003. Polyamines and glutamate decarboxylase-based acid resistance in Escherichia coli. J Biol Chem. 278(25):22846–22852. eng. doi:10.1074/jbc.M212055200.

Juszczak LJ, Eisenberg AS. 2017. The Color of Cation-π Interactions: Subtleties of Amine-Tryptophan Interaction Energetics Allow for Radical-like Visible Absorbance and Fluorescence. J Am Chem Soc. 139(24):8302–8311. doi:10.1021/jacs.7b03442.

Kabsch W. 2010. XDS. Acta Crystallogr D Biol Crystallogr. 66(Pt 2):125–132. eng. doi:10.1107/S0907444909047337.

Kallio A, McCann PP. 1981. Difluoromethylornithine irreversibly inactivates ornithine decarboxylase of Pseudomonas aeruginosa, but does not inhibit the enzymes of Escherichia coli. Biochem J. 200(1):69–75. eng. doi:10.1042/bj2000069.

Kallio A, McCann PP, Bey P. 1981. DL-alpha-(Difluoromethyl)arginine: A potent enzyme-activated

irreversible inhibitor of bacterial decarboxylases. Biochemistry. 20(11):3163–3168. eng. doi:10.1021/bi00514a027.

Kamio Y, Itoh Y, Terawaki Y, Kusano T. 1981. Cadaverine is covalently linked to peptidoglycan in Selenomonas ruminantium. J Bacteriol. 145(1):122–128. eng.

Kamio Y, Pösö H, Terawaki Y, Paulin L. 1986. Cadaverine covalently linked to a peptidoglycan is an essential constituent of the peptidoglycan necessary for the normal growth in Selenomonas ruminantium. J Biol Chem. 261(14):6585–6589. eng.

Kanerva K, Mäkitie LT, Pelander A, Heiskala M, Andersson LC. 2008. Human ornithine decarboxylase paralogue (ODCp) is an antizyme inhibitor but not an arginine decarboxylase. Biochem J. 409(1):187–192. eng. doi:10.1042/BJ20071004.

Karatan E, Duncan TR, Watnick PI. 2005. NspS, a predicted polyamine sensor, mediates activation of Vibrio cholerae biofilm formation by norspermidine. J Bacteriol. 187(21):7434–7443. eng. doi:10.1128/JB.187.21.7434-7443.2005.

Karplus PA, Diederichs K. 2012. Linking crystallographic model and data quality. Science. 336(6084):1030–1033. eng. doi:10.1126/science.1218231.

Karplus PA, Diederichs K. 2015. Assessing and maximizing data quality in macromolecular crystallography. Curr Opin Struct Biol. 34:60–68. eng. doi:10.1016/j.sbi.2015.07.003.

Kera K, Nagayama T, Nanatani K, Saeki-Yamoto C, Tominaga A, Souma S, Miura N, Takeda K, Kayamori S, Ando E, et al. 2018. Reduction of Spermidine Content Resulting from Inactivation of Two Arginine Decarboxylases Increases Biofilm Formation in Synechocystis sp. Strain PCC 6803. J Bacteriol. 200(9). eng. doi:10.1128/JB.00664-17.

Khan AU, Di Mascio P, Medeiros MH, Wilson T. 1992. Spermine and spermidine protection of plasmid DNA against single-strand breaks induced by singlet oxygen. Proc Natl Acad Sci USA. 89(23):11428–11430. eng. doi:10.1073/pnas.89.23.11428.

Khan AU, Mei YH, Wilson T. 1992. A proposed function for spermine and spermidine: Protection of replicating DNA against damage by singlet oxygen. Proc Natl Acad Sci USA. 89(23):11426–11427. eng. doi:10.1073/pnas.89.23.11426.

Kim J-S, Choi SH, Lee JK. 2006. Lysine decarboxylase expression by Vibrio vulnificus is induced by SoxR in response to superoxide stress. J Bacteriol. 188(24):8586–8592. eng. doi:10.1128/JB.01084-06.

Kim SH, Wang Y, Khomutov M, Khomutov A, Fuqua C, Michael AJ. 2016. The Essential Role of Spermidine in Growth of Agrobacterium tumefaciens Is Determined by the 1,3-Diaminopropane Moiety. ACS Chem Biol. 11(2):491–499. eng. doi:10.1021/acschembio.5b00893.

Klockgether J, Cramer N, Wiehlmann L, Davenport CF, Tümmler B. 2011. Pseudomonas aeruginosa Genomic Structure and Diversity. Front Microbiol. 2:150. eng. doi:10.3389/fmicb.2011.00150.

Knudsen M, Wiuf C. 2010. The CATH database. Hum Genomics. 4(3):207. doi:10.1186/1479-7364-4-3-207.

Köhler T, Curty LK, Barja F, van Delden C, Pechère JC. 2000. Swarming of Pseudomonas aeruginosa is dependent on cell-to-cell signaling and requires flagella and pili. J Bacteriol. 182(21):5990–5996. eng. doi:10.1128/jb.182.21.5990-5996.2000.

Kollef MH, Chastre J, Fagon J-Y, François B, Niederman MS, Rello J, Torres A, Vincent J-L, Wunderink RG, Go KW, et al. 2014. Global prospective epidemiologic and surveillance study of ventilator-associated pneumonia due to Pseudomonas aeruginosa. Crit Care Med. 42(10):2178–2187. eng. doi:10.1097/CCM.0000000000000510.

Kollonitsch J, Perkins LM, Patchett AA, Doldouras GA, Marburg S, Duggan DE, Maycock AL, Aster SD. 1978. Selective inhibitors of biosynthesis of aminergic neurotransmitters. Nature. 274(5674):906–908. eng. doi:10.1038/274906a0.

Krämer A, Herzer J, Overhage J, Meyer-Almes F-J. 2016. Substrate specificity and function of acetylpolyamine amidohydrolases from Pseudomonas aeruginosa. BMC Biochem. 17:4. eng. doi:10.1186/s12858-016-0063-z.

Kresse AU, Dinesh SD, Larbig K, Römling U. 2003. Impact of large chromosomal inversions on the adaptation and evolution of Pseudomonas aeruginosa chronically colonizing cystic fibrosis lungs. Mol Microbiol. 47(1):145–158. eng. doi:10.1046/j.1365-2958.2003.03261.x.

Krossa S, Faust A, Ober D, Scheidig AJ. 2016. Comprehensive Structural Characterization of the Bacterial Homospermidine Synthase–an Essential Enzyme of the Polyamine Metabolism. Sci Rep. 6:19501. doi:10.1038/srep19501.

Kwon DH, Lu C-D. 2006a. Polyamines increase antibiotic susceptibility in Pseudomonas aeruginosa. Antimicrob Agents Chemother. 50(5):1623–1627. eng. doi:10.1128/AAC.50.5.1623-1627.2006.

Kwon DH, Lu C-D. 2006b. Polyamines induce resistance to cationic peptide, aminoglycoside, and quinolone antibiotics in Pseudomonas aeruginosa PAO1. Antimicrob Agents Chemother. 50(5):1615–1622. eng. doi:10.1128/AAC.50.5.1615-1622.2006.

Kwon D-H, Lu C-D. 2007. Polyamine effects on antibiotic susceptibility in bacteria. Antimicrob Agents Chemother. 51(6):2070–2077. eng. doi:10.1128/AAC.01472-06.

Laemmli UK. 1970. Cleavage of Structural Proteins during the Assembly of the Head of Bacteriophage T4. Nature. 227(5259):680–685. doi:10.1038/227680a0.

Lam JS, Taylor VL, Islam ST, Hao Y, Kocíncová D. 2011. Genetic and Functional Diversity of Pseudomonas aeruginosa Lipopolysaccharide. Front Microbiol. 2:118. eng. doi:10.3389/fmicb.2011.00118.

Laskowski RA, Jabłońska J, Pravda L, Vařeková RS, Thornton JM. 2018. PDBsum: Structural summaries of PDB entries. Protein Sci. 27(1):129–134. doi:10.1002/pro.3289.

Lauren Cason A, Ikeguchi Y, Skinner C, Wood TC, Holden KR, Lubs HA, Martinez F, Simensen RJ, Stevenson RE, Pegg AE, et al. 2003. X-linked spermine synthase gene (SMS) defect: The first polyamine deficiency syndrome. Eur J Hum Genet. 11(12):937–944. doi:10.1038/sj.ejhg.5201072.

Lee J, Sperandio V, Frantz DE, Longgood J, Camilli A, Phillips MA, Michael AJ. 2009. An alternative

polyamine biosynthetic pathway is widespread in bacteria and essential for biofilm formation in Vibrio cholerae. J Biol Chem. 284(15):9899–9907. eng. doi:10.1074/jbc.M900110200.

Lee J, Zhang L. 2015. The hierarchy quorum sensing network in Pseudomonas aeruginosa. Protein Cell. 6(1):26–41. eng. doi:10.1007/s13238-014-0100-x.

Lee YH, Kim BH, Kim JH, Yoon WS, Bang SH, Park YK. 2007. CadC has a global translational effect during acid adaptation in Salmonella enterica serovar Typhimurium. J Bacteriol. 189(6):2417–2425. eng. doi:10.1128/JB.01277-06.

Lewis K. 2010. Persister cells. Annu Rev Microbiol. 64:357–372. eng. doi:10.1146/annurev.micro.112408.134306.

Linderoth N, Morris DR. 1983. Structural specificity of the triamines sym-homospermidine and aminopropylcadaverine in stimulating growth of spermidine auxotrophs of Escherichia coli. Biochem Biophys Res Commun. 117(2):616–622. eng. doi:10.1016/0006-291x(83)91245-7.

Lindgren V, Wretlind B. 1987. Characterization of a Pseudomonas aeruginosa transposon insertion mutant with defective release of exoenzymes. J Gen Microbiol. 133(3):675–681. eng. doi:10.1099/00221287-133-3-675.

Lo Sciuto A, Imperi F. 2018. Aminoarabinosylation of Lipid A Is Critical for the Development of Colistin Resistance in Pseudomonas aeruginosa. Antimicrob Agents Chemother. 62(3). eng. doi:10.1128/AAC.01820-17.

Lonsdale R, Ward RA. 2018. Structure-based design of targeted covalent inhibitors. Chem Soc Rev. 47(11):3816–3830. eng. doi:10.1039/c7cs00220c.

Lowe-Power TM, Hendrich CG, Roepenack-Lahaye E von, Li B, Wu D, Mitra R, Dalsing BL, Ricca P, Naidoo J, Cook D, et al. 2018. Metabolomics of tomato xylem sap during bacterial wilt reveals Ralstonia solanacearum produces abundant putrescine, a metabolite that accelerates wilt disease. Environ Microbiol. 20(4):1330–1349. eng. doi:10.1111/1462-2920.14020.

Lu C-D. 2006. Pathways and regulation of bacterial arginine metabolism and perspectives for obtaining arginine overproducing strains. Appl Microbiol Biotechnol. 70(3):261–272. eng. doi:10.1007/s00253-005-0308-z.

Lu C-D, Itoh Y, Nakada Y, Jiang Y. 2002. Functional analysis and regulation of the divergent spuABCDEFGH-spuI operons for polyamine uptake and utilization in Pseudomonas aeruginosa PAO1. J Bacteriol. 184(14):3765–3773. eng. doi:10.1128/jb.184.14.3765-3773.2002.

Lynch JP, Zhanel GG, Clark NM. 2017. Emergence of Antimicrobial Resistance among Pseudomonas aeruginosa: Implications for Therapy. Semin Respir Crit Care Med. 38(3):326–345. eng. doi:10.1055/s-0037-1602583.

Maccarrone M, Bari M, Battista N, Di Rienzo M, Falciglia K, Finazzi Agrò A. 2001. Oxidation products of polyamines induce mitochondrial uncoupling and cytochrome c release. FEBS Lett. 507(1):30–34. doi:10.1016/S0014-5793(01)02949-0.

Mackintosh CA, Pegg AE. 2000. Effect of spermine synthase deficiency on polyamine biosynthesis

and content in mice and embryonic fibroblasts, and the sensitivity of fibroblasts to 1,3-bis-(2-chloroethyl)-N-nitrosourea. Biochem J. 351 Pt 2:439–447. eng.

Madeo F, Eisenberg T, Pietrocola F, Kroemer G. 2018. Spermidine in health and disease. Science. 359(6374). eng. doi:10.1126/science.aan2788.

Magill SS, Edwards JR, Bamberg W, Beldavs ZG, Dumyati G, Kainer MA, Lynfield R, Maloney M, McAllister-Hollod L, Nadle J, et al. 2014. Multistate point-prevalence survey of health care-associated infections. N Engl J Med. 370(13):1198–1208. eng. doi:10.1056/NEJMoa1306801.

Mahadevi AS, Sastry GN. 2013. Cation-π interaction: Its role and relevance in chemistry, biology, and material science. Chem Rev. 113(3):2100–2138. eng. doi:10.1021/cr300222d.

Malhotra S, Hayes D, Wozniak DJ. 2019. Cystic Fibrosis and Pseudomonas aeruginosa: The Host-Microbe Interface. Clin Microbiol Rev. 32(3). eng. doi:10.1128/CMR.00138-18.

Marshall MS, Steele RP, Thanthiriwatte KS, Sherrill CD. 2009. Potential energy curves for cation-pi interactions: Off-axis configurations are also attractive. J Phys Chem A. 113(48):13628–13632. eng. doi:10.1021/jp906086x.

Martínez A, Ostrovsky P, Nunn DN. 1999. LipC, a second lipase of Pseudomonas aeruginosa, is LipB and Xcp dependent and is transcriptionally regulated by pilus biogenesis components. Mol Microbiol. 34(2):317–326. eng. doi:10.1046/j.1365-2958.1999.01601.x.

Martz E. 2002. Protein Explorer: Easy yet powerful macromolecular visualization. Trends Biochem Sci. 27(2):107–109. doi:10.1016/S0968-0004(01)02008-4.

Masuda N, Sakagawa E, Ohya S, Gotoh N, Tsujimoto H, Nishino T. 2000. Substrate specificities of MexAB-OprM, MexCD-OprJ, and MexXY-oprM efflux pumps in Pseudomonas aeruginosa. Antimicrob Agents Chemother. 44(12):3322–3327. eng. doi:10.1128/aac.44.12.3322-3327.2000.

Matthews BW. 1968. Solvent content of protein crystals. J Mol Biol. 33(2):491–497. doi:10.1016/0022-2836(68)90205-2.

Maurice NM, Bedi B, Sadikot RT. 2018. Pseudomonas aeruginosa Biofilms: Host Response and Clinical Implications in Lung Infections. Am J Respir Cell Mol Biol. 58(4):428–439. eng. doi:10.1165/rcmb.2017-0321TR.

McGinnis MW, Parker ZM, Walter NE, Rutkovsky AC, Cartaya-Marin C, Karatan E. 2009. Spermidine regulates Vibrio cholerae biofilm formation via transport and signaling pathways. FEMS Microbiol Lett. 299(2):166–174. eng. doi:10.1111/j.1574-6968.2009.01744.x.

McPhee JB, Bains M, Winsor G, Lewenza S, Kwasnicka A, Brazas MD, Brinkman FSL, Hancock REW. 2006. Contribution of the PhoP-PhoQ and PmrA-PmrB two-component regulatory systems to Mg2+-induced gene regulation in Pseudomonas aeruginosa. J Bacteriol. 188(11):3995–4006. eng. doi:10.1128/JB.00053-06.

Mecozzi S, West AP, Dougherty DA. 1996a. Cation-pi interactions in aromatics of biological and medicinal interest: Electrostatic potential surfaces as a useful qualitative guide. Proc Natl Acad Sci USA. 93(20):10566–10571. eng. doi:10.1073/pnas.93.20.10566.

Mecozzi S, West AP, Dougherty DA. 1996b. Cation−π Interactions in Simple Aromatics: Electrostatics Provide a Predictive Tool. J Am Chem Soc. 118(9):2307–2308. doi:10.1021/ja9539608.

Meyer RA, Henley CM, Meyer MH, Morgan PL, McDonald AG, Mills C, Price DK. 1998. Partial Deletion of both the Spermine Synthase Gene and the Pex Gene in the X-linked Hypophosphatemic, Gyro (Gy) Mouse. Genomics. 48(3):289–295. doi:10.1006/geno.1997.5169.

Michael AJ. 2016. Polyamines in Eukaryotes, Bacteria, and Archaea. J Biol Chem. 291(29):14896–14903. eng. doi:10.1074/jbc.R116.734780.

Michael AJ. 2018. Polyamine function in archaea and bacteria. J Biol Chem. 293(48):18693–18701. eng. doi:10.1074/jbc.TM118.005670.

Michaelis L, Menten ML, Johnson KA, Goody RS. 2011. The original Michaelis constant: Translation of the 1913 Michaelis-Menten paper. Biochemistry. 50(39):8264–8269. eng. doi:10.1021/bi201284u.

Minois N. 2014. Molecular basis of the 'anti-aging' effect of spermidine and other natural polyamines - a mini-review. Gerontology. 60(4):319–326. eng. doi:10.1159/000356748.

Minoux H, Chipot C. 1999. Cation−π Interactions in Proteins: Can Simple Models Provide an Accurate Description? J Am Chem Soc. 121(44):10366–10372. doi:10.1021/ja990914p.

Miyamoto S, Kashiwagi K, Ito K, Watanabe S, Igarashi K. 1993. Estimation of polyamine distribution and polyamine stimulation of protein synthesis in Escherichia coli. Arch Biochem Biophys. 300(1):63–68. eng. doi:10.1006/abbi.1993.1009.

Morata L, Cobos-Trigueros N, Martínez JA, Soriano A, Almela M, Marco F, Sterzik H, Núñez R, Hernández C, Mensa J. 2012. Influence of multidrug resistance and appropriate empirical therapy on the 30-day mortality rate of Pseudomonas aeruginosa bacteremia. Antimicrob Agents Chemother. 56(9):4833–4837. eng. doi:10.1128/AAC.00750-12.

Moreau PL. 2007. The lysine decarboxylase CadA protects Escherichia coli starved of phosphate against fermentation acids. J Bacteriol. 189(6):2249–2261. eng. doi:10.1128/JB.01306-06.

Morikubo N, Fukuda Y, Ohtake K, Shinya N, Kiga D, Sakamoto K, Asanuma M, Hirota H, Yokoyama S, Hoshino T. 2006. Cation-pi interaction in the polyolefin cyclization cascade uncovered by incorporating unnatural amino acids into the catalytic sites of squalene cyclase. J Am Chem Soc. 128(40):13184–13194. eng. doi:10.1021/ja063358p.

Moskowitz SM, Ernst RK, Miller SI. 2004. PmrAB, a two-component regulatory system of Pseudomonas aeruginosa that modulates resistance to cationic antimicrobial peptides and addition of aminoarabinose to lipid A. J Bacteriol. 186(2):575–579. eng. doi:10.1128/jb.186.2.575-579.2004.

Mulcahy H, Charron-Mazenod L, Lewenza S. 2008. Extracellular DNA chelates cations and induces antibiotic resistance in Pseudomonas aeruginosa biofilms. PLoS Pathog. 4(11):e1000213. eng. doi:10.1371/journal.ppat.1000213.

Nakada Y, Itoh Y. 2003. Identification of the putrescine biosynthetic genes in Pseudomonas aeruginosa and characterization of agmatine deiminase and N-carbamoylputrescine

amidohydrolase of the arginine decarboxylase pathway. Microbiology (Reading, Engl). 149(Pt 3):707–714. eng. doi:10.1099/mic.0.26009-0.

Nakao H, Shinoda S, Yamamoto S. 1991. Purification and some properties of carboxynorspermidine synthase participating in a novel biosynthetic pathway for norspermidine in Vibrio alginolyticus. J Gen Microbiol. 137(7):1737–1742. eng. doi:10.1099/00221287-137-7-1737.

Nakashima M, Yamagami R, Tomikawa C, Ochi Y, Moriya T, Asahara H, Fourmy D, Yoshizawa S, Oshima T, Hori H. 2017. Long and branched polyamines are required for maintenance of the ribosome, tRNAHis and tRNATyr in Thermus thermophilus cells at high temperatures. Genes Cells. 22(7):628–645. eng. doi:10.1111/gtc.12502.

Nicas TI, Hancock RE. 1983. Pseudomonas aeruginosa outer membrane permeability: Isolation of a porin protein F-deficient mutant. J Bacteriol. 153(1):281–285. eng.

Nichols CG, Lee S-J. 2018. Polyamines and potassium channels: A 25-year romance. J Biol Chem. 293(48):18779–18788. eng. doi:10.1074/jbc.TM118.003344.

Nishimura K, Lee SB, Park JH, Park MH. 2012. Essential role of eIF5A-1 and deoxyhypusine synthase in mouse embryonic development. Amino Acids. 42(2-3):703–710. eng. doi:10.1007/s00726-011-0986-z.

Normark S. 1995. beta-Lactamase induction in gram-negative bacteria is intimately linked to peptidoglycan recycling. Microb Drug Resist. 1(2):111–114. eng. doi:10.1089/mdr.1995.1.111.

Ober D, Harms R, Witte L, Hartmann T. 2003. Molecular evolution by change of function. Alkaloid-specific homospermidine synthase retained all properties of deoxyhypusine synthase except binding the eIF5A precursor protein. J Biol Chem. 278(15):12805–12812. eng. doi:10.1074/jbc.M207112200.

Ober D, Hartmann T. 1999a. Deoxyhypusine synthase from tobacco. cDNA isolation, characterization, and bacterial expression of an enzyme with extended substrate specificity. J Biol Chem. 274(45):32040–32047. eng. doi:10.1074/jbc.274.45.32040.

Ober D, Hartmann T. 1999b. Homospermidine synthase, the first pathway-specific enzyme of pyrrolizidine alkaloid biosynthesis, evolved from deoxyhypusine synthase. Proc Natl Acad Sci USA. 96(26):14777–14782. eng. doi:10.1073/pnas.96.26.14777.

Ober D, Tholl D, Martin W, Hartmann T. 1996. Homospermidine synthase of Rhodopseudomonas viridis: Substrate specificity and effects of the heterologously expressed enzyme on polyamine metabolism of Escherichia coli. J Gen Appl Microbiol. 42(5):411–419. doi:10.2323/jgam.42.411.

Ohnuma M, Terui Y, Tamakoshi M, Mitome H, Niitsu M, Samejima K, Kawashima E, Oshima T. 2005. N1-aminopropylagmatine, a new polyamine produced as a key intermediate in polyamine biosynthesis of an extreme thermophile, Thermus thermophilus. J Biol Chem. 280(34):30073–30082. eng. doi:10.1074/jbc.M413332200.

Ong SA, Peterson T, Neilands JB. 1979. Agrobactin, a siderophore from Agrobacterium tumefaciens. J Biol Chem. 254(6):1860–1865. eng.

Oves-Costales D, Kadi N, Fogg MJ, Song L, Wilson KS, Challis GL. 2007. Enzymatic logic of anthrax stealth siderophore biosynthesis: AsbA catalyzes ATP-dependent condensation of citric acid and spermidine. J Am Chem Soc. 129(27):8416–8417. eng. doi:10.1021/ja072391o.

Pan Y, Zhang K, Qi J, Yue J, Springer TA, Chen J. 2010. Cation-pi interaction regulates ligand-binding affinity and signaling of integrin alpha4beta7. Proc Natl Acad Sci USA. 107(50):21388–21393. eng. doi:10.1073/pnas.1015487107.

Park MH, Cooper HL, Folk JE. 1981. Identification of hypusine, an unusual amino acid, in a protein from human lymphocytes and of spermidine as its biosynthetic precursor. Proc Natl Acad Sci USA. 78(5):2869–2873. eng. doi:10.1073/pnas.78.5.2869.

Park MH, Joe YA, Kang KR. 1998. Deoxyhypusine synthase activity is essential for cell viability in the yeast Saccharomyces cerevisiae. J Biol Chem. 273(3):1677–1683. eng. doi:10.1074/jbc.273.3.1677.

Park MH, Wolff EC. 2018. Hypusine, a polyamine-derived amino acid critical for eukaryotic translation. J Biol Chem. 293(48):18710–18718. eng. doi:10.1074/jbc.TM118.003341.

Park YK, Bearson B, Bang SH, Bang IS, Foster JW. 1996. Internal pH crisis, lysine decarboxylase and the acid tolerance response of Salmonella typhimurium. Mol Microbiol. 20(3):605–611. eng. doi:10.1046/j.1365-2958.1996.5441070.x.

Pasini A, Caldarera CM, Giordano E. 2014. Chromatin remodeling by polyamines and polyamine analogs. Amino Acids. 46(3):595–603. eng. doi:10.1007/s00726-013-1550-9.

Patankar YR, Lovewell RR, Poynter ME, Jyot J, Kazmierczak BI, Berwin B. 2013. Flagellar motility is a key determinant of the magnitude of the inflammasome response to Pseudomonas aeruginosa. Infect Immun. 81(6):2043–2052. eng. doi:10.1128/IAI.00054-13.

Patel CN, Wortham BW, Lines JL, Fetherston JD, Perry RD, Oliveira MA. 2006. Polyamines are essential for the formation of plague biofilm. J Bacteriol. 188(7):2355–2363. eng. doi:10.1128/JB.188.7.2355-2363.2006.

Patterson AL. 1934. A Fourier Series Method for the Determination of the Components of Interatomic Distances in Crystals. Phys Rev. 46(5):372–376. doi:10.1103/PhysRev.46.372.

Pegg AE. 2009. Mammalian polyamine metabolism and function. IUBMB Life. 61(9):880–894. eng. doi:10.1002/iub.230.

Peters G, Locci R, Pulverer G. 1981. Microbial colonization of prosthetic devices. II. Scanning electron microscopy of naturally infected intravenous catheters. Zentralbl Bakteriol Mikrobiol Hyg B. 173(5):293–299. eng.

Pettersen EF, Goddard TD, Huang CC, Couch GS, Greenblatt DM, Meng EC, Ferrin TE. 2004. UCSF Chimera-A visualization system for exploratory research and analysis. J Comput Chem. 25(13):1605–1612. doi:10.1002/jcc.20084.

Pier GB, Coleman F, Grout M, Franklin M, Ohman DE. 2001. Role of alginate O acetylation in resistance of mucoid Pseudomonas aeruginosa to opsonic phagocytosis. Infect Immun.

69(3):1895–1901. eng. doi:10.1128/IAI.69.3.1895-1901.2001.

Piotrowski M, Janowitz T, Kneifel H. 2003. Plant C-N hydrolases and the identification of a plant N-carbamoylputrescine amidohydrolase involved in polyamine biosynthesis. J Biol Chem. 278(3):1708–1712. eng. doi:10.1074/jbc.M205699200.

Pless SA, Hanek AP, Price KL, Lynch JW, Lester HA, Dougherty DA, Lummis SCR. 2011. A Cation-π Interaction at a Phenylalanine Residue in the Glycine Receptor Binding Site Is Conserved for Different Agonists. Mol Pharmacol. 79(4):742–748. doi:10.1124/mol.110.069583.

Pletneva EV, Laederach AT, Fulton DB, Kostic NM. 2001. The role of cation-pi interactions in biomolecular association. Design of peptides favoring interactions between cationic and aromatic amino acid side chains. J Am Chem Soc. 123(26):6232–6245. eng. doi:10.1021/ja010401u.

Pohl E, Brunner N, Wilmanns M, Hensel R. 2002. The crystal structure of the allosteric non-phosphorylating glyceraldehyde-3-phosphate dehydrogenase from the hyperthermophilic archaeum Thermoproteus tenax. J. Biol. Chem. 277(22):19938–19945. eng. doi:10.1074/jbc.M112244200.

Potterton E, Briggs P, Turkenburg M, Dodson E. 2003. A graphical user interface to the CCP4 program suite. Acta Crystallogr D Biol Crystallogr. 59(Pt 7):1131–1137. eng. doi:10.1107/s0907444903008126.

Qu L, She P, Wang Y, Liu F, Di Zhang, Chen L, Luo Z, Xu H, Qi Y, Wu Y. 2016. Effects of norspermidine on Pseudomonas aeruginosa biofilm formation and eradication. Microbiologyopen. 5(3):402–412. eng. doi:10.1002/mbo3.338.

Ramos J-L, editor. 2004. Pseudomonas: Volume 1 Genomics, Life Style and Molecular Architecture. Boston, MA: Springer US. 1 Online-Ressource (XVIII, 835. ISBN: 1441990860.

Reddy AS, Sastry GM, Sastry GN. 2007. Cation-aromatic database. Proteins. 67(4):1179–1184. eng. doi:10.1002/prot.21202.

Reddy AS, Sastry GN. 2005. Cation M = H+, Li+, Na+, K+, Ca2+, Mg2+, NH4+, and NMe4+ interactions with the aromatic motifs of naturally occurring amino acids: A theoretical study. J Phys Chem A. 109(39):8893–8903. eng. doi:10.1021/jp0525179.

Redmond TM, Poliakov E, Kuo S, Chander P, Gentleman S. 2010. RPE65, visual cycle retinol isomerase, is not inherently 11-cis-specific: Support for a carbocation mechanism of retinol isomerization. J Biol Chem. 285(3):1919–1927. eng. doi:10.1074/jbc.M109.027458.

Reimann A, Nurhayati N, Backenköhler A, Ober D. 2004. Repeated evolution of the pyrrolizidine alkaloid-mediated defense system in separate angiosperm lineages. Plant Cell. 16(10):2772–2784. eng. doi:10.1105/tpc.104.023176.

Rhodes G. 2009. Crystallography made crystal clear: A guide for users of macromolecular models. 3. ed., [Nachdr.]. Amsterdam: Elsevier. 306 p. (Complementary science series). ISBN: 9780125870733. eng.

Rider JE, Hacker A, Mackintosh CA, Pegg AE, Woster PM, Casero RA. 2007. Spermine and

spermidine mediate protection against oxidative damage caused by hydrogen peroxide. Amino Acids. 33(2):231–240. eng. doi:10.1007/s00726-007-0513-4.

Rosenthal RG, Ebert M-O, Kiefer P, Peter DM, Vorholt JA, Erb TJ. 2014. Direct evidence for a covalent ene adduct intermediate in NAD(P)H-dependent enzymes. Nat Chem Biol. 10(1):50–55. eng. doi:10.1038/nchembio.1385.

Rosenthal RG, Vögeli B, Quade N, Capitani G, Kiefer P, Vorholt JA, Ebert M-O, Erb TJ. 2015. The use of ene adducts to study and engineer enoyl-thioester reductases. Nat Chem Biol. 11(6):398–400. doi:10.1038/nchembio.1794.

Roveri OA, Bilmes GM, Heihoff K, Braslavsky SE. 1990. Laser-Induced Optoacoustic Spectroscopy (LIOAS) of Proteins: Spectrum of Bovine Serum Albumin in the 532–670 nm Region. Appl Spectrosc. 44(10):1706–1710. doi:10.1366/0003702904417616.

Roveri OA, Braslavsky SE. 2012. π-Cation interactions as the origin of the weak absorption at 532 nm observed in tryptophan-containing polypeptides. Photochem Photobiol Sci. 11(6):962–966. eng. doi:10.1039/c2pp05341a.

Rubach JK, Plapp BV. 2003. Amino Acid Residues in the Nicotinamide Binding Site Contribute to Catalysis by Horse Liver Alcohol Dehydrogenase. Biochemistry. 42(10):2907–2915. doi:10.1021/bi0272656.

Rupp B. 2010. Biomolecular crystallography: Principles, practice, and application to structural biology. New York, NY: Garland Science. 809 p. ISBN: 9780815340812. eng.

Sakanaka M, Sugiyama Y, Kitakata A, Katayama T, Kurihara S. 2016. Carboxyspermidine decarboxylase of the prominent intestinal microbiota species Bacteroides thetaiotaomicron is required for spermidine biosynthesis and contributes to normal growth. Amino Acids. 48(10):2443–2451. eng. doi:10.1007/s00726-016-2233-0.

Sakanaka M, Sugiyama Y, Nara M, Kitakata A, Kurihara S. 2018. Functional analysis of arginine decarboxylase gene speA of Bacteroides dorei by markerless gene deletion. FEMS Microbiol Lett. 365(4). eng. doi:10.1093/femsle/fny003.

Salvi M, Toninello A. 2004. Effects of polyamines on mitochondrial Ca(2+) transport. Biochim Biophys Acta. 1661(2):113–124. eng. doi:10.1016/j.bbamem.2003.12.005.

Sánchez-Jiménez F, Medina MÁ, Villalobos-Rueda L, Urdiales JL. 2019. Polyamines in mammalian pathophysiology. Cell Mol Life Sci. eng. doi:10.1007/s00018-019-03196-0.

Sandkvist M. 2001. Type II secretion and pathogenesis. Infect Immun. 69(6):3523–3535. eng. doi:10.1128/IAI.69.6.3523-3535.2001.

Sandor R, Slanina J, Midlik A, Sebrlova K, Novotna L, Carnecka M, Slaninova I, Taborsky P, Taborska E, Pes O. 2018. Sanguinarine is reduced by NADH through a covalent adduct. Phytochemistry. 145:77–84. eng. doi:10.1016/j.phytochem.2017.10.010.

Scheetz MH, Hoffman M, Bolon MK, Schulert G, Estrellado W, Baraboutis IG, Sriram P, Dinh M, Owens LK, Hauser AR. 2009. Morbidity associated with Pseudomonas aeruginosa bloodstream

infections. Diagn Microbiol Infect Dis. 64(3):311–319. eng. doi:10.1016/j.diagmicrobio.2009.02.006.

Schrödinger LLC. 2015. The PyMOL Molecular Graphics System, Version 2.4.0.

Seifi HS, Shelp BJ. 2019. Spermine Differentially Refines Plant Defense Responses Against Biotic and Abiotic Stresses. Front Plant Sci. 10:117. eng. doi:10.3389/fpls.2019.00117.

Shao L, Majumdar R, Minocha SC. 2012. Profiling the aminopropyltransferases in plants: Their structure, expression and manipulation. Amino Acids. 42(2-3):813–830. eng. doi:10.1007/s00726-011-0998-8.

Shaw FL, Elliott KA, Kinch LN, Fuell C, Phillips MA, Michael AJ. 2010. Evolution and multifarious horizontal transfer of an alternative biosynthetic pathway for the alternative polyamine sym-homospermidine. J Biol Chem. 285(19):14711–14723. eng. doi:10.1074/jbc.M110.107219.

Sobe RC, Bond WG, Wotanis CK, Zayner JP, Burriss MA, Fernandez N, Bruger EL, Waters CM, Neufeld HS, Karatan E. 2017. Spermine inhibits Vibrio cholerae biofilm formation through the NspS-MbaA polyamine signaling system. J Biol Chem. 292(41):17025–17036. eng. doi:10.1074/jbc.M117.801068.

Spradling AC, Stern D, Beaton A, Rhem EJ, Laverty T, Mozden N, Misra S, Rubin GM. 1999. The Berkeley Drosophila Genome Project gene disruption project: Single P-element insertions mutating 25% of vital Drosophila genes. Genetics. 153(1):135–177. eng.

Srivenugopal KS, Adiga PR. 1980. Partial purification and properties of a transamidinase from Lathyrus sativus seedlings. Involvement in homoarginine metabolism and amine interconversions. Biochem J. 189(3):553–560. eng. doi:10.1042/bj1890553.

Stefanelli C, Stanic' I, Zini M, Bonavita F, Flamigni F, Zambonin L, Landi L, Pignatti C, Guarnieri C, Caldarera CM. 2000. Polyamines directly induce release of cytochrome c from heart mitochondria. Biochem J. 347 Pt 3:875–880. eng.

Sugimoto A. 2004. High-throughput RNAi in Caenorhabditis elegans: Genome-wide screens and functional genomics. Differentiation. 72(2-3):81–91. eng. doi:10.1111/j.1432-0436.2004.07202004.x.

Sunner J, Nishizawa K, Kebarle P. 1981. Ion-solvent molecule interactions in the gas phase. The potassium ion and benzene. J Phys Chem. 85(13):1814–1820. doi:10.1021/j150613a011.

Tait GH. 1976. A new pathway for the biosynthesis of spermidine. Biochem Soc Trans. 4(4):610–612. eng. doi:10.1042/bst0040610.

Tait GH. 1979. The formation of homospermidine by an enzyme from Rhodopseudomonas viridis (proceedings). Biochem Soc Trans. 7(1):199–201. eng. doi:10.1042/bst0070199.

Tholl D, Ober D, Martin W, Kellermann J, Hartmann T. 1996. Purification, molecular cloning and expression in Escherichia coli of homospermidine synthase from Rhodopseudomonas viridis. Eur J Biochem. 240(2):373–379. eng. doi:10.1111/j.1432-1033.1996.0373h.x.

Tierney AR, Rather PN. 2019. Roles of two-component regulatory systems in antibiotic resistance. Future Microbiol. 14:533–552. eng. doi:10.2217/fmb-2019-0002.

Torrice MM, Bower KS, Lester HA, Dougherty DA. 2009. Probing the role of the cation-π interaction in the binding sites of GPCRs using unnatural amino acids. Proc Natl Acad Sci USA. 106(29):11919–11924. doi:10.1073/pnas.0903260106.

Tseng BS, Zhang W, Harrison JJ, Quach TP, Song JL, Penterman J, Singh PK, Chopp DL, Packman AI, Parsek MR. 2013. The extracellular matrix protects Pseudomonas aeruginosa biofilms by limiting the penetration of tobramycin. Environ Microbiol. 15(10):2865–2878. eng. doi:10.1111/1462-2920.12155.

Tsybovsky Y, Donato H, Krupenko NI, Davies C, Krupenko SA. 2007. Crystal Structures of the Carboxyl Terminal Domain of Rat 10-Formyltetrahydrofolate Dehydrogenase: Implications for the Catalytic Mechanism of Aldehyde Dehydrogenases. Biochemistry. 46(11):2917–2929. doi:10.1021/bi0619573.

Umland TC, Wolff EC, Park MH, Davies DR. 2004. A new crystal structure of deoxyhypusine synthase reveals the configuration of the active enzyme and of an enzyme.NAD.inhibitor ternary complex. J Biol Chem. 279(27):28697–28705. eng. doi:10.1074/jbc.M404095200.

Vaara M. 1992. Agents that increase the permeability of the outer membrane. Microbiol Rev. 56(3):395–411. eng.

Vijay D, Sastry GN. 2008. Exploring the size dependence of cyclic and acyclic pi-systems on cation-pi binding. Phys Chem Chem Phys. 10(4):582–590. eng. doi:10.1039/b713703f.

Vögeli B, Rosenthal RG, Stoffel GMM, Wagner T, Kiefer P, Cortina NS, Shima S, Erb TJ. 2018. InhA, the enoyl-thioester reductase from Mycobacterium tuberculosis forms a covalent adduct during catalysis. J. Biol. Chem. 293(44):17200–17207. doi:10.1074/jbc.RA118.005405.

Vrbancich J, Ritchie GLD. 1980. Quadrupole moments of benzene, hexafluorobenzene and other non-dipolar aromatic molecules. J. Chem. Soc., Faraday Trans. 2. 76:648. doi:10.1039/f29807600648.

Walters MC, Roe F, Bugnicourt A, Franklin MJ, Stewart PS. 2003. Contributions of antibiotic penetration, oxygen limitation, and low metabolic activity to tolerance of Pseudomonas aeruginosa biofilms to ciprofloxacin and tobramycin. Antimicrob Agents Chemother. 47(1):317–323. eng. doi:10.1128/aac.47.1.317-323.2003.

Wang B-C. 1985. Resolution of phase ambiguity in macromolecular crystallography. In: Wyckoff HW, editor. Diffraction methods for biological macromolecules. Vol. 115. New York, NY: Acad. Press. p. 90–112 (Methods in Enzymology; vol. 115).

Wang J, Wang J, Zhang L-H. 2018. Immunological blocking of spermidine-mediated host-pathogen communication provides effective control against Pseudomonas aeruginosa infection. Microb Biotechnol. eng. doi:10.1111/1751-7915.13279.

Wang W, Paschalidis K, Feng J-C, Song J, Liu J-H. 2019. Polyamine Catabolism in Plants: A Universal Process With Diverse Functions. Front Plant Sci. 10:561. eng. doi:10.3389/fpls.2019.00561.

Wang Y, Kim SH, Natarajan R, Heindl JE, Bruger EL, Waters CM, Michael AJ, Fuqua C. 2016. Spermidine Inversely Influences Surface Interactions and Planktonic Growth in Agrobacterium tumefaciens. J Bacteriol. 198(19):2682–2691. eng. doi:10.1128/JB.00265-16.

Wargnies B, Lauwers N, Stalon V. 1979. Structure and properties of the putrescine carbamoyltransferase of Streptococcus faecalis. Eur J Biochem. 101(1):143–152. eng. doi:10.1111/j.1432-1033.1979.tb04226.x.

Watanabe S, Kusama-Eguchi K, Kobayashi H, Igarashi K. 1991. Estimation of polyamine binding to macromolecules and ATP in bovine lymphocytes and rat liver. J Biol Chem. 266(31):20803–20809. eng.

Wątor E, Wilk P, Grudnik P. 2020. Half Way to Hypusine—Structural Basis for Substrate Recognition by Human Deoxyhypusine Synthase. Biomolecules. 10(4):522. doi:10.3390/biom10040522.

Weiss T, Bernhardt G, Buschauer A, Jauch KW, Zirngibl H. 1997. High-resolution reversed-phase high-performance liquid chromatography analysis of polyamines and their monoacetyl conjugates by fluorescence detection after derivatization with N-hydroxysuccinimidyl 6-quinolinyl carbamate. Anal Biochem. 247(2):294–304. eng. doi:10.1006/abio.1997.2091.

Williams BJ, Du R-H, Calcutt MW, Abdolrasulnia R, Christman BW, Blackwell TS. 2010. Discovery of an operon that participates in agmatine metabolism and regulates biofilm formation in Pseudomonas aeruginosa. Mol Microbiol. 76(1):104–119. eng. doi:10.1111/j.1365-2958.2010.07083.x.

Wolff EC, Folk JE, Park MH. 1997. Enzyme-substrate intermediate formation at lysine 329 of human deoxyhypusine synthase. J Biol Chem. 272(25):15865–15871. eng. doi:10.1074/jbc.272.25.15865.

Wortham BW, Oliveira MA, Fetherston JD, Perry RD. 2010. Polyamines are required for the expression of key Hms proteins important for Yersinia pestis biofilm formation. Environ Microbiol. 12(7):2034–2047. eng. doi:10.1111/j.1462-2920.2010.02219.x.

Wu H, Min J, Ikeguchi Y, Zeng H, Dong A, Loppnau P, Pegg AE, Plotnikov AN. 2007. Structure and Mechanism of Spermidine Synthases. Biochemistry. 46(28):8331–8339. doi:10.1021/bi602498k.

Xiu X, Puskar NL, Shanata JAP, Lester HA, Dougherty DA. 2009. Nicotine binding to brain receptors requires a strong cation–π interaction. Nature. 458(7237):534–537. doi:10.1038/nature07768.

Xu Y, Labedan B, Glansdorff N. 2007. Surprising arginine biosynthesis: A reappraisal of the enzymology and evolution of the pathway in microorganisms. Microbiol Mol Biol Rev. 71(1):36–47. eng. doi:10.1128/MMBR.00032-06.

Xue Y, Davis AV, Balakrishnan G, Stasser JP, Staehlin BM, Focia P, Spiro TG, Penner-Hahn JE, O'Halloran TV. 2008. Cu(I) recognition via cation-pi and methionine interactions in CusF. Nat Chem Biol. 4(2):107–109. eng. doi:10.1038/nchembio.2007.57.

Yamamoto S, Nagata S, Kusaba K. 1993. Purification and characterization of homospermidine synthase in Acinetobacter tartarogenes ATCC 31105. J Biochem. 114(1):45–49. eng. doi:10.1093/oxfordjournals.jbchem.a124137.

Yamamoto S, Sugahara T, Tougou K, Shinoda S. 1994. Cloning and nucleotide sequence of the carboxynorspermidine decarboxylase gene from Vibrio alginolyticus. Microbiology (Reading, Engl). 140 (Pt 11):3117–3124. eng. doi:10.1099/13500872-140-11-3117.

Yamashita T, Nishimura K, Saiki R, Okudaira H, Tome M, Higashi K, Nakamura M, Terui Y, Fujiwara K, Kashiwagi K, et al. 2013. Role of polyamines at the G1/S boundary and G2/M phase of the cell cycle. Int J Biochem Cell Biol. 45(6):1042–1050. eng. doi:10.1016/j.biocel.2013.02.021.

Yao X, He W, Lu C-D. 2011. Functional characterization of seven γ-Glutamylpolyamine synthetase genes and the bauRABCD locus for polyamine and β-Alanine utilization in Pseudomonas aeruginosa PAO1. J Bacteriol. 193(15):3923–3930. eng. doi:10.1128/JB.05105-11.

Yao X, Li C, Zhang J, Lu C-D. 2012. γ-glutamyl Spermine Synthetase PauA2 as a potential target of antibiotic development against Pseudomonas aeruginosa. Antimicrob Agents Chemother. 56(10):5309–5314. eng. doi:10.1128/AAC.01158-12.

Zacharias N. 2002. Cation–π interactions in ligand recognition and catalysis. Trends Pharmacol Sci. 23(6):281–287. doi:10.1016/S0165-6147(02)02027-8.

Zarb P, Coignard B, Griskeviciene J, Muller A, Vankerckhoven V, Weist K, Goossens M, Vaerenberg S, Hopkins S, Catry B, et al. 2012. The European Centre for Disease Prevention and Control (ECDC) pilot point prevalence survey of healthcare-associated infections and antimicrobial use. Euro Surveill. 17(46). eng. doi:10.2807/ese.17.46.20316-en.

Zhang H-T, Liu H. 2015. Laboratory-based evaluation of MDR strains of Pseudomonas in patients with acute burn injuries. Int J Clin Exp Med. 8(9):16512–16519. eng.

Zhang KYJ, Main P. 1990. Histogram matching as a new density modification technique for phase refinement and extension of protein molecules. Acta Crystallogr A. 46(1):41–46. doi:10.1107/S0108767389009311.

Zhong W, Gallivan JP, Zhang Y, Li L, Lester HA, Dougherty DA. 1998. From ab initio quantum mechanics to molecular neurobiology: A cation-π binding site in the nicotinic receptor. Proc Natl Acad Sci USA. 95(21):12088–12093. doi:10.1073/pnas.95.21.12088.

Zhou L, Wang J, Zhang L-H. 2007. Modulation of bacterial Type III secretion system by a spermidine transporter dependent signaling pathway. PLoS ONE. 2(12):e1291. eng. doi:10.1371/journal.pone.0001291.